Applications of quasiparticle forces in quantum technologies

Dissertation

zur Erlangung des Grades

des Doktors der Naturwissenschaften

der Naturwissenschaftlich - Technischen Fakultät

der Universität des Saarlandes

von

Raphael Pascal Schmit

Saarbrücken

2020

Tag des Kolloquiums:	10. Juni 2021
Dekan:	Prof. Dr. Jörn Eric Walter
Berichterstatter:	Prof. Dr. Frank Wilhelm-Mauch
	Prof. Dr. Alexander Brinkmann
Vorsitz:	Prof. Dr. Jürgen Eschner
Akad. Mitarbeiter:	Dr. Adam Wysocki

"*In science one tries to tell people, in such a way as to be understood by everyone, something that no one ever knew before. But in poetry, it's the exact opposite.*"

Paul Dirac

Abstract

The performance of many superconducting devices is diminished by long-lived Bogoliubov quasiparticle excitations present in the superconducting part. In normal-metal–insulator–superconductor structured micro-refrigerators, for example, the tunneling of quasiparticles into the normal metal and the accompanying backflow of heat just extracted from it, reduces the cooling efficiency. In superconducting qubits incoherent quasiparticle tunneling through Josephson junctions leads to qubit decoherence and relaxation. While the associated rates are small compared to those of currently more serious noise sources, quasiparticle tunneling is expected to be relevant for fulfilling the high requirements given by current quantum computation tasks based on fault tolerant quantum computing. Normal-metal quasiparticle traps among other established techniques are commonly used in order to redistribute the quasiparticles inside the superconducting part and reduce their density in regions which are more important for the device performance. In this thesis we quantitatively investigate on the trapping performance of such normal-metal quasiparticle traps and particularly the role taken by the superconducting proximity effect therein. The quasiclassical Green's function approach based on the non-equilibrium Keldysh technique serves as theoretical tool. As central physical quantities in the stationary non-equilibrium state the superconducting order parameter, local density of quasiparticle states and the quasiparticle density are put into context with the proximity effect. Two competing characteristics opposingly affecting the trapping performance are revealed, which points out the existence of an ideal trap position with optimal trapping performance. Furthermore, the conversion between dissipative normal current and supercurrent mediated by Andreev reflection and the resulting reduction of the quasiparticle density is studied.

A further part of this thesis is about the emulation of quantum field theory in curved spacetime involving spontaneous particle creation due to the conversion of virtual particles into real, detectable ones. We propose an experimental setup, where the dynamics of surface acoustic waves and phonons, respectively, on a piezoelectric semiconductor mimics the propagation of a massless scalar quantum field on a curved spacetime with an effective metric resembling that of a black hole and an expanding universe to some extent, including an acoustic event horizon for surface acoustic waves. An appropriate detection scheme indicating particle creation in form of phonons employs electron loaded dynamic quantum dots and a Stern-Gerlach gate for their readout. A non-thermal steady state for the electrons is predicted, which is ascribed to particle creation.

Zusammenfassung

Die Performance vieler auf Supraleitung basierender Quantentechnologien wird durch die Präsenz von langlebigen Bogoliubov-Quasiteilchen im supraleitenden Bauteil beeinträchtigt. Die Kühlleistung von elektronischen Mikro-Kühlern beispielsweise, die aus normal- und supraleitenden Metallen bestehende Tunnelkontakte verwenden, wird durch in das Normalmetall tunnelnde Quasiteilchen und dem damit einhergehendem Wärmefluss, welche dem Normalmetall zuvor entzogen wurden, reduziert. In supraleitenden Qubits führt inkohärentes Tunneln von Quasiteilchen durch Josephson-Kontakte zu Dekohärenz und Relaxation des Qubits. Zwar sind die damit verbundenen Raten im Vergleich zu denen anderer Fehlerquellen laut aktuellem Stand kleiner, man geht jedoch davon aus, dass das Tunneln von Quasiteilchen relevant ist, um die hohen Anforderungen, die aktuelle Anwendungen von fehlertoleranten Quantencomputern erfordern, zu erfüllen. Der Einsatz von Normalmetall-Quasiteilchenfallen und anderer experimenteller Techniken hat sich etabliert, um Quasiteilchen im supraleitenden Bauteil umzuverteilen und deren Dichte in für die Performance ausschlaggebenden Regionen zu reduzieren. In dieser Dissertation untersuchen wir quantitativ die Einfangperformance solcher Normalmetall-Quasiteilchenfallen und speziell die Rolle, die der supraleitende Proximity-Effekt dabei spielt. Als theoretisches Werkzeug dienen dabei quasiklassische Greensfunktionen, die auf der Keldysh-Technik für Nichtgleichgewichtssituationen basieren. Als zentrale physikalische Größen des stationären Nichtgleichgewichtszustandes werden der supraleitende Ordnungsparameter, die lokale Zustandsdichte der Quasiteilchen und deren Dichte mit dem Proximity-Effekt in Verbindung gebracht. Dabei werden zwei sich auf die Fallenwirkung gegensätzlich auswirkende Eigenschaften deutlich, welche die Existenz einer idealen Fallenpositionierung mit optimaler Einfangperformance aufzeigen. Zusätzlich wird die durch Andreev-Reflektion veraursachte Umwandlung zwischen dissipativem Normalstrom und Suprastrom und die damit verbundene Reduktion der Quasiteilchendichte studiert.

Ein weiterer Teil dieser Dissertation behandelt die Emulation von Quantenfeldtheorie in gekrümmter Raumzeit mit spontaner Teilchenproduktion aufgrund der Umwandlung von virtuellen in reale, detektierbare Teilchen. Wir schlagen ein Experiment vor, in dem die Ausbreitung von akustischen Oberflächenwellen beziehungsweise Phononen auf einem piezoelektrischen Halbleiter die Propagation eines masselosen skalaren Quantenfeldes in einer gekrümmten Raumzeit mit einer effektiven Metrik imitiert. Die effektive Metrik weist dabei Ähnlichkeiten zu der eines Schwarzen Loches und eines sich ausdehnendem Universums auf, einschließlich eines akustischen Horizonts für akustische Oberflächenwellen. Ein geeignetes Detektionsverfahren, welches auf Teilchenproduktion in Form von Phononen hindeutet, verwendet in dynamischen Quantenpunkten gefangene Elektronen und ein Stern-Gerlach-Gatter für deren Messung. Wir sagen einen nicht-thermischen Gleichgewichtszustand der Elektronen vorher, der der Teilchenproduktion zugeschrieben wird.

Publication List

Published

- Raphael P. Schmit, Bruno G. Taketani, Frank K. Wilhelm
  Quantum simulation of particle creation in curved space-time
  PLoS ONE 15(3): e0229382
- R. P. Schmit and F. K. Wilhelm
  Role of the proximity effect for normal-metal quasiparticle traps
  arXiv:2005.06867 (submitted to PRApplied)

Acknowledgements

First, I would like to express my deepest thanks to Frank Wilhelm-Mauch for giving me this great opportunity to join his research group and learn from him in various aspects. His rich knowledge about diverse areas, which he often connects effortlessly, is very inspiring and helpful and I learned a lot through his support. This also includes countless conferences and summer schools we could attend which allowed us to participate in the scientific world, not only remotely from Saarbrücken. Besides that, he leading the group very considerately and with two open ears gave me the necessary freedom to organize my working hours, especially during tough times.

It was a pleasure for me to work with Bruno Taketani, who co-supervised me during my Master thesis and with whom we worked together on one of the projects.

My thanks also go to the entire group and especially to my office roommates Andrii Sokolov, Susanna Kirchhoff and Peter Schuhmacher for a very pleasant and cheerful atmosphere.

I would like to thank Gino Bishop and Andrii, who helped with proofreading and provided very helpful comments.

Last but not least, I would like to express my thanks to my family. I am grateful to Angeline, who is at my side for over a decade with permanent reliability and support in all areas of life and no matter how hard times can be. I am also very thankful for my parents who supported and always believe in me.

Contents

List of Figures

To my four parents

Susanne, you have a place in our hearts and you will stay in our memories forever.

Part I

Quantum simulation of particle creation in curved spacetime

Conversion of vacuum fluctuations into real particles was first predicted by L. Parker considering an expanding universe, followed in S. Hawking's work on black hole radiation. Since their experimental observation is challenging, analogue systems have gained attention in the verification of this concept. Here we propose an experimental set-up consisting of two adjacent piezoelectric semiconducting layers, one of them carrying electron loaded dynamic quantum dots (DQDs), and the other being p-doped with an attached gate on top, which introduces a space-dependent layer conductivity. The propagation of surface acoustic waves (SAWs) on the latter layer is governed by a wave equation with an effective metric. In the frame of the DQDs, this space- and time-dependent metric possesses an acoustic horizon for SAWs and resembles that of a two-dimensional non-rotating and uncharged black hole to some extent. The non-thermal steady state of the DQD spin indicates particle creation in form of piezophonons.

This part of the thesis has evolved from my master thesis with the title *Analogue Hawking radiation with surface acoustic waves* (in German *Analoge Hawking-Strahlung mit akustischen Oberflächenwellen*) in the same group. As part of my PhD, we developed a vastly improved measurement scheme and worked out some more details leading to a slight reinterpretation regarding the particle creation. This work got published with the title *Quantum simulation of particle creation in curved space-time* in PLoS ONE 15(3): e0229382 as part of the PLoS ONE collection *Open Quantum Computation and Simulation*.

After the introduction, Sec. 2 gives a recap of the work done during my master thesis. This sets the necessary background to understand the development and clearly demarcates the contributions done during my master's and PhD. Sec. 3 contains further details, with the main focus put on the proposed detector for the created particles. In Sec. 4 the slight reinterpretation is given. A perturbative approach given in Sec. 6, which employs the Bloch-Redfield equation derived in Sec. 5, finally gives indications for the validity of our model. This part is concluded with Sec. 7.

1 Introduction: Same equations – same physics

"*True is not what makes sense to us, true is what Nature confirms.*"

D. Schönemann

Galileo Galilei is considered as the founder of modern science. He added and established the conduct of appropriate experiments to Aristotle's approach of collecting data by observation[1] in order to study Nature. Experimentation takes an essential role in modern science by being indispensable for the verification of a theory.

For certain subjects, such as astronomy, planning and performing appropriate experiments seems virtually hopeless, even in the long-term future. One popular example is Stephen Hawking's famous prediction of Hawking radiation [2], i.e. the emission of thermal radiation by a black hole. The temperature T_H of this radiation is connected to the mass M of the black hole via

$$T_H = \frac{\hbar c^3}{8\pi G k_B} \frac{1}{M}.$$

For the supermassive black hole Sagittarius A* in the center of the milky way, which is the closest (known) astrophysical one to the Earth, the temperature is predicted to be $T_H \sim 10^{-14}$ K – hence a direct observation in a 2.7 K "hot" cosmic background seems virtually impossible.

Scientists longingly hope for further investigation on Hawking radiation since it may provide clues to resolve unanswered problems such as the trans-Planckian problem [3], or the no-hair theorem and the related information paradox.[2] The possibility to produce micro black holes in near-future particle accelerators is also discussed [5, 6, 7], but was not successful yet [8].

One way out of this hopeless situation was porposed by W. Unruh, who was the first to consider black hole analogues [9]. As he describes in [10] and is illustrated by Fig. 1.1, a waterfall shares some qualitative features with an astrophysical black hole: The locus of points, which separates the upstream subsonic flow with $v(\mathbf{r}) < c$ from the downstream supersonic flow with $v(\mathbf{r}) > c$ with the local fluid velocity $v(\mathbf{r})$ and the speed of sound c, cannot be passed by sound waves in the supersonic region. Hence, the crossover between sub- and supersonic flow, where $v(\mathbf{r}) = c$, acts as unidirectional surface for sound waves and traps them in the downstream region. Furthermore, sound waves undergo a redshift while traveling upstream in the subsonic region. Due to these close analogies with astrophysical black holes, where the event horizon can be passed only in one direction and separates the interior of the black hole from the outside, these system are called *dumb holes* (in German *stumme Löcher*) sometimes.

While it can be very helpful to have this picture together with its qualitative features in mind when looking for an alternative black hole analogue, the true justification for a system to behave to some extent like a black hole requires quantitative arguments: Unruh showed [9] that the propagation of sound waves in an irrotational, stationary and converging fluid, flowing with spherically symmetric velocity $v(r)$, is governed by an effective metric matching that of a gravitating spherical, non-rotating massive body in Painlevé-Gullstrand coordinates [12]

$$\mathrm{d}s^2 = -\left[c^2 - v^2(r)\right]\mathrm{d}t^2 + 2v(r)\mathrm{d}r\mathrm{d}t + \mathrm{d}r^2 + r^2\mathrm{d}\Omega^2, \tag{1.1}$$

[1] It is said that Aristotle did not perform experiments, but instead relied on pondering about Nature. Fun fact: He was strongly convinced that men have more teeth than women [1].

[2] See, for example, [4] for a pedagogical introduction.

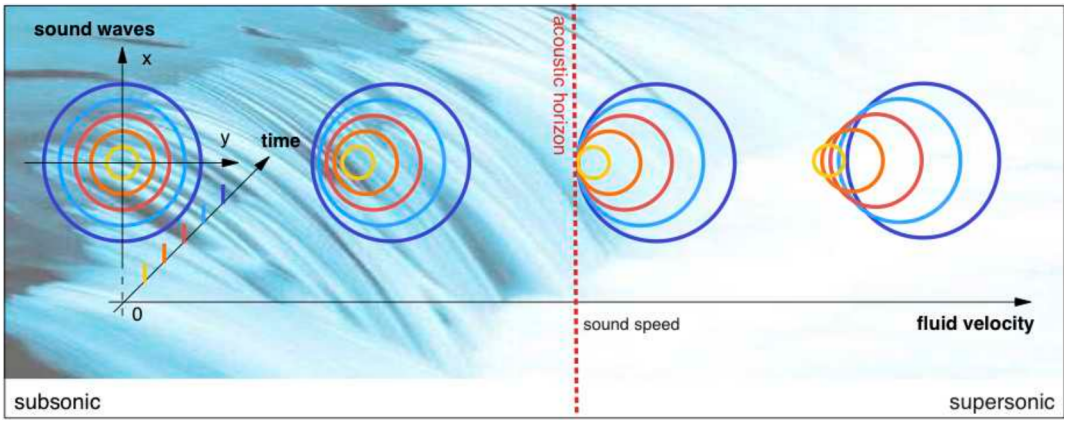

FIGURE 1.1: Shown is the appearance of an acoustic horizon in a long water fall. Sound waves propagating in the water cannot reach the upstream region with subsonic flow, $v(\mathbf{r}) < c$, from the downstream region with supersonic flow, $v(\mathbf{r}) > c$, which thus acts similar to the interior of a black hole. The figure is taken from [11].

which indeed possesses a horizon wherever $c^2 - v^2(r) = 0$, confirming that this system is suitable for mimicking a black hole. Furthermore, regarding the emission of analogue Hawking radiation, he argued that after quantization of the sound field, this result can be directly transferred to the quantum mechanical excitations expressed via a quantum field which propagates on the effective metric with line element given by Eq. (1.1), concluding that the same steps which led Hawking to his famous result, also lead to the prediction of thermal Hawking-like radiation in form of phonons, which is emitted from the acoustic horizon.

Since Unruh's original proposal, a vast number of black hole analogous have been proposed, for instance in liquid Helium [13], dc-SQUID transmission lines [14], electromagnetic waveguides [15], water waves [16, 17, 18], hydrodynamic microcavity polariton flow [19], optical set-ups [20, 21, 22, 23] and Bose-Einstein condensates [24, 25, 26].

The use of analogue systems is of course not restricted to black holes, but can be found in almost all areas of physics.[3] Here, a few further examples and their possible analogues related to black holes will be briefly mentioned: The ubiquitous presence of vacuum fluctuations is arguably one of the most surprising effects of quantum theory. Their existence is indirectly observable via the modification of the electron's magnetic moment [28] or the Lamb shift of an atomic spectrum [29]. A more direct access could be accomplished by converting the virtual particles into directly observable real ones. Such particle creation is predicted to take place under various conditions such as the dynamical Casimir effect [30, 31] and related circumstances [32], during the expansion of the universe [33], or due to the presence of a black hole's event horizon [2]. While the dynamical Casimir effect has been experimentally verified [34], direct experimental observation of particle creation in an expanding universe is challenging. Systems analogue to particle creation in the dynamical Casimir effect [35, 36] and in an expanding universe [37, 38, 39, 40, 41, 42] have been proposed in setting ranging from trapped ions and BEC to photonic crystal fibers.

All of these analogue systems work according to one common basic and actually very simple principle: *Same equations means same physics — mathematics does not care about the physical context.*

[3] Analog and digital quantum simulations run on a quantum computer currently show great potential. See, for example [27].

2 Analogue Hawking radiation with surface acoustic waves – the story so far

We stress that this section presents all the contributions to our paper PLoS ONE 15(3): e0229382 which were exclusively obtained during my master thesis. This includes the derivation of the effective metric, which governs the propagation of surface acoustic waves (SAWs) on a piezoelectric semiconducting substrate. Under appropriate circumstances, this effective metric will give rise to an acoustic horizon. From this, we conclude the emission of analogue Hawking radiation in form of phonons and derive the associated Hawking temperature.

Later contributions obtained during my PhD, such as the detection scheme, are presented in later sections.

2.1 Basic building blocks

This section contains the fundamental requirements to generate an acoustic horizon for SAWs. In adapting the original proposal of Ref. [9] to solid-state devices, the difficulty lies in designing a moving medium for wave propagation. This can be circumvented by having a space- (and time-) dependent wave speed $c(x,t)$. An observer moving with a proper speed v along the waves will eventually experience the crossover between subsonic and supersonic propagation - a direct route for the formation of an acoustic horizon. Here, the local modulation of the SAW speed can be achieved by exploiting its dependence on the substrate conductivity [43, 44, 45, 46, 47, 48], which can be changed locally by biasing a thin gate attached to the piezoelectric p-type semiconducting substrate (see, e.g. Ref. [49]): Biasing the gate with a voltage induces a 2DEG in the surface of the substrate in the vicinity to the gate, changing the substrate conductivity. A properly moving detector experiences an acoustic horizon for SAWs at the crossover $c(x,t) = v$, from which analogue Hawking radiation in form of phonons is permanently emitted.

In the following, we derive the effective metric and present the set-up.

2.1.1 Effective metric

Consider the one-dimensional propagation of SAWs along the x-direction with a space-dependent speed of sound $c(x)$. With u denoting the SAW amplitude, the dynamics follows the usual wave equation (see, e.g. [50])[4]

$$\frac{\partial^2 u}{\partial^2 t} = \frac{\partial}{\partial x}\left(c^2(x)\frac{\partial u}{\partial x}\right). \tag{2.1}$$

Comparing this equation with the equation for a scalar and massless field ϕ in a spacetime described by a metric $g_{\mu\nu}$,

$$\partial_\mu\left(\sqrt{|g|}g^{\mu\nu}\partial_\nu\right)\phi = 0,$$

[4]The SAW-type solutions (Rayleigh, Lamb and Love waves) are only obtained from the usual wave equation by taking appropriate boundary conditions into account. However, these boundary conditions effectively put constraints on the SAW amplitude and velocity. As a result, the SAW dynamics still follow the usual wave equation, only with the SAW speed differing from the bulk value.

one can read an effective metric in the rest frame of the substrate (in the following referred to as "lab frame"), which gives the line element

$$\mathrm{d}s^2 = -c^2(x)\mathrm{d}t^2 + \mathrm{d}x^2. \tag{2.2}$$

The Galilean transformation[5] from the lab frame to the reference frame of an observer moving at speed v along the x-direction is accomplished by the substitutions

$$t \to t \quad , \quad x \to x + vt \tag{2.3}$$

$$\frac{\partial}{\partial t} \to \frac{\partial}{\partial t} - v\frac{\partial}{\partial x} \quad , \quad \frac{\partial}{\partial x} \to \frac{\partial}{\partial x} \tag{2.4}$$

in Eq 2.1. The effective metric describing the SAW dynamics in the moving reference frame leads to the line element

$$\mathrm{d}s^2 = -\left[c^2(x - vt) - v^2\right]\mathrm{d}t^2 + 2v\mathrm{d}t\mathrm{d}x + \mathrm{d}x^2. \tag{2.5}$$

While the lab frame lacks an acoustic horizon, see Eq. (2.2), the effective metric in the moving reference frame matches Painlevé-Gullstrand's metric revealing an acoustic horizon where $c^2 - v^2 = 0$. This distinct behavior takes the observer-dependent notion of particles, known from quantum field theory, to extremes: The moving observer experiences the presence of phonons traveling on the substrate, even if the lab observer measures the vacuum state free of any phonons. For the particular line element Eq. (2.5) describing a black hole, this effect is analogous to the Hawking effect, and the excess phonons form the analogue Hawking radiation.

As noted above, the Hawking effect is based on vacuum fluctuations, which themself originate from the quantum mechanical commutation relations of the quantized field and its conjugate variable [51]. For a system with analoguous lineelement [15], it was already shown that the correct commutation relations are fulfilled. The presence of analogue Hawking radiation and the calculation of the related temperature can be demonstrated from several standpoints (see, e.g. [2, 51, 52, 53, 54, 55]). As was shown in [54], the existence of an apparent horizon with a non-vanishing surface gravity

$$\kappa_g = \left|\frac{\partial c}{\partial x}\right|_{c^2=v^2} \tag{2.6}$$

is accompanied by Planckian Hawking radiation with a temperature given by

$$T_H = \frac{\hbar\kappa_g}{2\pi k_B} \tag{2.7}$$

for frequencies greater than κ_g.

2.1.2 SAW dynamics

The propagation of SAWs can be controlled by their interaction with a 2DEG in the substrate [43, 44, 45, 46, 47, 48]. Here we follow Ref. [47], which presented a detailed calculation of

[5] Strictly speaking, the lab and moving reference frame are connected via a Lorentz transformation. As their relative speed v will be essentially given by the speed of sound of SAWs, which is much smaller than the vacuum speed of light, the Lorentz transformation can be sufficiently approximated by a Galilean transformation.

SAW propagation on a piezoelectric semiconductor with a *homogeneous* electron gas, and extend their results to the inhomogeneous case.

Due to the piezoelectric effect the SAW is accompanied by an electric field, thus interacting with the 2DEG and inducing currents that dissipate energy due to Ohmic losses. The piezoelectric effect is taken into account by introducing a space dependent charge density n_s that obeys Maxwell's equation

$$\frac{\partial D}{\partial x} = -q n_s \tag{2.8}$$

with the elementary charge denoted by $q = |q|$ (e will be reserved for the piezoelectric constant) and where D is the electric displacement field. The induced current density is given by

$$j(x,t) = -q \left[n_{\mathrm{2DEG}}(x) + f n_s(x,t) \right] \mu E(x,t), \tag{2.9}$$

where μ denotes the electron mobility, f accounts for the part of the induced space charge being in the conduction band (for a calculation of f, see [47]), n_{2DEG} denotes the *time-independent* density of the 2DEG induced by an attached gate and $E(x,t)$ is the electric field. The time-independence of n_{2DEG} is necessary in order to recover the usual wave equation for the SAW amplitude. Diffusion currents $\sim k_B T \frac{\partial}{\partial x} \left(n_{\mathrm{2DEG}} + f n_s \right)$ due to spatial inhomogeneous charge distribution can be neglected in the low-temperature limit we propose to work in. The total charge density contributing to the electric current is given by

$$\rho = -q \left[n_{\mathrm{2DEG}} + f n_S \right]. \tag{2.10}$$

Using the continuity equation for the charge current and density

$$\frac{\partial \rho}{\partial t} + \frac{\partial j}{\partial x} = 0 \tag{2.11}$$

and the time-independence of n_{2DEG}, one can derive an equation relating D and E,

$$-\frac{\partial^2 D}{\partial x \partial t} = \mu \frac{\partial}{\partial x} \left(\left[f \frac{\partial D}{\partial x} - q n_{\mathrm{2DEG}} \right] E \right). \tag{2.12}$$

Making a plane-wave ansatz

$$E = E_0 \exp\left\{ i \left(k(x) - \omega t \right) \right\} \tag{2.13}$$

$$D = D_0 \exp\left\{ i \left(k(x) - \omega t \right) \right\}, \tag{2.14}$$

and neglecting terms with the product $E \cdot D$[6], one can write $D = \varepsilon_{\mathrm{eff}} E$ with an effective permittivity

$$\varepsilon_{\mathrm{eff}} = \frac{\mu q}{\omega} \left[\frac{\partial_x n_{\mathrm{2DEG}}}{\partial_x k} + i\, n_{\mathrm{2DEG}} \right], \tag{2.15}$$

where ∂_x abbreviates the spatial derivative. The equations of state for a piezoelectric material

$$T = dS - eE \tag{2.16}$$

$$D = eS + \varepsilon E, \tag{2.17}$$

[6]Following Ref. [47] these terms can be neglected if the strain amplitude $S \ll \varepsilon v/(e\mu) \sim 10^{-6}$ for GaAs. As the upper layer is not driven, the strain amplitude is estimated to be in the 10^{-9}-regime.

where T and S denote stress and strain constants, d is the elastic constant and e is the piezoelectric constant, can be simplified to $T = d_{\text{eff}} S$ with an effective elastic constant

$$d_{\text{eff}} = d\left[1 + \frac{e^2}{\varepsilon d}\left(1 - \frac{\varepsilon_{\text{eff}}}{\varepsilon}\right)^{-1}\right]. \tag{2.18}$$

This equation illustrates the effect of piezoelectric stiffening, i.e. a dressed elastic constant due to the piezoelectric effect [56]. The equation of motion for the SAW amplitude u is given by

$$S = \frac{\partial u}{\partial x} \text{ and } \frac{\partial T}{\partial x} = \rho \frac{\partial^2 u}{\partial t^2}, \tag{2.19}$$

leading, with Eq. (2.18), finally to the wave equation of Eq. (2.1) with the SAW speed given by

$$c(x) = \text{Re}\left(\sqrt{\frac{\text{d}_{\text{eff}}}{\rho}}\right). \tag{2.20}$$

Note that the RHS of Eq (2.20) also depends on the SAW speed via $\partial_x k(x) = \omega/c(x)$. Thus, Eq. (2.20) is an algebraic equation and can in principle be solved for $c(x)$, which would give an expression for the SAW speed in terms of the 2DEG density $n_{\text{2DEG}}(x)$. Next, the 2DEG density, as it is induced by a voltage biased gate attached to the semiconducting substrate, will be approximated. Finally, after computer-aided numerical solution for $c(x)$ the associated Hawking temperature Eq. (2.7) can be determined. However, later it turned out that a rather easy approximation can be done, which allows for an analytic solution of $c(x)$. This approach was pursued during my PhD and will be presented in Sec. 3, but the result is already shown in Fig. 2.1.

2.1.3 2DEG density modulation

The transistor is an every-day device which allows for controlling the conductivity of the contained semiconductor. In this work, a MOSFET-like layered structure comprising a thin insulator and a normal-metal gate on top of the semiconducting substrate is used to induce a 2DEG in the vicinity of the semiconductor–insulator interface on the semiconducting site.[7] In this section, we describe the charge distribution in the 2DEG, which results if the semiconductor is only *partially* covered by the normal-metal gate (see Fig. 2.2).

As a bare approximation the 2DEG is assumed to distribute homogeneously over the area of the gate,

$$n_0(x) = n\,\Theta(-x)\ , \tag{2.21}$$

with a density amplitude n proportional to the applied gate voltage V_G [49], and the Heaviside step function $\Theta(x)$. However, the actual 2DEG is smeared out and its density n_{2DEG} is smoothed close to the diode's edge (illustrated in Fig 2.1). We take this into account by convoluting the approximated density $n_0(x)$ and a Gaussian with a FWHM denoted by κ_s^{-1},

[7] There is excellent literature about the functionality of semiconductor devices, such as MOSFETs. See, for example, [49] or [57].

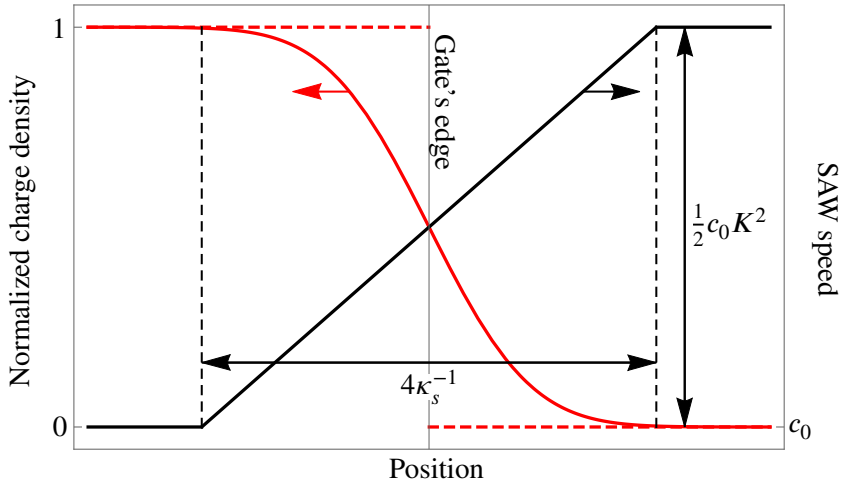

FIGURE 2.1: Spatial profiles around the gate's edge. Shown are the densities of the approximate (dashed red) and actual, smeared out (solid red) charge distribution of the induced 2DEG. The latter one arises from the first one due to screening effects inside the semiconducting substrate, which smoothen the charge density in a narrow region of approximate thickness $4\kappa_s^{-1}$ around the gate's edge with the screening length κ_s^{-1}. The corresponding SAW speed $c(x)$ (black) approximated from Eq 2.20 (see Sec. 3 for details) takes the values c_0 and $c_0(1 + K^2/2)$ with the piezoelectric coupling constant K^2 in the region with high and low 2DEG density, respectively, and approximately aligns linearly in the transition region.

reading

$$G(x) = A \exp\left\{-(\kappa_s x)^2\right\}, \tag{2.22}$$

$$n_{\mathrm{2DEG}}(x) = (G * n_0)(x) \tag{2.23}$$

$$= \frac{n}{2}\left[1 - \operatorname{erf}\left(\kappa_s x\right)\right], \tag{2.24}$$

where "$*$" denotes the convolution operation. The normalization coefficient A guarantees charge conservation,

$$\int_{-\infty}^{\infty} \left[n_{\mathrm{2DEG}}(x) - n_0(x)\right] \mathrm{d}x = 0. \tag{2.25}$$

The phenomenological parameter κ_s^{-1} should be of the order of the screening length of the substrate material which, for moderate doping of the p-type semiconducting substrate, is typically of the order of 10^{-8} m [58, 59].

2.2 Results

The basic building blocks mentioned in the preceding section are now combined to present one possible set-up suitable as a black hole analogue with the purpose to detect analogue Hawking radiation in form of phonons.

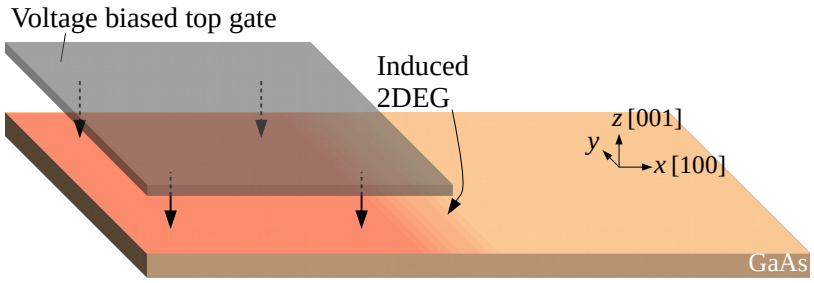

FIGURE 2.2: Partial sketch of the experimental set-up intended to serve as basis of an analogue black hole. The two-dimensional electron gas (2DEG), which is induced in the MOSFET-like layered structure, gives rise to a space-dependent speed of sound in the GaAs substrate – a direct route to the formation of an acoustic horizon at the crossover between sub- and supersonic motion in the reference frame of a moving observer, according to Eq. (2.5). The moving observer as well as the cryogenics are not shown.

Proposed experimental set-up and estimated Hawking temperature

We proposed that combining the three main ingredients from the preceding section in a set-up sketched in Fig. 2.2 is sufficient to create an acoustic horizon for SAWs experienced by a moving observer. The set-up consists of a GaAs substrate, which is both piezoelectric and semiconducting, to which a normal-metal gate with (almost) arbitrary dimension[8] is attached. From the computer-aided solution of Eq. (2.20) it follows that when biasing this gate with a voltage $V_G \approx 10$ V,[9] the SAW speed approaches a value of $c_0 = \sqrt{d/\rho}$ beneath the gate inside the 2DEG and a value of $c_0(1 + K^2/2)$ in the region with vanishing 2DEG. Here, d, ρ and $K^2 = e^2/(\epsilon d)$ denote the elastic constant, substrate density and piezoelectric coupling constant, respectively, with the piezoelectric constant e. An observer moving with appropriate speed $c_0 < v < c_0(1 + K^2/2)$ along the x-direction experiences the permanent emission of analogue Hawking radiation in form of phonons from the acoustic horizon occurring at $c(x) = v$, even without need of driving the substrate with SAWs due to the observer-dependent notion of particles, as mentioned in Sec. 2.1.1.

For a GaAs piezoelectric semiconducting substrate with material constants $K^2 \sim 10^{-4}$ [47], $c_0 \sim 10^3$ ms^{-1} [60], and $\kappa_s \sim 10^9$ m^{-1} [61], the maximal Hawking temperature according to Eq. (2.7) is numerically found to be of the order of 10^{-3} K. As experiments are usually conducted at the 1 K regime, distinguishing this low Hawking temperature from the background radiation may be challenging. We note, however, that no optimization was attempted. Different piezoelectric materials (piezoelectric coupling constants up to 3 orders of magnitude larger have been achieved [62]) and alternative gate set-ups are possible routes to increase the temperature of the emitted radiation.

[8] The set-up must of course fit into appropriate cryogenics. But with todays lithographic techniques a normal-metal gate with 50 nm extension is possible. What is important for this work is the spatial change from high to low conductivity, as it occurs at the gate's edge – and this is independent of the gate's size.

[9] On the one hand, a MOSFET can be destroyed when applying a too high voltage, which is usually of the order of 20 V [49, 57]. On the other hand, a 2DEG is induced only if the gate voltage exceeds a certain threshold, which depends on material properties and is typically of the order of 1 V.

Strategy for detection of analogue Hawking radiation

The absence of the acoustic horizon in the lab frame renders the use of static[10] detectors such as IDTs (interdigitated transducers) inapplicable for the detection of the analogue Hawking radiation. Instead, since the acoustic horizon is only present in the moving reference frame – an ultimate manifestation of the observer-dependent notion of particles – a moving detector for phonons is required as well. To our knowledge, at the time my Master thesis was written, neither such a detector nor an appropriate detection scheme were available. In what follows, one promising route we conceived is presented. However, due to lack of time at the end of my master's, it unfortunately remained a rather immature train of thought.

Our proposal is based on the piezoelectric effect: As mechanical wave, a SAW is accompanied by an electric wave when propagating on a piezoelectric substrate. This fact is routinely used to trap single electrons and/or holes in the minima of the wave in order to drag and transport them with the SAW, a construct known as electron/hole loaded dynamic quantum dot (DQD) [63, 64, 65].[11] Such a DQD should move on a second, adjacent but spatially separated piezoelectric semiconducting substrate, called measurement substrate, so that its speed v is constant and does not follow the speed profile $c(x)$. The speed v could be chosen appropriately by attaching a sufficiently sized and voltage-biased gate on the measurement substrate as well. Alternatively, since the SAW speed depends on the thickness of the substrate it propagates on [66][12] – similar to the behavior of water waves approaching the shore –, the thickness of the measurement substrate can be chosen appropriately.

The piezoelectric effect does not only allow for the realization of DQDs, but also for the indirect measurement of the Hawking phonons: In a piezoelectric, phonons and photons are expected to be intrinsically indivisible and correlated to some extent. More precisely: Due to the piezoelectric interaction between phonons and photons, neither of them are eigenstates of their respective unperturbed Hamiltonians. Consequently, they have finite lifetimes, after which they evolve into superpositions of the true, yet unknown, eigenstates of the full Hamiltonian. These eigenstates are in turn superpositions of different phonon and photon Fock states as well: Consequently, the Hawking phonons would be accompanied by Hawking photons. Furthermore, if the participating photons would not be confined to the first substrate containing the acoustic horizon, but instead could overcome the spatial separation to the measurement substrate, they could interact with the electrons in the DQDs. Eventually, the information about the Hawking photons and thus the Hawking phonons as well, which would be encoded in the electrons' state could be gained using standard phase measurements.

While the realization of DQDs is well established, the remaining description is, frankly speaking, superficial and lacks a fair amount of detail: What are the exact eigenstates of a piezoelectric, expressed in phonon and photon Fock states, and vice versa? To what extent are the Hawking phonons and photons correlated? Can the evanescent electric waves and the associated photons stemming from the Hawking phonons really reach the measurement substrate and thus the DQD? If so, what is their interaction, and how is the state of the electron in the DQD affected? What are the associated time scales, especially compared to the decoherence and relaxation times of the electron loaded DQDs, and how do they depend on the Hawking temperature? ...

[10] In this context, static means to be at rest with respect to the substrate.

[11] DQDs are sometimes also called moving quantum dots.

[12] Actually, our very first approach towards the required spatial modulation of the SAW speed was based on the thickness dependence of the SAW speed. However, it turned out that the calculation of the SAW speed in a substrate with space-dependent thickness is very cumbersome.

Herewith, the contributions to our final publication PLoS ONE 15(3): e0229382, which were done during my Master thesis, are finished. Our final detection scheme with a moving detector is presented in Sec. 3.2.

3 Finalizing the project

Note that from this section on the contributions to the present project were obtained during my PhD.

In the following section, details that were elaborated compared to my Master thesis, are presented. This contains a rather easy approximate solution for the SAW speed and estimation of the Hawking temperature. Furthermore, the moving detector, initially intended for detection of analogue Hawking radiation in form phonons, is presented.

3.1 Approximation of the SAW speed

For convenience, the 2DEG density is denoted by n in the following. Eq 2.20 gives an *algebraic* relation between the SAW speed and the 2DEG density. Consequently, $c(x)$ only depends *locally* on $n(x)$ and $\partial_x n(x)$: As $n(x)$ and $\partial_x n(x)$ only change at the gate's edge on a length scale κ_s^{-1}, $c(x)$ changes on the same length scale as well. This can be seen as follows. In principle, an expression for the SAW speed $c(x)$ in terms of n can be obtained from the implicit equation Eq. 2.20. I.e. $c(x) = f(n, \partial_x n)$ with a particular function f. Derivation of this equation with respect to x gives

$$\frac{\partial c}{\partial x} = \frac{\partial f}{\partial n}\frac{\partial n}{\partial x} + \frac{\partial f}{\partial\left(\partial_x n\right)}\frac{\partial^2 n}{\partial x^2}. \tag{3.1}$$

Expanding $n(x)$ (see Eq. 2.24) in a Taylor series around the gate's edge $x = 0$ up to third order and solving for the roots, one obtains a value of approximately $4\,\kappa_s^{-1}$ for the size of the region, where $n(x)$ changes from 0 to its maximum value. Outside this region $\partial_x n$ and $\partial_x^2 n$ vanish. According to Eq. 3.1, the SAW speed consequently only changes around the gate's edge, too. For wavelengths much longer than the screening length, $\lambda \gg \kappa_s^{-1} \sim 1$ nm, a good approximation for $c(x)$ is a piecewise constant behavior in the regions $|x| > 2\,\kappa_s^{-1}$, and a linear adjustment in between, $|x| < 2\,\kappa_s^{-1}$. Deep inside the gate, i.e. for $x < -2\,\kappa_s^{-1}$, the corresponding value for the SAW speed is obtained by letting $n \to \infty$ and $\partial_x n \to 0$ in Eq. 2.15, giving $d_{\text{eff}} = d$ (see Eq. 2.18) and consequently $c = c_0 = \sqrt{d/\rho}$ (see Eq. 2.20). In the region far away from the gate, i.e. $x > 2\,\kappa_s^{-1}$, the 2DEG density is vanishing $n = \partial_x n = 0$, and, with Eqs. (2.15-2.20), give $c = c_0\sqrt{1+K^2} \approx c_0\left(1 + \frac{1}{2}K^2\right)$, where a small piezoelectric coupling constant $K^2 = e^2/(\varepsilon d) \ll 1$ is assumed, which is valid for nearly all piezoelectric materials [48]. This approximation was validated using the computer-aided solution of Eq. (2.20).

Hence, the gradient of $\partial_x c$ determining the Hawking temperature via Eq. (2.7) can be approximated to

$$\max\left\{\left|\frac{\partial c}{\partial x}\right|\right\} = \frac{1}{8}\kappa_s K^2 c_0. \tag{3.2}$$

3.2 Novel detection strategy

In this part the moving detector will be described first roughly and then with some more details step-by-step afterwards.

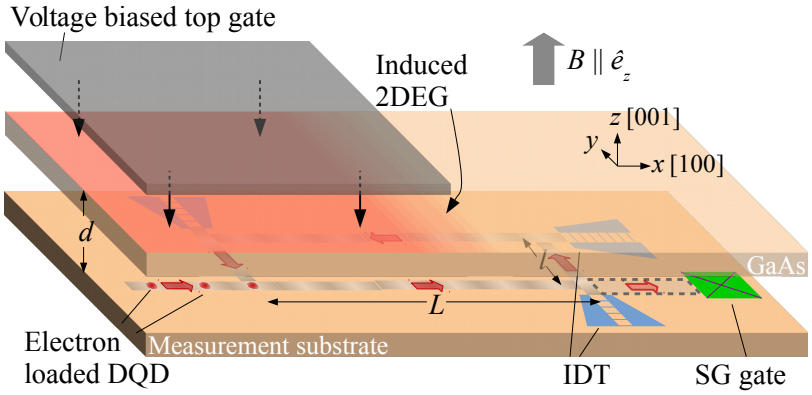

FIGURE 3.1: Partial sketch of the experimental set-up. The formation of the acoustic horizon for surface acoustic waves on the upper GaAs layer is due to the inhomogeneous two-dimensional electron gas (2DEG) induced by the attached gate. The electrons in the dynamic quantum dots (DQDs) on the lower GaAs layer (measurement substrate) serve as thermometers for the Hawking temperature: Thermal occupation of the two electron-spin states in the DQDs is expected due to an effective spin-phonon interaction with Hawking phonons. A Stern-Gerlach (SG) gate allows for the readout of the electronic spin. The arrangement of the interdigitated transducers (IDTs) serves as a storage ring for the DQDs in order to provide enough time for thermalization. Not shown is the cryogenics.

3.2.1 Final set-up

Fig. 3.1 shows the full, final set-up, which is the initial one (see Fig. 2.2) extended by the moving detector. It comprises several DQDs transporting photogenerated electrons and propagating in an adjacent piezoelectric semiconducting substrate (labeled as measurement substrate). A magnetic field along the [001] crystallographic axis of GaAs leads to a Zeeman-splitting of the electron-spin states. The thermal occupation among the spin states due to interaction between the thermal Hawking phonons and the electrons, reveals the Hawking temperature and can be read out by a Stern-Gerlach (SG) gate [67, 68], which converts spin into current paths due to the Stern-Gerlach effect. The arrangement of IDTs serves as storage ring for the electrons and enables for a sufficiently long interaction time required for thermalization, which is estimated to ~ 1 s.

3.2.2 Inter-substrate interaction

As already mentioned, due to the piezoelectric effect mechanical waves and phonons are accompanied by electric fields.[13] While the mechanical waves are confined to the substrate they propagate in, the electric fields are present also outside the substrate as evanescent fields, typically decaying exponentially on a length scale given by the wavelength of the mechanical wave.[14] Consequently, in a set-up composed of two adjacent piezoelectric substrates, mechanical waves are not restricted entirely to one substrate, but are shared among them via mutual piezoelectric interaction [69, 72].

[13] Since the propagation of acoustic waves is typically 4 to 5 orders of magnitude slower than that of electromagnetic waves, the magnetic field originating from a time-dependent electric field can be neglected, which is called the quasi-static approximation [69].

[14] The explicit calculation of the mechanical and electric fields in presence of boundaries can be arbitrarily cumbersome. See, for example [43, 45, 70, 71] and references therein.

This property allows for a controlled propagation of DQDs with constant speed v on the measurement substrate while interacting with Hawking phonons emitted from the acoustic horizon on the other substrate.

3.2.3 Approximate energy levels in a DQD

In this section, the energy levels of an electron which is trapped inside a DQD and additionally exposed to an external magnetic field, are approximated. First, the DQD without magnetic field will be considered. The magnetic field will then be treated as perturbation, and at the very end the electron spin will be included. On the one hand, it is possible to calculate the energy spectrum exactly, as will be shown in appendix 7. The approach pursued here, on the other hand, uses concepts already known and established, thereby closely following the spirit of this whole part of the thesis.

As was experimentally demonstrated in [63] for instance, an array of square formed DQDs can be realized by interfering two orthogonally traveling coherent SAW beams. The coordinate system will be chosen such that the beams point along the x- and y-axis, respectively. In the rest frame of the DQD the electric potential induced by the SAWs due to the piezoelectric effect can be approximated as [71]

$$V_{\mathrm{SAW}}(x, y) = U_0 \cos(kx) \cos(ky), \tag{3.3a}$$

where the potential amplitude U_0 is related to the actual SAW amplitude and the piezoelectric constant and k denotes the wave number of the coherent SAW beams. An electron, which is confined to the xy-plane[15] and trapped inside the DQD, is described by the Hamiltonian

$$H = \frac{1}{2m}\left(p_x^2 + p_y^2\right) + V_{\mathrm{SAW}}(x, y). \tag{3.3b}$$

Expanding the potential around its minimum up to second order gives the Hamiltonian of a two-dimensional, symmetric harmonic oscillator with resonance frequency

$$\omega = \frac{2\pi}{\lambda}\sqrt{\frac{U_0}{m}}, \tag{3.3c}$$

where λ is the wavelength of the SAW beams and m denotes the effective mass of the electron trapped inside the DQD. The low-energy spectrum of the orbital states of the electron in the DQD is thus approximately given by the equidistant spectrum of an harmonic oscillator with an energy splitting $\hbar\omega$.

If a magnetic field with strength B_0 is applied perpendicular to a 2DEG of *free* electrons, the electronic energy spectrum is changed and given by Landau levels with energy splitting

$$\hbar\omega_B = \frac{\hbar e B}{m},$$

where ω_B denotes the usual cyclotron frequency. The characteristic length scale is given by the magnetic length

$$l_B = \sqrt{\frac{\hbar}{eB_0}},$$

[15] In Ref. [63] a quantum well was used. Alternatively, an attached and voltage biased gate inducing a 2DEG could be employed as well, which can also serve as modulator for the speed v of the moving detector.

which gives the spatial extension of the quantum state in the lowest Landau level. For a magnetic field $B_0 = 1$ T, the magnetic length for an electron is $l_B \approx 2.5 \times 10^{-8}$ m. The extension of a DQD is given by the wavelength λ of the coherent SAW beams. For typical values of $\lambda \sim 10^{-6}$ m, the DQD is much larger than l_B for $B_0 = 1$ T. This allows for a qualitative treatment of the low-energy spectrum of the electrons trapped in a DQD exposed to a magnetic field: The electrons can be treated as free electrons subjected to the magnetic field, which leads to the usual Landau levels with energy splitting $\hbar\omega_B$. In appendix 7 the exact energy spectrum will be calculated and it turns out that this rather rude looking approximation is not bad.

So far, the electron spin was neglected. The magnetic field leads to the usual Zeeman splitting $\Delta = g\mu_B B$ between the spin states with the Bohr magneton $\mu_B = \hbar e/(2m)$. For free electrons with $g = 2$, this coincides with the Landau splitting $\hbar\omega_B$. However, in real metals this does not happen, since first, the effective mass of the electrons determines the cyclotron frequency, and second, the Landé g-factor can vary due to effects of the band structure. For GaAs the Zeemann splitting is about 68 times smaller than the cyclotron energy. As a result, the smallest energy scale is given by the Zeemann energy, and the low-energy spectrum of the electron in the DQD, relevant for the interaction with the Hawking phonons as discussed further below, just consists of the two split spin states.

3.2.4 Measurement: thermalization and readout

With values of the potential amplitude $U_0 \sim 40 - 600$ meV [73, 74], SAW wavelength $\lambda \sim 10^{-6}$ m determining the DQD size, effective electron mass $m = 0.067\, m_e$ and Landé g-factor $g = 0.44$ for GaAs, and magnetic field $B_0 = 1$ T, the energy separation $\hbar\omega$ of the electron orbital states in the DQD, the cyclotron energy $\hbar\omega_B$ and Zeemann splitting Δ are of the order of $\hbar\omega \sim 1$ meV, $\hbar\omega_B \sim 1$ meV, $\Delta \sim 10$ μeV. With a Hawking temperature of $T_H \sim 1$ μK, corresponding to $k_B T_H \sim 0.1$ meV, the influence of the thermal Hawking phonons on the equilibrium state of the electrons in the DQDs is negligible. As mentioned above, the Hawking temperature could be increased by using other substrate materials with higher piezoelectric coupling constants (up to 3 orders of magnitude have been achieved [62]) and alternative gate set-ups, rendering the measurement of the Hawking temperature feasible. This is accessible via an ensemble measurement of the occupation of the electron states.

DQDs are proposed as platform to transport quantum information encoded in the electron spin [67]. In compliance with DiVincenzo's criteria [75] regarding the qubit readout, a proposal for single-qubit measurement, which exploits the Stern-Gerlach effect to convert spin into current paths, is already available [67, 68]. This is in contrast to the electron's behavior as harmonic oscillator[16] which in principle allows for tomographic reconstruction of the quantum state [76, 77], but the available measurement schemes must be adapted to the set-up at hand. Furthermore, even with increased Hawking temperature the thermal occupation of the harmonic oscillator states is far less suited than the thermal occupation of the spin states since $k_B T_H \sim \Delta \ll \hbar\omega, \hbar\omega_B$.

The use of Stern-Gerlach gates (or other spin-to-charge conversion methods) allows for the readout of the electron spin from which the Hawking temperature can be computed. Thermalization among the spin states with the thermal Hawking phonons is mediated via electron-phonon and spin-orbit coupling. The Dresselhaus spin-orbit coupling [78] is the dominant

[16] Not only the orbital states of the electron inside the DQD are obtained from an approximation as harmonic oscillator, but also the Landau levels.

process for spin-flip transitions between the Zeemann sublevels in the DQD [79, 80]. Equilibration is expected to be achieved after a time $\Gamma_{12} + \Gamma_{21}$ (see, e.g. [81]), where the Γ-terms denote the rate for a spin-flip with emission and absorption of a piezophonon, respectively. An upper bound for the equilibration time is given by the rate for spontaneous emission of a piezophonon. A rough estimation of this rate for the present set-up is given by Eq (8) of Ref [80], but with an additional factor $\exp\left\{-2d(g\mu_B B)/(\hbar c)\right\}$, where d denotes the distance between the two substrates, taking into account the exponential decay of the piezoelectric field accompanying the piezophonons [43, 71], and the energy conservation, $\hbar c k = g\mu_B B$. For a magnetic field $B = 1$ T, the equilibration rate is of the order of 1 s^{-1}. The steady state of the electron spin could be achieved while the electrons are stored in a storage ring as it is shown in Fig. 12.1. Efficient electron transport over macroscopic distances has been shown in [64][17]: The lengths l, L of the storage ring can be chosen arbitrarily in the sub-mm regime. Future conveyor belts for electrons using serpentine-shaped SAW waveguides [82, 83] could provide an alternate route to reach thermalization. In comparison, however, the present set-up details make the proposed storage ring more feasible.

3.2.5 Comparison of thermalization rates

From the considerations above it follows that the thermalization time of the electron spin states with the thermal Hawking phonons is independent of the SAW potential amplitude U_0, i.e. the SAW power. Similarly, the dependence of the thermalization time for the electron orbital states inside the DQD on U_0 can be estimated using Fermi's golden rule: The electron-phonon interaction is the relevant process [84, 85, 86, 87, 88, 89] for transitions between harmonic oscillator states $|m\rangle$ and $|n\rangle$ of the electrons in the DQDs, giving rise to rates

$$\Gamma_{mn} \propto \left|\langle m \left| e^{i\,\mathbf{q}\cdot\mathbf{r}} \right| n\rangle\right|^2 \rho\,(\hbar\omega)\,,$$

where $\rho(E) \propto E$ denotes the density of states for a two-dimensional phonon system and the exponential comes from the electron-phonon. When restricting the electron motion and phonon momentum to one dimension for simplicity, and employing the well-known relation

$$x = \sqrt{\frac{\hbar}{2m\omega}}\left(a + a^\dagger\right)$$

between position operator and the creation and annihilation operator for the harmonic oscillator case, the above matrix element can be expressed via the displacement operator $\mathcal{D}(\alpha) = \exp\left\{\alpha a^\dagger - \alpha^* a\right\}$ as

$$\langle m \left| e^{i\,\mathbf{q}\cdot\mathbf{r}} \right| n\rangle = \langle m \left| \mathcal{D}(\alpha) \right| n\rangle$$

with

$$\alpha = i\ |n-m| \sqrt{\frac{\hbar\omega}{2mc^2}},$$

where the phonon momentum was determined via energy conservation: Transitions between the oscillator states $|m\rangle$ and $|n\rangle$ with energy difference $|n-m|\,\hbar\omega$ involve phonons with energy $\hbar c q$. The matrix representation of the displacement operator in the Fock basis was given

[17] Assuming an exponential decay of the number of charge carriers along the propagation direction, $n_c(x) \sim \exp\{-x/\Lambda\}$, the decay constant Λ can be estimated to several thousand SAW wavelengths for Ref. [64]. Further increase could be achieved by increasing the SAW power.

by Cahill and Glauber [76] and reads

$$\langle m\,|\mathcal{D}(\alpha)|\,n\rangle = \sqrt{\frac{m!}{n!}}\alpha^{n-m}\mathrm{e}^{-|\alpha|^2/2}L_m^{(n-m)}\left(|\alpha|^2\right)$$

for $n \geq m$[18], where $L_m^{(n-m)}$ are associated Laguerre polynomials. As result, the thermalization time almost grows exponentially with $\omega \propto \sqrt{U_0}$.

The lifetime t_l, i.e. the time an electron stays trapped in the DQD potential, must be sufficiently large for the electrons to equilibrate with the Hawking phonons. Electron tunneling out of the DQD potential scales with the SAW potential amplitude as $\exp\left\{-\sqrt{U_0/(\hbar\omega_A)}\right\}$ [90], where the attempt frequency ω_A is related to the potential curvature, which in the harmonic approximation is proportional to the SAW potential as well, $\omega_A \propto U_0$. Hence, electron tunneling is expected to be not controllable via the SAW potential amplitude. While the radiative recombination lifetime of the electrons and holes is essentially infinite [64] due to their spatial separation, experimental data indicates a non-monotonic behavior of the lifetime as a function of the SAW potential amplitude [91].

To contrast that, it is noted again that for the electron spin as thermometer, the thermalization time and the lifetime t_l can be chosen independently from each other.

[18] For the case $n < m$ the expression for the displacement operator in the Fock basis can be simply complex conjugated.

4 Quantum simulation of particle creation in curved spacetime

4.1 Criticism

As was pointed out by the reviewers and initially escaped our attention, the derivation of the Hawking temperature resulting in Eq. (2.7) with the surface gravity κ_g assumes a stationary spacetime. However, as is evident from Eq. (2.5),

$$\mathrm{d}s^2 = -\left[c^2(x - vt) - v^2\right]\mathrm{d}t^2 + 2v\mathrm{d}t\mathrm{d}x + \mathrm{d}x^2,$$

the effective metric in the moving reference frame is explicitly time dependent. Hence, the conclusion drawn from the (apparent) analogy to the effective metrics in Refs. [14, 15], which led to the expression for the surface gravity Eq. (2.6),

$$\kappa_g = \left|\frac{\partial c}{\partial x}\right|_{c^2=v^2},$$

is not evident and requires validation for explicitly time dependent metrics. Furthermore, not only the thermal nature of spontaneously created particles is unclear, but their existence in the first place was challenged by the reviewers. This concern was expressed by one of the reviewers by proposing an experiment on a different platform which is (almost) analogue to our proposal. The propagation of free surfaces waves in a water channel with an obstacle on the bottom and a static water level was considered. The wave speed will change with the water depth according to $c(x) = \sqrt{gh(x)}$ in the long wavelength approximation. As moving detector, a camera moving at constant speed in the lab frame with look at the free surface deformation is used. The reviewer expressed doubts about the existence of Hawking radiation in this set-up.

Indeed, mode mixing of positive and negative frequency modes when scattered at the horizon, is at the heart of the Hawking effect and a viable way to access the associated Hawking temperature [17, 92]. Classical and quantum field theory are the natural languages to give answers to this question and, in the present set-up, to particle creation.

However, we stress that sending a wave corresponding to either a positive or a negative frequency mode with respect to the lab system along the substrate is not necessarily appropriate for the mode mixing experiment because the relation between positive and negative frequency modes with respect to the lab system and those with respect to the moving reference frame is not obvious at all and must be investigated using quantum field theory. As we pointed out, the acoustic horizon is present only in the moving reference frame.

Regarding particle creation, we note that the substrate layer with inhomogeneous SAW speed is not driven with SAWs on purpose—there is no appeal for the propagation of a classical field on the effective background metric. As particle creation is based on the canonical commutation relations of the underlying quantum field, this process is of a purely quantum mechanical nature. The energy which is associated with the created phonons is delivered by the external drive which keeps the detector moving at constant speed. Similar to the Unruh effect, the interaction between the detector and the quantum field is essential for particle creation. This is not given in the classical experiment proposed by the reviewer, which is the missing ingredient to be entirely analogue to our proposal.

4.2 Reinterpretation

While the expression for the surface gravity Eq. (2.6) might be incorrect, the line element

$$\mathrm{d}s^2 = -\left[c^2(x - vt) - v^2\right]\mathrm{d}t^2 + 2v\mathrm{d}t\mathrm{d}x + \mathrm{d}x^2,$$

which follows from the effective metric in the moving reference frame, does have features in common with Painlevé-Gullstrand's line element

$$\mathrm{d}s^2 = -\left[c^2 - v^2(r)\right]\mathrm{d}t^2 + 2v(r)\mathrm{d}r\mathrm{d}t + \mathrm{d}r^2 + r^2\mathrm{d}\Omega^2,$$

and the Friedmann-Lemaître-Robertson-Walker line element

$$\mathrm{d}s^2 = -c^2\mathrm{d}t^2 + a^2(t)\mathrm{d}\mathbf{r}^2$$

of an expanding universe with scale factor $a(t)$, revealing its potential for particle creation. This is supported by calculations using the Bloch-Redfield equations in Sec. 6. There, we argue that the electrons in the DQD equilibrate to a non-thermal state when in contact with a zero-temperature phonon bath. This is attributed to particle creation in form of piezoelectric phonons. However, note that the present set-up does not strictly simulate either of both systems, as Eq. 2.5 does not match their respective metric precisely.

5 Bloch-Redfield equation: derivation

In this section the Bloch-Redfield equation is introduced in order to use them in the following section as a perturbative approach towards a justification for particle creation, similar to Unruh's perturbative treatment of the Unruh effect. The derivation follows the one given in U. Weiss' book "Quantum dissipative systems" [93] and "Superconducting qubits II: Decoherence" by Wilhelm et. al [94], which are recommended for further details.

Consider a quantum system of interest with arbitrary finite dimensional Hilbert space, which is in contact with a reservoir. The Bloch-Redfield equation is a useful tool to study those open quantum systems, especially in regard to relaxation and decoherence of qubits induced by the interaction with the reservoir [94]. Other areas of physics, where the use of the Bloch-Redfield equation is well established, are in NMR [95, 96] and optical spectroscopy [97].

As starting point, the Liouville-von Neumann equation for the density matrix ρ_{full} of the full system is considered,

$$\dot{\rho}_{\text{full}} = -\frac{i}{\hbar}\left[H, \rho_{\text{full}}\right] =: \mathcal{L}\rho_{\text{full}}. \tag{5.1}$$

Here, the Hamiltonian

$$H = H_S + H_R + H_I$$

describes the full system composed of the relevant quantum system, the reservoir and their mutual interaction. Accordingly, the Liouville superoperator consists of three terms as well,

$$\mathcal{L} = \mathcal{L}_S + \mathcal{L}_R + \mathcal{L}_I.$$

The dynamics of the relevant system, described by the density matrix ρ_S, can be obtained by applying an appropriate projection operator P on the full density matrix,

$$\rho_S(t) = P\rho_{\text{full}}(t) := \text{Tr}_R\left\{\rho(t)\right\}. \tag{5.2}$$

Here, $\text{Tr}_R\{\bullet\}$ denotes the partial trace over the reservoir. Employing the projection operator, the full density matrix can be decomposed in a relevant and irrelevant part as

$$\rho_{\text{full}} = \underbrace{P\rho_{\text{full}}}_{=\rho_S} + (1-P)\rho_{\text{full}}. \tag{5.3}$$

Using this decomposition, one can derive a set of coupled equations for the two parts,

$$(1-P)\dot{\rho}_{\text{full}} = (1-P)\mathcal{L}\rho_S + (1-P)\mathcal{L}(1-P)\rho_{\text{full}} \tag{5.4a}$$

$$\dot{\rho}_S = P\mathcal{L}\rho_S + P\mathcal{L}(1-P)\rho_{\text{full}}, \tag{5.4b}$$

by applying $1-P$ to yield Eq. (5.4a) and P to yield Eq. (5.4b) on the Liouville-von Neumann equation (5.1). In order to obtain an equation solely describing the relevant dynamics, the two equations are decoupled by plugging the formal solution of Eq. (5.4a),

$$(1-P)\rho_{\text{full}}(t) = \mathrm{e}^{(1-P)\mathcal{L}t}(1-P)\rho_{\text{full}}(0) + \int_0^t \mathrm{e}^{(1-P)\mathcal{L}\tau}(1-P)\mathcal{L}\rho_S(t-\tau)\mathrm{d}\tau,$$

into Eq. (5.4b), which yields the exact Nakajima-Zwanzig equation [98, 99],

$$\dot{\rho}_S(t) = P\mathcal{L}\rho_S(t) + \int_0^t P\mathcal{L}\mathrm{e}^{(1-P)\mathcal{L}\tau}(1-P)\mathcal{L}\rho_S(t-\tau)\mathrm{d}\tau + P\mathcal{L}\mathrm{e}^{(1-P)\mathcal{L}t}(1-P)\rho_{\mathrm{full}}(0). \tag{5.5}$$

The inhomogeneity depending on the initial value $\rho_{\mathrm{full}}(0)$ can be dropped when assuming factorizing initial conditions, i.e. $\rho_{\mathrm{full}} = \rho_S \otimes (1-P)\rho_{\mathrm{full}}$ (see also Ref. [94] for a discussion of this assumption). Since P commutes with $\mathcal{L}_S$ and further $\mathcal{L}_R\rho_S = 0$, one finds

$$\dot{\rho}_S(t) = P(\mathcal{L}_S + \mathcal{L}_I)\rho_S(t) + \int_0^t P\mathcal{L}_I\mathrm{e}^{(1-P)\mathcal{L}\tau}(1-P)\mathcal{L}_I\rho_S(t-\tau)\mathrm{d}\tau. \tag{5.6}$$

The dynamics of the relevant system consists of a reversible motion, described by the first instantaneous term, and an irreversible motion stemming from the time-retarded second term.

For weak system-bath interactions the Born approximation, which is second order in $\mathcal{L}_I$, can be applied. This allows to drop $\mathcal{L}_I$ in the exponent as the integrand is already of second order in $\mathcal{L}_I$. Disregarding memory effects, which is accomplished by the Markov approximation valid if the system-bath interaction is the slowest process in the full system, one finally arrives at the Bloch-Redfield equation

$$\dot{\rho}_S(t) = P(\mathcal{L}_S + \mathcal{L}_I)\rho_S(t) + \int_0^\infty P\mathcal{L}_I\mathrm{e}^{(1-P)(\mathcal{L}_S+\mathcal{L}_R)\tau}(1-P)\mathcal{L}_I\mathrm{d}\tau\rho_S(t). \tag{5.7}$$

In the eigenbasis of H_S, this reads [93]

$$\dot{\rho}_{\mu\nu}(t) = -i\,\omega_{\mu\nu}\rho_{\mu\nu}(t) + \sum_{\kappa\lambda} R_{\mu\nu\kappa\lambda}\rho_{\kappa\lambda}(t). \tag{5.8}$$

Here, $R_{\mu\nu\kappa\lambda}$ are the elements of the Redfield tensor and the $\rho_{\mu\nu}$ are the elements of the density matrix of the relevant system. For eigenstates $|\mu\rangle$ and $|\nu\rangle$ of H_S with eigenenergies E_μ and E_ν, respectively, $\omega_{\mu\nu}$ is defined as $\omega_{\mu\nu} = (E_\mu - E_\nu)/\hbar$. The Redfield tensor has the form [93, 100]

$$R_{\mu\nu\kappa\lambda} = \Gamma^+_{\lambda\nu\mu\kappa} + \Gamma^-_{\lambda\nu\mu\kappa} - \delta_{\nu\lambda}\sum_\alpha \Gamma^+_{\mu\alpha\alpha\kappa} - \delta_{\mu\kappa}\sum_\alpha \Gamma^-_{\lambda\alpha\alpha\nu} \tag{5.9}$$

with the rates given by [93, 100]

$$\Gamma^+_{\lambda\nu\mu\kappa} = \hbar^{-2}\int_0^\infty \mathrm{d}t\langle\langle\lambda|\, H_{I,\mathrm{SB}}(t)\,|\nu\rangle\,\langle\mu|\, H_{I,\mathrm{SB}}(0)\,|\kappa\rangle\rangle_{\mathrm{bath}}\mathrm{e}^{-i\,\omega_{\mu\kappa}t} \tag{5.10}$$

$$\Gamma^-_{\lambda\nu\mu\kappa} = \hbar^{-2}\int_0^\infty \mathrm{d}t\langle\langle\lambda|\, H_{I,\mathrm{SB}}(0)\,|\nu\rangle\,\langle\mu|\, H_{I,\mathrm{SB}}(t)\,|\kappa\rangle\rangle_{\mathrm{bath}}\mathrm{e}^{-i\,\omega_{\lambda\nu}t}, \tag{5.11}$$

where $\langle\cdot\rangle_{\mathrm{bath}}$ is the expectation value of the bath observable and $H_{I,\mathrm{SB}}$ is the interaction Hamiltonian in the interaction picture with respect to the bath Hamiltonian.

6 Bloch-Redfield equation: application

For a motion of the DQD in x direction, $\mathbf{v} = v\hat{e}_x$, the Hamiltonian approximately describing the electron-spin while interacting with the piezoelectric phonons can be written as $H = H_S + H_{\mathrm{SB}} + H_B$ with the spin Hamiltonian [84, 85, 86, 87, 88, 89]

$$H_S = E_0\sigma_z + \Delta E\sigma_y, \tag{6.1}$$

the phonon bath Hamiltonian

$$H_B = \sum_q \hbar\omega_q \left(b_q^\dagger b_q + \frac{1}{2}\right) \tag{6.2}$$

and their mutual interaction Hamiltonian

$$H_{\mathrm{SB}} = \sigma_x \sum_q M_q \mathrm{e}^{i\,qvt}\left(b_{-q}^\dagger + b_q\right). \tag{6.3}$$

Here, ΔE originates from a motion induced constant magnetic field, and the spin-phonon coupling is due to a motion induced magnetic noise originating from the electric noise due to the piezophonons [84, 85]. Details about the parameters and their dependence on the DQD speed and the material constants can be found in Ref [84] and references therein. Using this model Hamiltonian, the dynamics of the DQD spin while interacting with the phonon system can be calculated using the Bloch-Redfield equation derived above, applied to the density matrix of the DQD. The eigenstates of H_S are denotes by $|0\rangle$ and $|1\rangle$ for the ground and excited state, respectively. The interaction Hamiltonian in the interaction picture with respect to the bath Hamiltonian is given by

$$\begin{aligned} H_{I,\mathrm{SB}}(t) =&\ \exp\left\{i\,H_B t/\hbar\right\} H_{\mathrm{SB}} \exp\left\{-i\,H_B t/\hbar\right\} && (6.4)\\ =&\ \sigma_x \sum_q M_q \mathrm{e}^{i\,qvt}\left(b_{-q}^\dagger \mathrm{e}^{i\,\omega_q t} + b_q \mathrm{e}^{-i\,\omega_q t}\right). && (6.5)\end{aligned}$$

Using $\langle b_{-q}^\dagger b_l\rangle = \delta_{-q,l} n\left(\omega_q\right)$ with the Bose-Einstein distribution $n(\omega)$ the rates can be expressed as

$$\Gamma^+_{\lambda\nu\mu\kappa} = M_{\lambda\nu\mu\kappa} \sum_q \left|M_q\right|^2 \int_0^\infty \mathrm{d}t \left\{\mathrm{e}^{i\,[qv+\omega_q-\omega_{\mu\kappa}]t} n(\omega_q) + \mathrm{e}^{i\,[qv-\omega_q-\omega_{\mu\kappa}]t}(n(\omega_q)+1)\right\} \tag{6.6}$$

$$\Gamma^-_{\lambda\nu\mu\kappa} = M_{\lambda\nu\mu\kappa} \sum_q \left|M_q\right|^2 \int_0^\infty \mathrm{d}t \left\{\mathrm{e}^{i\,[qv-\omega_q-\omega_{\lambda\nu}]t} n(\omega_q) + \mathrm{e}^{i\,[qv+\omega_q-\omega_{\lambda\nu}]t}(n(\omega_q)+1)\right\}, \tag{6.7}$$

where $M_{\lambda\nu\mu\kappa} = \hbar^{-2} \langle\lambda|\sigma_x|\nu\rangle \langle\mu|\sigma_x|\kappa\rangle$.
For a subsonic motion, $v < c$, these rates are given by

$$\Gamma^{+}_{\lambda\nu\mu\kappa} = \frac{\pi}{2} M_{\lambda\nu\mu\kappa} \begin{cases} \frac{J\left(\omega^{-}_{\kappa\mu}\right)}{1-v/c}\left[n\left(\omega^{-}_{\kappa\mu}\right)+1\right] + \frac{J\left(\omega^{+}_{\kappa\mu}\right)}{1+v/c}\left[n\left(\omega^{+}_{\kappa\mu}\right)+1\right] & ,\omega_{\kappa\mu} > 0 \\ \frac{J\left(\omega^{+}_{\mu\kappa}\right)}{1+v/c} n\left(\omega^{+}_{\mu\kappa}\right) + \frac{J\left(\omega^{-}_{\mu\kappa}\right)}{1-v/c} n\left(\omega^{-}_{\mu\kappa}\right) & ,\omega_{\mu\kappa} > 0 \end{cases} \tag{6.8a}$$

$$\Gamma^{-}_{\lambda\nu\mu\kappa} = \frac{\pi}{2} M_{\lambda\nu\mu\kappa} \begin{cases} \frac{J\left(\omega^{-}_{\lambda\nu}\right)}{1-v/c}\left[n\left(\omega^{-}_{\lambda\nu}\right)+1\right] + \frac{J\left(\omega^{+}_{\lambda\nu}\right)}{1+v/c}\left[n\left(\omega^{+}_{\lambda\nu}\right)+1\right] & ,\omega_{\lambda\nu} > 0 \\ \frac{J\left(\omega^{+}_{\nu\lambda}\right)}{1+v/c} n\left(\omega^{+}_{\nu\lambda}\right) + \frac{J\left(\omega^{-}_{\nu\lambda}\right)}{1-v/c} n\left(\omega^{-}_{\nu\lambda}\right) & ,\omega_{\nu\lambda} > 0 \end{cases}, \tag{6.8b}$$

with $\omega^{\pm}_{\alpha\beta} = \omega_{\alpha\beta}/(1 \pm v/c)$ and where $J(\omega) = \sum_q \left|M_q\right|^2 \delta(\omega - \omega_q)$ denotes the spectral density and it was used that $\int_0^\infty \mathrm{e}^{i\,\omega t}\mathrm{d}t = \pi\delta(\omega)$, where the imaginary parts resulting from principal value integrals are neglected as they manifest themselves as Lamb shifts.

For a supersonic motion, $v > c$, and a vanishing temperature of the phonon bath, the rates are given by

$$\Gamma^{+}_{\lambda\nu\mu\kappa} = \frac{\pi}{2} M_{\lambda\nu\mu\kappa} \begin{cases} \frac{J\left(\omega^{+}_{\kappa\mu}\right)}{v/c+1} & ,\omega_{\kappa\mu} > 0 \\ \frac{J\left(\omega^{-}_{\mu\kappa}\right)}{v/c-1} & ,\omega_{\mu\kappa} > 0 \end{cases} \tag{6.9a}$$

$$\Gamma^{-}_{\lambda\nu\mu\kappa} = \frac{\pi}{2} M_{\lambda\nu\mu\kappa} \begin{cases} \frac{J\left(\omega^{+}_{\lambda\nu}\right)}{v/c+1} & ,\omega_{\lambda\nu} > 0 \\ \frac{J\left(\omega^{-}_{\nu\lambda}\right)}{v/c-1} & ,\omega_{\nu\lambda} > 0 \end{cases}. \tag{6.9b}$$

From Eqs 6.8a and 6.8b and Eqs 6.9a and 6.9b, respectively, the Redfield tensor Eq 5.9 can be computed for each corresponding case.

For the steady state solution of the Bloch-Redfield Eqs 5.8 one finds vanishing off-diagonal matrix elements, $\rho_{10} = \rho_{01} = 0$, in both sub- and supersonic cases, as expected due to spin decoherence. The diagonal matrix elements can be expressed as

$$\frac{\rho_{11}}{\rho_{00}} = \frac{\Gamma_{12}}{\Gamma_{21}} \tag{6.10}$$

with the absorption rate $\Gamma_{12} = R_{1111} = \Gamma^{+}_{1221} + \Gamma^{-}_{1221}$ and the emission rate $\Gamma_{21} = R_{1122} = \Gamma^{+}_{2112} + \Gamma^{-}_{2112}$.

For subsonic motion, $v < c$, these rates explicitly read

$$\Gamma_{12} = \frac{\pi}{2} M_{1221} \left\{ \frac{J\left(\omega^{+}_{21}\right)}{1+v/c} n\left(\omega^{+}_{21}\right) + \frac{J\left(\omega^{-}_{21}\right)}{1-v/c} n\left(\omega^{-}_{21}\right) \right\} \tag{6.11}$$

$$\Gamma_{21} = \frac{\pi}{2} M_{1221} \left\{ \frac{J\left(\omega^{+}_{21}\right)}{1+v/c}\left[n\left(\omega^{+}_{21}\right)+1\right] + \frac{J\left(\omega^{-}_{21}\right)}{1-v/c}\left[n\left(\omega^{-}_{21}\right)+1\right] \right\}. \tag{6.12}$$

The steady state Eq 6.10 is clearly non-thermal in the sense that the effective temperature T' of the DQD, given via

$$\frac{\rho_{11}}{\rho_{00}} = \exp\left\{-\frac{\hbar\omega_{10}}{k_B T'}\right\}, \tag{6.13}$$

does not in general coincide with the temperature of the phonon bath the DQD is in contact with, $T \neq T'$. In this scenario the rates and thus the non-thermality can be easily explained via the Doppler-effect: Phonons participating in transitions in the DQD have a frequency in the rage $\Omega = [\omega_{10} - \Delta\omega/2, \omega_{10} + \Delta\omega/2]$ with the line width $\Delta\omega$. As these frequencies are measured in the reference frame of the DQD, and the speed of sound c and the speed of the DQD add up/subtract leading to a Doppler-shift $\omega \to (1 \pm v/c)\omega$, there are in fact two frequency ranges involved in transitions, namely $\Omega/(1 \pm v/c)$ measured in the bath frame. Each of them contribute to the absorption and emission rate in the usual manner, where the prefactors $(1 \pm v/c)^{-1}$ are due to the Doppler-shifted line width. Furthermore, for a zero temperature phonon bath the absorption rate also vanishes, $\Gamma_{12} = 0$, since there are no phonons present which could excite the DQD and thus the DQD equilibrates with the phonon bath by relaxing to its ground state and thus having vanishing effective temperature.

In the case of supersonic motion, $v > c$, where we restricted the analyses to a vanishing bath temperature $T = 0$, the absorption and emission rates are now given by

$$\Gamma_{12} = \pi \frac{\boldsymbol{M}_{1221}}{v/c - 1} \boldsymbol{J}\left(\omega_{21}^{-}\right) \tag{6.14}$$

$$\Gamma_{21} = \pi \frac{\boldsymbol{M}_{1221}}{v/c + 1} \boldsymbol{J}\left(\omega_{21}^{+}\right). \tag{6.15}$$

Even though the bath is at zero temperature, the effective temperature of the DQD given via Eq 6.13 is non-vanishing, because the absorption rate does not vanish. We argue that this motion-enhanced character of the density matrix can be attributed to the presence of excess particles in form of piezophonons originating from particle creation, which excite the DQD and lead it to a steady state which is not in thermal equilibrium with the bath.

7 Conclusion

We have presented a new semiconductor analogue system to simulate quantum effects in general relativity. Particle creation in this system is expected for a DQD moving with constant speed in the measurement substrate. The detailed steps to achieve this are discussed, including the charge density modulation of a two-dimensional electron gas which is responsible for the change in speed of sound for SAWs travelling on the substrate. This in turn leads to an acoustic horizon for SAWs seen by the DQD.

We analyzed a measurement scheme to detect the created particles using the DQDs, whose steady-state spin populations differ from that of a thermal state due to their interaction with the created piezophonons. We stress that a number of different alternatives to observe the evanescent waves could be pursued, as their detection is well developed in fields such as biosensing [101]. However, these schemes must be adapted to allow for the characterization of the quantum nature of the associated SAW phonons.

Appendices

7.A Energy spectrum inside a DQD with perpendicular magnetic field

The Hamiltonian describing an electron trapped inside a DQD with an external, perpendicular magnetic field, reads

$$H = \frac{1}{2m}(\mathbf{p} + e\mathbf{A})^2 + \frac{1}{2}m\omega^2\mathbf{r}^2, \tag{7.1}$$

where the motion is assumed to be restricted to the xy-plane and the electric potential due to the piezoelectric effect is approximated by a symmetric harmonic oscillator with

$$\omega = \frac{2\pi}{\lambda}\sqrt{\frac{U_0}{m}},$$

according to the treatment leading to Eqs. (3.3). Note that a canonical transformation from the lab frame to the moving frame, in which the DQD is at rest, was performed. When doing so, the magnetic field $\mathbf{B} = B_0\hat{e}_z$ must be transformed into the moving frame as well, giving rise to an electric field $\mathbf{E} = vB_0/2\,\hat{e}_y$, while the magnetic field along the z-axis stays almost unchanged. Here, it was used that the velocity $v \sim 10^3\ \mathrm{m\,s^{-1}}$ of the DQD is much smaller than the speed of light.[19] The constant force on the electron due to the electric field leads to a displacement Δy in y-direction of

$$\frac{\Delta y}{\lambda} = \frac{e\lambda v B_0}{8\pi^2 U_0},$$

which is with the typical parameters $v \sim 10^3\ \mathrm{m\,s^{-1}}$, $\lambda \sim 10^{-6}\ \mathrm{m}$, $U_0 \sim 40 - 600\ \mathrm{meV}$ of the order of $10^{-4} - 10^{-3}$ in units of the SAW wavelength λ, and hence negligible.

In the symmetric gauge,

$$\mathbf{A} = \frac{B_0}{2}\begin{pmatrix} -y \\ x \\ 0 \end{pmatrix},$$

the Hamiltonian Eq. (7.1) can be written as

$$H = \frac{\mathbf{p}^2}{2m} + \frac{1}{2}m\tilde{\omega}_B^2\mathbf{r}^2 + \omega_B L_z$$

with $L_z = xp_y - yp_x$ the z-component of the angular momentum, $\omega_B = eB_0/m$ the cyclotron frequency and

$$\tilde{\omega}_B = \sqrt{\omega^2 + \left(\frac{\omega_B}{2}\right)^2}.$$

As central force field, the harmonic oscillator described by the first part conserves the angular momentum, and hence commutes with the second part containing L_z. Therefore, the spectrum of H is just the Minkowski sum of the spectra of the individual parts. Both, the harmonic oscillator and the second part, have equidistant energy spectra with splitting $\hbar\tilde{\omega}_B$ and $\hbar\omega_B$, respectively.

[19] The analogous transformation of the electric potential due to the DQD can be disregarded for the same reason.

Finally, the electron spin leads to the usual Zeemann splitting of the energy levels with separation $\Delta = g\mu_B B_0$. As mentioned above, this splitting usually differs from $\hbar\omega_B$, and is much smaller for GaAs for instance.

Part II

Role of the proximity effect for normal-metal quasiparticle traps

The performance of many superconducting devices is degraded in presence of non-equilibrium quasiparticles in the superconducting part. One promising approach towards their evacuation is the use of normal-metal quasiparticle traps, where normal metal is brought into good metallic contact with the superconductor. A voltage biased normal-metal–insulator–superconductor junction equipped with such a trap is used to investigate on the trapping performance and the part played by the superconducting proximity effect therein. This involves an appropriate one-dimensional model of the junction and the numerical solution of Usadel equations describing the non-equilibrium state of the superconductor. The functionality of the trap is determined by the density of states (DOS) at the tunnel barrier. Herein, the proximity effect leads to two antagonistic characteristics affecting the trapping performance: the beneficial reduction of the DOS at an energy $|E| = \Delta_{\mathrm{BCS}}$ versus the contraction of the spectral energy gap in the DOS causing quasiparticle poisoning. For both effects the trap position is decisive, which needs to be taken into account for optimizing the trapping performance. In addition, the conversion between dissipative normal and supercurrent inside the superconducting part with its impact on the quasiparticle density is studied.

8 Introduction

8.1 Quasiparticle traps for superconducting devices

8.1.1 Why to trap quasiparticles: quasiparticles and superconducting devices

Mesoscopic superconductors are easily driven out of equilibrium, often leading to the generation of quasiparticles (QPs). Furthermore, there is convincing experimental evidence for the existence of a residual QP population even at low temperatures [102, 103, 104, 105, 106], exceeding the expected equilibrium density. Due to the spectral energy gap in the superconducting DOS the number of QPs at thermal equilibrium should be exponentially suppressed at temperatures far below this gap, vividly illustrated by [107]: A peace of superconducting aluminum in thermal equilibrium at 20 mK, a temperature rather easily realized with todays refrigerating techniques, is expected to have a QP density of one pair per the volume of the earth. The non-equilibrium QPs have a detrimental impact on most superconducting devices, e.g. causing decoherence in superconducting qubit systems [106, 108, 109, 110, 111, 112, 113, 114], lowering the efficiency of micro-refrigerators [115, 116, 117, 118], or preventing the experimental detection of the 2e periodic Coulomb staircase in single Cooper pair transistors [119, 120, 121, 122].

Sufficient cooling down to temperatures far below the critical temperature might help for some technical applications since thermal QPs are (almost) absent due to the energy gap in the excitation spectrum. One important process during QP relaxation is their electron-phonon mediated recombination [123] to form Cooper pairs, along with the emission of phonons with energy $\hbar\omega \gtrsim 2\Delta$. The related time scale is controlled not only by the phononic density of states at $\hbar\omega \gtrsim 2\Delta$, but also by the phonon's potential to break again a Cooper pair and hence to excite new QPs, effectively increasing the QP lifetime [123, 124, 125, 126, 127, 128]. Thus, reaching complete thermalization might take too long to be practical for most quantum computing applications based on superconducting elements. Furthermore, the generation of non-equilibrium QPs is intrinsic to qubit control techniques using single flux quantum pulse sequences [129, 130, 131], while different strategies to minimize QP generation and poisoning are available [131].

In the following, the performance of superconducting qubits, micro-refrigerators based on normal-metal–insulator–superconductor junctions and single Cooper pair transistors in the presence of QPs is qualitatively explained.

Superconducting qubits

The currently most promising candidates for qubits based on artificial atoms are the superconducting qubits. Their success is ultimately based on the facts that the superconducting state is a robust macroscopic quantum phenomenon and allows for lossless transmission of signals. The Josephson effect [132] takes a key role in regards to quantum computing since the use of Josephson junctions adds anharmonicity and hence renders possible the application of superconducting circuits as two-level systems in the first place.

However, the tunneling of quasiparticles through the Josephson junction leads to relaxation and decoherence of the superconducting qubit [106, 108, 109, 110, 111, 112, 113, 114]. For most of the current qubit designs the associated rates $1/T_1$ and $1/T_2$ are small compared to those determined by external factors [109]. However, the upper limit of the coherence time

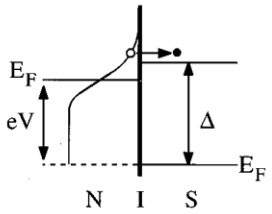

FIGURE 8.1: A normal metal is cooled due to an energy-selective extraction of "hot" electrons with an energy exceeding the superconducting energy gap. The figure is taken from [133].

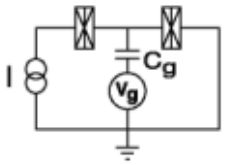

FIGURE 8.2: Circuit representation of a single Cooper pair transistor. The figure is taken from [121].

due to quasiparticle related decoherence is of the order of the coherence time required for fault-tolerant quantum computing [103].

Micro-refrigerators

In a normal-metal–insulator-superconductor junction electrons on the normal-metal side can enter the superconductor as quasiparticles only if their energy exceeds the superconducting energy gap. This energy-selective extraction of "hot" electrons results in a cooling of the normal metal.

The expected cooling performance of such NIS junctions or related set-ups is diminished by quasiparticles, which can tunnel back into the normal metal or recombine with each other under emission of phonons with energy $\hbar\omega \approx 2\Delta$ which can be absorbed in the normal metal, both resulting in the back transfer of the just extracted energy [115, 116, 117, 118].

Single Cooper pair transistors

The operation of the single Cooper pair transistor (shown in Fig. 8.2) relies on the coherent tunneling of Cooper pairs on and off the superconducting island. In the regime, where the charging energy $E_C = e^2/(2C_\Sigma)$ with the total island capacitance C_Σ exceeds the Josephson energy E_J, the variation of E_J with the normalized gate polarization $n_g = C_g V_g/e$ due to phase-charge duality [119] is strongest. This is predicted to lead to a particular behavior of the switching current I_c from the supercurrent branch near zero voltage to the voltage state [134]: I_c is predicted to be $2e$ periodic in n_g with a maximum where charge states differing by one Cooper pair are degenerate.

The experimental verification is impeded by quasiparticle poisoning, i.e. presence of non-equilibrium quasiparticles [121] incoherently tunneling onto the island, thereby changing its charge (parity) and resulting in switching currents with a $1e$ periodic or even more complicated structure [135] as a function of n_g.

8.1.2 How to trap quasiparticles: Normal-metal traps and co.

Evacuating and trapping QPs in less active regions of the device seems to provide a practicable way to improve the device performance. Most of the current trapping techniques share a common qualitative principle: Since the QP energy depends on the spectral energy gap via

$$E = \sqrt{\xi^2 + \Delta^2}$$

with the kinetic energy ξ measured from the Fermi energy, spatial variations in the superconducting order parameter deform the energy landscape the QPs reside in, thereby introducing accumulation regions for the QPs in the local minima. Once they relaxed in regions with lower Δ the QPs are effectively trapped there, provided that the thermal energy is not sufficient to promote them back to regions with higher Δ.

These spatial variations can be achieved by engineering gap inhomogeneities [121, 136, 137] directly affecting the order parameter, or by exploiting the superconducting proximity effect of a normal metal on a superconductor, which occurs in normal-metal vortex penetration due to external magnetic fields [107, 138, 139, 140, 141] or when purposely bringing both metals in good metallic contact [115, 142, 143, 144, 145, 146, 147].[1]

The choice of which trapping technique to use depends on the superconducting device: While gap engineering was for example successfully used for a single Cooper pair transistor [121], there allowing for sufficient control of the quasiparticle distribution, its application to a transmon qubit proved ineffective [148]. Micro-refrigerators are effectively combined with vortex traps [139], whereas vortrex flow can lead to dissipation and degradation of the quality factor of superconducting resonators and qubits [107, 149, 150]. The effective use of normal-metal traps was for example demonstrated for micro-refrigerators [115], and a careful trap design and positioning can reduce the quasiparticle-induced relaxation rate of transmon qubits [151] and even compensate for relaxation which is induced by subgap states resulting from the proximity to the normal-metal trap [152].

8.2 Normal-metal quasiparticle traps in the focus

This work focuses on the QP trapping performance of the latter technique, a normal metal in good metallic contact with a superconductor. As is shown in Fig. 8.3, a superconducting island of length $L_S = L_1 + L_2$ is connected via a tunnel junction to a normal metal reservoir hold at temperature $T = 0$ and potential eV measured from the superconductor's one. QPs are injected into, diffuse through and exit the superconductor via the electrical grounding at the superconductor's end. A thin normal metal partially covering the superconducting island in good metallic contact in a distance of L_1 to the injector serves as QP trap.

The role of the proximity effect on the non-equilibrium steady-state of the superconducting island is studied, especially in regard to the density of QPs. In order to determine the efficiency of the trap and its influence on the QP distribution $n_{\mathrm{qp}}(x)$ inside the S-island, $n_{\mathrm{qp}}(x)$ has to be compared with that of an NIS-junction with the same geometry but without a covering metal. In the following, this reference set-up is referred to as setup 1, whereas the set-up with normal-metal trap shown in Fig. 12.1 is referred to as setup 2.

Usually, the dynamics and the steady-state of the QP distribution are studied by using a phenomenological diffusion equation for the QP density, taking into account their interaction

[1] Exploiting the mutual influence of two superconductors with different bulk energy gaps has a similar effect [147].

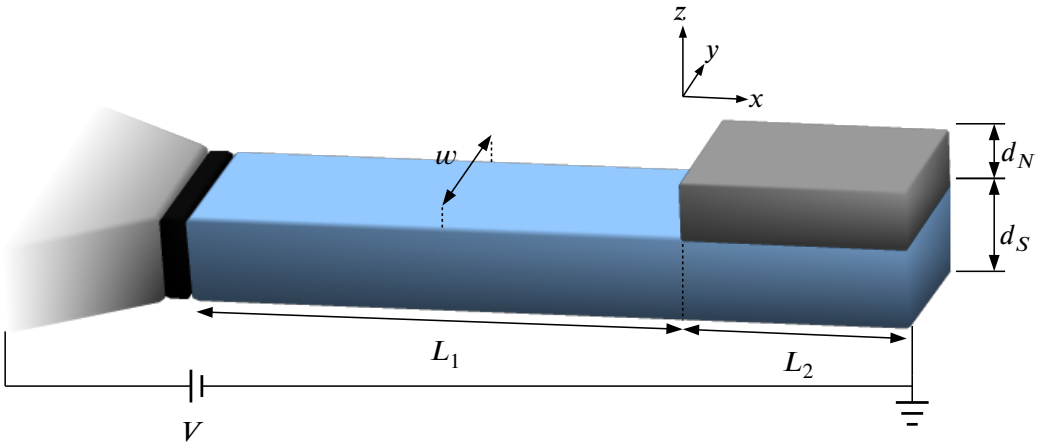

FIGURE 8.3: (Not to scale) Schematic of a QP injector with attached normal-metal trap. A mesoscopic superconducting wire (blue part) is connected to a big normal metal reservoir (partially shown by left gray part) via a thin tunnel barrier (black part). The reservoir is kept at temperature $T = 0$ K and potential eV measured from the superconductor's one. At its end the superconductor is covered in good metallic contact with another normal metal with length L_2, serving as QP trap, and is electrically grounded. In what follows, this set-up is referred to as setup 2. The trapping performance is investigated by comparing the non-equilibrium steady states of this set-up and another QP injector with the same dimensions and parameters but without attached trap. This reference set-up is called setup 1in the following.

with phonons and loss mechanisms due to QP recombination and trapping [107, 125, 126, 144, 152, 153, 154, 155, 156]. Here, a different approach is pursued, employing the Usadel formalism [157, 158, 159] which is a convenient tool to study dirty mesoscopic proximity systems in and out of equilibrium and was applied in various fields [152, 160, 161, 162, 163, 164, 165, 166, 167, 168, 169, 170, 171, 172, 173]. In particular, it was used for a detailed theory of non-equilibrium phenomena in a superconductor in contact with a normal-metal trap, given in [173]. As will be review in Sec. 10 this formalism gives access to spectral quantities such as the QP density of states (DOS), and also to non-equilibrium quantities such as the QP distribution and current densities.

8.3 Outline

This brief motivation and qualitative explanation of the working principle of quasiparticle traps is followed by a derivation of the Usadel equations in Sec. 9, which are used in this work to determine the non-equilibrium steady state of the two set-ups. In Sec. 10 the Usadel equations and physical quantities such as the DOS, quasiparticle density and current densities are expressed in terms of the trigonometric parameterization. Furthermore – even though not necessarily useful for this project but certainly interesting from a general point of view – the structure of the kinetic equations and of the current densities, partially influenced by a symmetry property of the spectral Usadel equations with respect to the quasiparticle energy, are discussed. As key role for this work, the superconducting proximity effect and the related process of Andreev reflection are reviewed in Sec. 11. There, the boundary conditions, with which the Usadel equations need to be supplemented in mesoscopic hybrid structures, are also given. The main results of this work, published as paper with the title "Role of the proximity

effect for normal-metal quasiparticle traps“ are presented in Sec. 12. This includes the derivation of a one-dimensional model for both set-ups with appropriate boundary conditions, the qualitative explanation of the numerical results with the proximity effect and the discussion of the relation between the Andreev reflection, the conversion between normal dissipative and supercurrent and the reduction of the quasiparticle density. In Sec. 14 details about the numerical solver, which is based on a relaxation method, and the approximate analytic solution to the spectral Usadel equations for the one-dimensional S_1S_2 wire part of the one-dimensional model are given.

9 Non-equilibrium superconductivity: from Gor'kov via Eilenberger to Usadel

The ultimate goal of this section is to derive the Usadel equations, which are central to Part II as all the calculations are based on them. The equations of motion for the superconducting Green's functions in Keldysh⊗Nambu space are obtained, known as Gor'kov equations. They serve as starting point for the quasiclassical approximation yielding the Eilenberger equations. In the case of dirty superconductors, characterized by frequent impurity scatterings with a mean free path much shorter than the superconducting coherence length, the quasiclassical Green's functions can be essentially averaged over the Fermi surface and obey the Usadel equations.

This section is neither meant to give a rigorous derivation nor a pedagogical stand-alone introduction. Instead it presents important steps and results which were otained during several years of work in the field of in and out of equilibrium situations in normal and superconducting metals, among others. Also, knowledge about the BCS theory of conventional superconductivity is assumed and will not be reviewed. The following description is mostly inspired by the review articles [174] by J. Rammer and H. Smith and [175] by W. Belzig et al., and J. Rammer's book "Quantum field theory for non-equilibrium states" [176] as well as N. Kopnin's book "Theory of nonequilibrium superconductivity" [177]. Besides them, the book "Green's functions and condensed matter" by G. Rickayzen, although not as detailed as the aforementioned literature regarding non-equilibrium aspects, is strongly recommended. Additionally, C. Timm's lecture notes [178] are exceptionally well and pedagogically written. Last but not least, the two classics "Superconductivity of metals and alloys" by PG de Gennes [179] and M. Tinkahm's "Introduction to superconductivity" [180] certainly mustn't be missed.

9.1 Non-equilibrium and Keldysh's technique

The central objects of this section are the single-particle Green's functions for non-equilibrium situations. Similar to the equilibrium treatment, Wick's theorem can be applied and the Dyson equation for the single-particle Green's functions is obtained.

Consider a system of electrons[2] described by the time-independent Hamiltonian $H = H_0 + V^{(2)}$, where the first term $H_0 = T + V^{(1)}$ represents non-interacting electrons, which may be exposed to an external, time-independent potential $V^{(1)}$, and $V^{(2)}$ accounts for two-body interactions stemming from e.g. electron-electron or electron-phonon interactions. The system is assumed to be in thermal equilibrium with a reservoir at temperature T and chemical potential μ. At time t_0, the system is disconnected from the reservoir which will be ignored from now on, and is subject to an external time-dependent disturbance $H'(t)$. The full Hamiltonian describing the system for times $t \geq t_0$ is then given by $\mathcal{H}(t) = H + H'(t)$.

Non-equilibrium statistical mechanics aims at describing the influence of the external perturbation on the electron system. To this end, Green's functions take a fundamental part as they constitute the connection between conveniently calculable quantities and experimentally relevant quantities.[3]

[2] The following is not exclusively restricted to electrons, but can be analogously applied to bosonic fields as phonons and photons with minor adaptations, and their mutual interactions.

[3] The Kubo formula [181] in the context of linear response theory usually expresses the susceptibility giving the response in terms of Green's functions.

In the Keldysh technique the single-particle Green's function is defined as

$$G_{c_K}(1,1') = -i \left\langle T_{c_K} \left\{ \psi(1)\psi^\dagger(1') \right\} \right\rangle_H . \tag{9.1}$$

This expression needs some explanation. The arguments of the function are given in a dense notation with the meaning $1 \equiv (\mathbf{r}_1, t_1, \sigma_1)$ and potential for including spin and other degrees of freedom as well. The time dependence of the field operators stems from their transformation into the Heisenberg picture. This is useful, since the quantum state of the system is time-independent in the Heisenberg picture. Prior to time t_0 the system was in thermal equilibrium, so that the state of the system is described by the thermal density matrix

$$\rho(H) = \frac{\mathrm{e}^{-\beta H}}{\mathrm{Tr}\left\{\mathrm{e}^{-\beta H}\right\}},$$

where the grand canonical ensemble is used. The expectation value in Eq. (9.1) is a thermal average,

$$\langle \bullet \rangle_H = \mathrm{Tr}\left\{\rho(H)\bullet\right\}.$$

The contour-ordering operator T_{c_K} orders the operators according to the position on the contour of their time arguments, including a change in sign each time the order of electron operators is swapped.[4] Thereby, the Keldysh contour c_K, shown in Fig. 9.1, consists of two separate paths c_1 and c_2, with the properties $T_{c_1} = \overrightarrow{T}$ and $T_{c_2} = \overleftarrow{T}$, with the usual time- and anti-time-ordering operators $\overrightarrow{T}$ and $\overleftarrow{T}$, respectively. Additionally, all times on c_2 proceed those on c_1. Therefore, this Green's function can be mapped onto the Keldysh space,

$$G_{c_K}(1,1') \mapsto \underline{G} \equiv \begin{pmatrix} G_{11} & G_{12} \\ G_{21} & G_{22} \end{pmatrix}, \tag{9.2}$$

with the prescription that G_{ij} is given by Eq. (9.1) with $t_1 \in c_i$ and $t_{1'} \in c_j$. The components read

$$\begin{aligned}
G_{11}(1,1') &= -i \left\langle \overrightarrow{T} \left\{ \psi(1)\psi^\dagger(1') \right\} \right\rangle \\
G_{12}(1,1') &= +i \left\langle \psi^\dagger(1')\psi(1) \right\rangle = G^<(1,1') \\
G_{21}(1,1') &= -i \left\langle \psi(1)\psi^\dagger(1') \right\rangle = G^>(1,1') \\
G_{22}(1,1') &= -i \left\langle \overleftarrow{T} \left\{ \psi(1)\psi^\dagger(1') \right\} \right\rangle .
\end{aligned}$$

In constructing the Keldysh contour initial correlations were neglected which allowed for $t_0 \to -\infty$.[5] By transforming into the interaction picture with respect to the independent-particle Hamiltonian H_0, one can express the single-particle Green's function Eq. (9.1) as [176]

$$G_{c_K}(1,1') = -i \left\langle T_{c_K} \left\{ S\psi_{H_0}(1)\psi^\dagger_{H_0}(1') \right\} \right\rangle_{H_0} \tag{9.4a}$$

$$= -i \frac{\mathrm{Tr}\left\{ \mathrm{e}^{-\beta H_0} T_{c_K} \left\{ S\psi_{H_0}(1)\psi^\dagger_{H_0}(1') \right\} \right\}}{\mathrm{Tr}\left\{\mathrm{e}^{-\beta H_0}\right\}} \tag{9.4b}$$

[4] Note that the additional factor -1 in case of fermionic operators is not due to the fermionic anti-commutation relations which only hold if the involved field operators have the same time argument.

[5] See, e.g. [174] and references therein for a discussion.

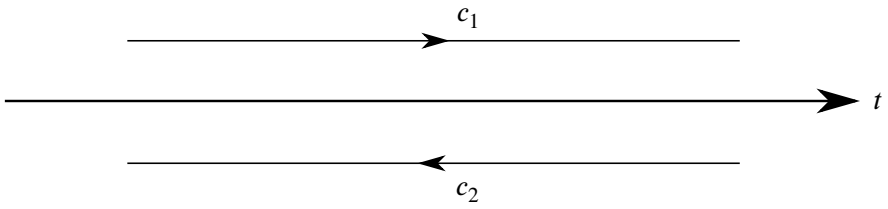

FIGURE 9.1: The Keldysh contour c_K. The path c_1 extends from $t = -\infty$ to $+\infty$, whereas c_2 points in the opposite time direction. The arrows show in direction of increasing "time" along the respective path. Hence, ordering on c_1 corresponds to the usual time-ordering, whereas ordering on c_2 corresponds to anti-time-ordering. All times on c_2 proceed those on c_1.

with

$$S = \exp\left\{-\frac{i}{\hbar}\int\limits_{c_K}\left[V^{(2)}_{H_0}(\tau) + H'_{H_0}(\tau)\right]\mathrm{d}\tau\right\},$$

where the index H_0 in the operators indicates their transformation into the interaction picture with respect to H_0. The expressions Eq. (9.4a)-(9.4b), although seeming to be even more complicated than the definition Eq. (9.1), have in fact several properties which make this representation very useful and the starting point for perturbation theory: The particle-particle interaction and the perturbation, described by the terms $V^{(2)}$ and $H'(t)$, respectively, both enter the Green's function only at one position, namely via S. Furthermore, $V^{(2)}$ and $H'(t)$ are both transformed into the interaction picture with respect to H_0, and thus, all field operators too.[6] Last but not least, the density matrix $\rho(H)$ is replaced by $\rho(H_0)$, i.e. a statistical average over a system of free, non-interacting particles. Due to the S-terms, the terms Eq. (9.4a)-(9.4a) contain products of multiple different field operators, as for example $\psi^\dagger_{H_0}\psi_{H_0}\psi_{H_0}\psi^\dagger_{H_0}$, which all give rise to many-particle Green's functions. The crucial point here is that these Green's functions describe a system of non-interacting particles. This is important in order to employ Wick's theorem [182] and express the many-particle Green's functions in terms of single-particle ones. The Green's functions of non-interacting particles have a key role in the Green's function formalism. In order to highlight this fact, they are adorned with an index "0". At this point, a "physical" proof of Wick's theorem is presented rather than a rigorous and detailed mathematical one, which can be found for example in [183, 184]. This proof goes as follows: First, the theorem is stated, and then it is made plausible using a simple example. According to Wick's theorem, an n-particle Green's function of non-interacting particles, $G^{(n)}_0(1,\dots,n;1',\dots n')$ can be written in terms of single-particle Green's functions $G_0(i,j')$ as the determinant of an $n\times n$ matrix,

$$G^{(n)}_0(1,\dots,n;1',\dots n') = \begin{vmatrix} G_0(1,1') & \dots & G(1,n') \\ \vdots & \ddots & \vdots \\ G_0(n,1') & \dots & G_0(n,n') \end{vmatrix}. \tag{9.5}$$

[6] In second quantization, a spin independent particle-particle interaction for instance can be expressed in terms of field operators as $2V^{(2)} = \sum\limits_{\sigma\sigma'}\int \mathrm{d}\mathbf{r}_1\int \mathrm{d}\mathbf{r}_2\psi^\dagger_\sigma(\mathbf{r}_1)\psi^\dagger_{\sigma'}(\mathbf{r}_2)V(\mathbf{r}_1-\mathbf{r}_2)\psi_{\sigma'}(\mathbf{r}_2)\psi_\sigma(\mathbf{r}_1)$.

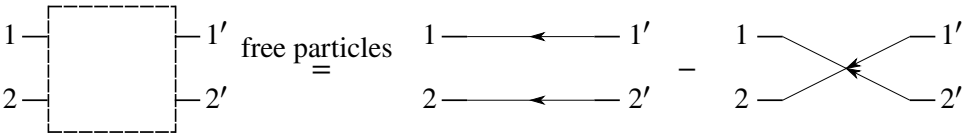

FIGURE 9.2: Graphic illustration of Wick's theorem applied to the two-particle Green's function $G^{(2)}(1,2;1',2')$. For two interacting particles, one at $(\mathbf{r}_{1'}, t_{1'})$ and the other at $(\mathbf{r}_{2'}, t_{2'})$, there is an infinite number of multiple scattering processes possible, depicted as black box (dashed empty square), to bring the particles to $(\mathbf{r}_1, t_1)$ and $(\mathbf{r}_2, t_2)$. For free, non-interacting and indistinguishable particles, there are just two possibilities, both only involving single-particle Green's functions $G_0(i, i')$ (solid line with middle arrow head), which interfere destructively due to the fermionic nature.

It is instructive to look at the case $n = 2$, in which the two-particle Green's function is according to Eq. (9.5) expressed as

$$G_0^{(2)}(1,2;1',2') = G_0(1,1')G_0(2,2') - G_0(1,2')G_0(2,1').$$

This equation is illustrated in Fig. 9.2 and interpreted as follows: Just as the single-particle Green's function $G(1,1')$ gives the probability amplitude to find a particle at $(\mathbf{r}_1, t_1)$ after its creation at $(\mathbf{r}_{1'}, t_{1'})$, the two-particle Green's function $G^{(2)}(1,2;1',2')$ gives the probability amplitude for detecting one particle at $(\mathbf{r}_1, t_1)$ and the other at $(\mathbf{r}_2, t_2)$ after their creation at $(\mathbf{r}_{i'}, t_{i'})$ for $i = 1, 2$.[7] In the case of free, non-interacting and indistinguishable particles, such an outcome is only possible if either one particle propagated from $(\mathbf{r}_{1'}, t_{1'})$ to $(\mathbf{r}_1, t_1)$ and the other from $(\mathbf{r}_{2'}, t_{2'})$ to $(\mathbf{r}_2, t_2)$, described by $\hat{G}_0(1,1')\hat{G}_0(2,2')$, or that one particle propagated from $(\mathbf{r}_{2'}, t_{2'})$ to $(\mathbf{r}_1, t_1)$ and the other from $(\mathbf{r}_{1'}, t_{1'})$ to $(\mathbf{r}_2, t_2)$, described by $G_0(1,2')G_0(2,1')$.[8][9]

Now, Eq. (9.4a) is able to show its full potential: Using Wick's theorem, the many-particle Green's functions can be expressed as an infinite sum of single-particle Green's functions with increasing number of interactions, each describing the propagation of a particle from $(\mathbf{r}_{1'}, t_{1'})$ to $(\mathbf{r}_1, t_1)$ with intermediate scattering events followed by free propagation. Taming the infinite sum over single-particle Green's functions can be accomplished conveniently with the concept of self-energies. The irreducible parts in the series serve as modules or building blocks for the reducible parts. Using the notation

$$(A * B)(1,1') = \int \mathrm{d}\mathbf{r}_2 \int_{c_K} \mathrm{d}t_2 A(1,2)B(2,1'),$$

each irreducible part can be expressed as $G_0 * \Sigma_j * G_0$, where Σ_j is specific for the irreducible part at hand and describes the specific intermediate scattering events due to the interactions.

[7] This interpretation holds for any n-particle Green's function, regardless of the number n of participating particles and their interactions.

[8] In case the order operator in Eq. (9.1) takes action and swaps the order of the field operators, it is said that a hole instead of a particle is created at $(\mathbf{r}_1, t_1)$ and propagates to $(\mathbf{r}_{1'}, t_{1'})$. The proof works for holes in the same way.

[9] This interpretation is explicitly based on the fact that the particles are free and thus can propagate without scattering. However, as noted earlier, the electrons may be exposed to an external, time-independent potential $V^{(1)}$ as well, depriving them of their freedom. Wick's theorem as given by Eq. (9.5) still holds, and its physical proof can be saved by another physical proof: Particle-particle interactions are necessary for two-particle correlations. These can be quantified using Green's functions as $C_2(1,2;1',2') = G^{(2)}(1,2;1',2') - G(1,1')G(2,2') + G(1,2')G(2,1')$. For a system of non-interacting particles, C_2 has to vanish which immediately yields Wick's theorem applied to the two-particle Green's function $G_0^{(2)}$, even though the particles may not be free.

The full self-energy is then the sum over all these terms, $\Sigma = \sum_j \Sigma_j$. This allows to write

$$G = G_0 + \underbrace{G_0 * \Sigma * G_0}_{\text{irreducible parts}} + G_0 * \Sigma * G_0 * \Sigma * G_0 + \dots \tag{9.6a}$$

$$= G_0 + G_0 * \Sigma * G, \tag{9.6b}$$

where from Eq. (9.6a) to Eq. (9.6b) the term $G_0 * \Sigma$ was factored out in order to use Eq. (9.6a) in the other factor. Eq. (9.6b) is called the Dyson equation. The benefit it provides for approximating the Green's function to be calculated, is easily evident when applying it to systems which are invariant under translations in time and space.[10] Those systems are preferably studied with Green's functions $\tilde{G}(\mathbf{k}, \omega)$ in frequency-momentum-space connected to those used here via respective Fourier transformations, under which the convolutions $*$ are transformed into ordinary products. Thus, Eq. (9.6b) can be solved easily, yielding

$$\tilde{G} = \frac{\tilde{G}_0}{1 - \tilde{G}_0 \tilde{\Sigma}}. \tag{9.7}$$

There is still no hope of finding the exact Green's function, since this amounts to calculating the full self-energy, which itself consists of infinitely many different contributions. However, this specific functional form of Eq. (9.7) has two important properties: First, $\tilde{G}$ is expressed in terms of $\tilde{\Sigma}$ via a non-polynomial function. Hence, doing approximations on the level of the self-energy by taking into account only a finite sub-set of contributions, $\Sigma \approx \sum_{j<j_{\max}} \Sigma_j$, still leads to an infinite amount of reducible parts as approximation on the level of the Green's functions. This can be understood by considering the full Taylor expansion in Σ, or by Eq. (9.6a). Second, the poles of $\tilde{G}$ are immediately obtained. As it will be seen later, they hold information about quasiparticle energy and lifetimes.

The Dyson equation (9.6b) can also be written as matrix equation to account for the matrix representation (9.2) of the Green's function and the self-energy. The complexity of the matrix structure can be further reduced owing to the fact that the components of $\underline{G}$ are not linear independent but instead fulfill the property

$$G_{11} + G_{22} = G_{12} + G_{21}. \tag{9.8}$$

While the final matrix representation is arbitrary, the most convenient and common choice is to perform the Keldysh rotation,

$$\check{A} = L \hat{\tau}_3 \underline{A} L^\dagger$$

with

$$L = \frac{1}{\sqrt{2}} \left(\hat{\tau}_0 - i \hat{\tau}_2 \right)$$

and the Pauli matrices

$$\hat{\tau}_0 = \begin{pmatrix} 1 & 0 \\ 0 & 1 \end{pmatrix} \quad \hat{\tau}_1 = \begin{pmatrix} 0 & 1 \\ 1 & 0 \end{pmatrix} \quad \hat{\tau}_2 = \begin{pmatrix} 0 & -i \\ i & 0 \end{pmatrix} \quad \hat{\tau}_3 = \begin{pmatrix} 1 & 0 \\ 0 & -1 \end{pmatrix}, \tag{9.9}$$

[10] Admittedly, this is a great restriction, since any (interesting) particle-particle interaction breaks the translation invariance. However, metals with random impurities at which electrons can scatter, can be studied using spatially averaged, and thus translationally invariant Green's functions. See for instance [183].

on the Green's functions and self-energies. This particular choice leads to the upper triangular form

$$\check{A} = \begin{pmatrix} A_R & A_K \\ 0 & A_A \end{pmatrix}$$

of all included matrices due to Eq. (9.8), with the usual retarded

$$A_R(1,1') = \Theta\left(t_1 - t_{1'}\right)\left(A^{>}(1,1') - A^{<}(1,1')\right) \tag{9.10a}$$

and advanced

$$A_A(1,1') = -\Theta\left(t_{1'} - t_1\right)\left(A^{>}(1,1') - A^{<}(1,1')\right) \tag{9.10b}$$

component and the Keldysh component

$$A_K(1,1') = A^{>}(1,1') + A^{<}(1,1'). \tag{9.10c}$$

Additionally, the product of upper triangular matrices has an upper triangular form as well. In the case of the Green's function, this particular form allows for a separate physical interpretation of the components: generally speaking, G_R and G_A give information about the states of the system, whereas the Keldysh component describes their occupation and is thus particularly important for non-equilibrium situations.

In Keldysh space, denoted by "$\check{}$", the Dyson equation is found to be

$$\check{G} = \check{G}_0 + \check{G}_0 \otimes \check{\Sigma} \otimes \check{G} \tag{9.11}$$

with the bilinear form

$$(A \otimes B)(1,1') = \int \mathrm{d}\mathbf{r}_2 \int_{-\infty}^{\infty} \mathrm{d}t_2 A(1,2)B(2,1'),$$

which generalizes "$*$" to matrices A, B. Operating with $\check{G}_0^{-1}(1,1') = \delta(1,1')\left(i\hbar\partial_{t_1} - h(1)\right)$[11] with the Dirac delta $\delta(1,1') = \delta_{\sigma_1,\sigma_{1'}}\delta(\mathbf{r}_1 - \mathbf{r}_{1'})\delta(t_1 - t_{1'})$ and the single-particle Hamiltonian $h(1) = -\hbar^2/(2m)\nabla^2_{\mathbf{r}_1} + e\phi(1) - \mu$ from the left, the above equation can be cast in the form

$$\left(\check{G}_0^{-1} - \check{\Sigma}\right) \otimes \check{G} = \hbar\delta(1,1'). \tag{9.12}$$

Analogously, in Eq. (9.6a) the term $\Sigma * G_0$ can be factored out to the right, which yields the conjugate Dyson equation

$$\check{G} \otimes \left(\check{G}_0^{-1} - \check{\Sigma}\right) = \hbar\delta(1,1') \tag{9.13}$$

9.2 Conventional superconductivity and Gor'kov equations

The Green's functions introduced in the last section serve as an appropriate tool to study superconductivity in non-equilibrium situations. A microscopic treatment follows from the Dyson equations when taking into account the attractive electron interaction responsible for superconductivity.

[11] Unit matrices are suppressed.

An attractive interaction between electrons leads to bound electron states, a phenomenon known as Cooper instability [185]. In the BCS-theory [186, 187] of conventional superconductivity, this pairing interaction is mediated by phonons. The resulting bound states pair the degenerate electron states $|\mathbf{k}\uparrow\rangle$ and $|-\mathbf{k}\downarrow\rangle$ which transform into each other via time reversal. Due to the attractive interaction it is energetically favorable for the Cooper pairs to form a spin-singlet state, for which the spatial part of the pair wavefunction is symmetric under particle exchange[12], leading to a smaller mean distance between the electrons than in a spatially antisymmetric state.[13] The decisive property of superconductivity is the collective behavior of the Cooper pairs as one entity, described by a phase-coherent many-body wave function. This wave function includes a macroscopic number of particles, which makes superconductivity to a macroscopic quantum phenomenon. The simplified picture of a macroscopic, BEC-like occupation of a single quantum state by the bosonic Cooper pairs, which might hold for superconductivity with preformed pairs as it can be found in some disordered, amorphous superconductors[14], is in general not without flaws [192].

By introducing the Nambu pseudospinor field [193]

$$\hat{\Psi}(\mathbf{r},t) = \begin{pmatrix} \psi_\uparrow(\mathbf{r},t) \\ \psi_\downarrow^\dagger(\mathbf{r},t) \end{pmatrix},$$

the pairing in the superconducting state can be conveniently incorporated into one matrix single-particle Green's function given by

$$\hat{G}(1,1') = -i\left\langle \overrightarrow{T}\left\{\hat{\Psi}(1)\hat{\Psi}^\dagger(1')\right\}\right\rangle = \begin{pmatrix} G(1,1') & F(1,1') \\ F^\dagger(1,1') & G^\dagger(1,1') \end{pmatrix},$$

where any product of two such pseudospinor fields is to be understood as the tensor product of the two matrices. Here, the anomalous component $F = -i\left\langle \overrightarrow{T}\left\{\psi_\uparrow\psi_\downarrow\right\}\right\rangle$ gives the pair amplitude, which vanishes in the normal state, but is non-zero in the superconducting state due to the Cooper pairing. When using the Nambu pseudospinor field in the Keldysh technique above, all components of the triangular matrices are to be replaced by 2×2 matrices. From now on, a matrix $\check{A}$ denotes such a 4×4 matrix in Keldysh⊗Nambu space.

The Gor'kov equations of motion for superconducting Green's functions [194] can be obtained from the Dyson equations (9.12)-(9.13) by using for the self-energy the term stemming from the attractive interaction responsible for the pairing[15]. This reads

$$\check{\Delta}(1,1') = \delta(1,1')\begin{pmatrix} \hat{\Delta}(1) & 0 \\ 0 & \hat{\Delta}(1) \end{pmatrix} \quad \hat{\Delta} = \begin{pmatrix} 0 & \Delta(1) \\ \Delta^*(1) & 0 \end{pmatrix} \tag{9.14}$$

[12] Due to Pauli's exclusion principle the anomalous Green's function (to be defined below) must be antisymmetric under particle exchange. Not only are their spin and spatial variables subject to this exchange but also their band indices and times (even though Pauli's exclusion principle is an equal-time relation), the latter giving rise to the classification of even- and odd-frequency pairing [188, 189]. The BCS-theory neglects the bands and assumes an even-frequency pairing, forcing the spin part to a spin-singlet.

[13] This simple argument holds only for the BCS-Hamiltonian describing conventional superconductors and cannot account for more complex situations as in some high-temperature or strongly correlated heavy-fermion superconductors with d- or p-wave pairing where the Coulomb repulsion is mitigated in space – due to the spatial antisymmetry (p) or higher total momentum (d) – and/or in time due to odd-frequency pairing. See, e.g., [190] and references therein for more details and examples.

[14] See, for example [191] and references therein.

[15] Interactions other than the pairing interaction will be considered separately at a later point.

with the superconducting order parameter $\Delta(1) = \lambda \lim_{1'\to 1^+} F^\dagger(1', 1)$, where λ characterizes the strength of the attractive interaction. The Gor'kov equations thus read

$$\left(\check{G}_0^{-1} + \check{\Delta}\right) \otimes \check{G} = \hbar\delta(1, 1') \tag{9.15a}$$
$$\check{G} \otimes \left(\check{G}_0^{-1} + \check{\Delta}\right) = \hbar\delta(1, 1') \tag{9.15b}$$

with the single-particle Hamiltonian in Keldysh⊗Nambu space

$$\check{G}_0^{-1}(1, 1') = \delta(1, 1') \left(i\hbar\check{\tau}_3 \frac{\partial}{\partial t_1} + \frac{\hbar^2}{2m}\nabla^2_{\mathbf{r}_1} - e\phi(1) + \mu \right),$$

where

$$\check{\tau}_3 = \begin{pmatrix} \hat{\tau}_3 & 0 \\ 0 & \hat{\tau}_3 \end{pmatrix}$$

and unit matrices are suppressed. Magnetic fields can be included via the gauge-invariant spatial derivative $\nabla_{\mathbf{r}_1} - ie\mathbf{A}(\mathbf{r})\check{\tau}_3$.

The Wigner transformation

$$\begin{aligned} \mathbf{R} &= \tfrac{\mathbf{r}_1 + \mathbf{r}_{1'}}{2}, \quad \mathbf{r} = \mathbf{r}_1 - \mathbf{r}_{1'} \\ T &= \tfrac{t_1 + t_{1'}}{2}, \quad t = t_1 - t_{1'} \end{aligned}$$

allows for a separation in variables $(t, \mathbf{r})$, describing the microscopic properties, and variables $(T, \mathbf{R})$, describing the macroscopic properties of the system. To this end, all functions are Fourier transformed with respect to the relative coordinates,

$$A(X, p) \equiv \int \mathrm{e}^{-ipx/\hbar} A\left(X + \frac{x}{2}, X - \frac{x}{2}\right) \mathrm{d}x$$

with the abbreviated notation analogous to [174, 176]

$$\begin{aligned} X &= (T, \mathbf{R}), \qquad x = (t, \mathbf{r}) \\ p &= (E, \mathbf{p}), \quad px = -Et + \mathbf{p}\cdot\mathbf{r}. \end{aligned}$$

In this representation, the convolution $A \otimes B$ is given by[16]

$$(A \otimes B)(X, p) = \mathrm{e}^{\frac{i\hbar}{2}\left(\partial_X^A \partial_p^B - \partial_p^A \partial_X^B\right)} A(X, p) B(X, p),$$

where

$$\partial_X = \left(-\frac{\partial}{\partial T}, \nabla_{\mathbf{R}}\right), \quad \partial_p = \left(-\frac{\partial}{\partial E}, \nabla_{\mathbf{p}}\right)$$

and

$$\partial_X^A \partial_p^B \equiv -\frac{\partial^A}{\partial T}\frac{\partial^B}{\partial E} + \nabla^A_{\mathbf{R}} \cdot \nabla^B_{\mathbf{p}}. \tag{9.16}$$

In the Wigner representation the single-particle Hamiltonian becomes

$$G_0^{-1}(X, p) = E\check{\tau}_3 - \xi_{\mathbf{p}} - e\phi(\mathbf{R}, T),$$

[16] For a proof, see e.g. [176].

where $\xi_{\mathbf{p}} = p^2/(2m) - \mu$. In deriving this expression, it was assumed that the external potentials are functions of the center-of-mass variables only as their variations on the microscopic length and time scales are negligible. Analogously, derivatives with respect to the center-of-mass variables take into account the lack of translation invariance due to the external potentials, and are thus small compared to the derivatives with respect to the relative coordinates.

The Gor'kov equations (9.15a)-(9.15b) provide a full description of superconducting structures. However, finding their solution can be a very cumbersome task, especially in inhomogeneous systems as for example hybrid structures where spatial variations of the superconducting order parameter cannot be neglected anymore [195]. The quasiclassical approximation [196, 197] will be introduced in the next section.

9.3 The quasiclassical approximation and the Eilenberger equations

While the quasiclassical approximation can be applied to generally time-dependent situations [198], the following formulation is restricted to thermal equilibrium and non-equilibrium steady-states, in which the T-dependence in the Wigner representation of the Green's functions vanishes.

Since the single-particle Green's function $\check{G}(1,1')$ oscillates as a function of the relative coordinate $\mathbf{r} = \mathbf{r}_1 - \mathbf{r}_{1'}$ on a length scale of the Fermi wavelength λ_F, its Wigner transformation is peaked near the Fermi surface. When neglecting effects resulting from these oscillations and the interference of single-electron wavefunctions, such as weak localization, it is possible to eliminate the dependence on the relative cooridante [175]. Furthermore, this approach is sufficient for describing proximity systems where the Fermi wavelength is much shorter than the relevant length scale given by the superconducting coherence length. The elimination of the $\mathbf{r}$-dependence is accomplished by integrating over $\xi_p = p^2/(2m) - \mu$ [196, 197]. This yields the quasiclassical Green's function defined as

$$\check{g}\left(\mathbf{R}, E, \mathbf{v}_F\right) = \frac{i}{\pi\hbar} \fint \check{G}\left(\mathbf{R}, E, \xi, \mathbf{v}_F\right) \mathrm{d}\xi, \tag{9.17}$$

where the integration is along a specific contour allowing to separate low-energy contributions relevant for transport processes from high-energy contributions, which do not contribute and would cause a logarithmic divergence of the integral stemming from the integrand [196].[17] The dependence on the direction of the velocity at the Fermi surface may not be discriminated.

Subtracting the Gor'kov equation (9.15a) from its conjugated form Eq. (9.15b), and neglecting short-range oscillations by expanding the convolutions of the form Eq. (9.16) therein up to first order in $\mathbf{R}$, yields the Eilenberger equation of motion for the quasiclassical Green's functions [175]

$$-\hbar\mathbf{v}_F \cdot \nabla_{\mathbf{R}} \check{g}\left(\mathbf{R}, E, \mathbf{v}_F\right) = \left[-iE\check{\tau}_3 + \check{\Delta}(\mathbf{R}), \check{g}\left(\mathbf{R}, E, \mathbf{v}_F\right)\right]. \tag{9.18}$$

Here, $\check{\Delta}(\mathbf{R}) = \tau_0 \otimes \hat{\Delta}(\mathbf{R})$ denotes the Wigner transform of $\check{\Delta}(1,1')$ defined in Eq. (9.14).

9.4 Dirty superconductors and the Usadel equations

The only interaction considered so far is the pairing interaction associated with the term $\check{\Delta}$. Isotropic elastic impurity-scattering within the Born approximation can be incorporated by

[17] For more details, see e.g. [176].

adding the self-energy

$$\check{\sigma}(\mathbf{R}, E) = \frac{\hbar}{2\tau} \left\langle \check{g}\left(\mathbf{R}, E, \mathbf{v}_F\right) \right\rangle_{\mathbf{v}_F}$$

to $\check{\Delta}$ in the the Eilenberger equation (9.18), where $\langle \bullet \rangle_{\mathbf{v}_F}$ denotes averaging over the Fermi surface and τ is the elastic scattering time.[18]

One frequently has to deal with superconductors where the elastic mean free path $l_e = v_F \tau$ is much shorter than the system dimensions and the superconducting coherence length, i.e. the associated self-energy dominates all other terms in the Eilenberger equation. This is the defining condition for dirty superconductors. A characteristic of those systems is a randomized quasiparticle motion over the Fermi surface, leading to a diffusive motion in real-space and almost isotropic Green's functions in momentum-space. This allows for further simplification of the Eilenberger equation. Expanding the Green's function into spherical harmonics,[19]

$$\check{g}(\mathbf{R}, E, \mathbf{v}_F) = \check{g}_s(\mathbf{R}, E) + \mathbf{v}_F \check{g}_p(\mathbf{R}, E),$$

and appropriately averaging the Eilenberger equation over the Fermi surface with the assumption $\check{g}_s \pm \mathbf{v}_F \check{g}_p \approx \check{g}_s$ and the dirty-limit condition, one can show [157, 175, 199] that the s-wave component $\check{g}_s$, from now on written as $\check{g}_s(\mathbf{R}, E) \equiv \check{G}(\mathbf{r}, E)$, obeys the Usadel equation [157]

$$\hbar D \nabla \left(\check{G} \nabla \check{G}\right) = \left[-iE\check{\tau}_3 + \check{\Delta}, \check{G}\right] \tag{9.19}$$

with the diffusion constant $D = \tau v_F^2/3$. Measuring the energy in units of the BCS bulk energy gap Δ_{BCS}, $E = \epsilon \Delta_{\mathrm{BCS}}$, and length in units of the superconducting coherence length $\xi_0 = \sqrt{\hbar D/\Delta_{\mathrm{BCS}}}$, the Usadel equation reads

$$\nabla \left(\check{G} \nabla \check{G}\right) = \left[-i\epsilon\check{\tau}_3 + \check{\Delta}, \check{G}\right]. \tag{9.20}$$

The superconducting order parameter measured in units of Δ_{BCS} entering the Usadel equation (9.20) via the pairing term $\check{\Delta}$ is given by

$$\Delta = \frac{N_0 \lambda}{8i} \int \mathrm{Tr}\left\{\left(\hat{\tau}_1 - i\hat{\tau}_2\right)\hat{K}\right\} \mathrm{d}\epsilon. \tag{9.21}$$

Here, N_0 denotes the density of states (DOS) at the Fermi energy. In deriving this expression the particle-hole symmetry, i.e. a DOS symmetric (or constant) around the Fermi energy, was assumed.

Since Δ itself depends on the Green's function via the Keldysh component $\hat{K}$, the set of equations (9.20) and (9.21) has to be solved self-consistently. Exact analytic solutions exist only in few cases, e.g. at thermal equilibrium or homogeneous non-equilibrium situations.[20] The numerical procedure to find the solution for given boundary conditions will be presented in a later section.

[18] Treating general elastic scattering within the Born approximation introduces next to the scattering lifetime τ also the transport lifetime τ_{tr}, which is central in the transport theory of metals and determines the elastic mean free path via $l_e = v_F \tau_{\mathrm{tr}}$. For isotropic elastic scattering both times coincide, $\tau_{\mathrm{tr}} = \tau$.

[19] For homogeneous systems in thermal equilibrium there exists no preferred direction neither in real nor k-space, so that all terms higher than the s-wave component $\check{g}_s$ vanish.

[20] See, e.g. [161], where a mesoscopic superconducting wire is exposed to an homogeneous perpendicular magnetic field and is traversed by a homogeneous supercurrent.

10 Usadel equations in the trigonometric parameterization

As was noted by [175], the quasiclassical Green's function Eq. (9.17) is a linear combination of Pauli matrices not including the unit matrix. Therefore, its square is proportional to the unit matrix, $\check{g}^2 = c\check{\tau}_0$, with some not necessarily constant proportionality factor. Multiplying the Eilenberger equation (9.18) with $\check{g}$ once from left, once from right and adding both obtained equations, the resulting equation reads

$$-\hbar \mathbf{v}_F \cdot \nabla c\check{\tau}_0 = \left[-iE\check{\tau}_3 + \check{\Delta}, \check{g}^2\right] = 0,$$

since the commutator with $\check{g}^2 \propto \check{\tau}_0$ vanishes. Hence, the Eilenberger equations preserve the norm c, which can be determined by the asymptotic behavior of $\check{g}$. In a structure containing a sufficiently large superconductor, whose interior is described by the known equilibrium bulk solution to the homogeneous Gor'kov equations [194], c is determined to be unity, $c = 1$. With the quasiclassical Green's functions, the over the Fermi surface averaged Green's functions $\check{G}$ entering the Usadel equations (9.19) are normalized as well, $\check{G}^2 = \check{\tau}_0$. This gives for the diagonal components

$$\hat{R}^2 = \hat{A}^2 = \hat{\tau}_0 \tag{10.1a}$$

and for the Keldysh component

$$\hat{R}\hat{K} + \hat{K}\hat{A} = 0. \tag{10.1b}$$

Eq. (10.1a) can be exploited for convenient parameterizations [175] of the retarded component. Here, the trigonometric parameterization is used, in which the retarded Green's function is expressed as

$$\hat{R} = \begin{pmatrix} \cos(\theta) & \sin(\theta)\,\mathrm{e}^{i\chi} \\ \sin(\theta)\,\mathrm{e}^{-i\chi} & -\cos(\theta) \end{pmatrix} \tag{10.2a}$$

with the complex angle $\theta(\mathbf{r}, E)$ and *complex* phase $\chi(\mathbf{r}, E)$. From the definitions of the retarded and advanced Green's functions in Nambu space Eqs. (9.10a)-(9.10b) it follows $\hat{A}(1, 1') = -\tau_3 \hat{R}(1', 1)^\dagger \tau_3$, which carries over to their quasiclassical analogues, giving

$$\hat{A}(\mathbf{r}, E) = -\hat{\tau}_3 \hat{R}^\dagger(\mathbf{r}, E)\hat{\tau}_3.$$

The condition Eq. (10.1b) for the Keldysh component is fulfilled by

$$\hat{K} = \hat{R}\hat{h} - \hat{h}\hat{A} \tag{10.2b}$$

with the distribution matrix

$$\hat{h} = f_L + f_T\hat{\tau}_3, \tag{10.2c}$$

where the distribution functions f_L and f_T are odd and even with respect to the Fermi surface, respectively. The distribution matrix can be chosen to be diagonal due to its ambiguity [200],

which allows for the separation into even and odd components [201, 202]. In thermal equilibrium at temperature T the distribution functions are spatially constant[21] and given by

$$f_L = \tanh\left(\frac{E}{2k_B T}\right) \tag{10.3}$$

$$f_T \equiv 0. \tag{10.4}$$

With the parameterization Eq. (10.2b) and the expression for the distribution matrix Eq. (10.2c) the order parameter Eq. (9.21) normalized to Δ_{BCS} is given by

$$\Delta = \frac{N_0 \lambda}{4i} \int_{-\frac{\hbar\omega_D}{\Delta_{\mathrm{BCS}}}}^{\frac{\hbar\omega_D}{\Delta_{\mathrm{BCS}}}} \left[\sin(\theta)\, \mathrm{e}^{i\chi}\left(f_L - f_T\right) - \sin\left(\theta^*\right) \mathrm{e}^{i\chi^*}\left(f_L + f_T\right)\right] \mathrm{d}\epsilon. \tag{10.5}$$

In fact, with $\check{g}$ as a solution to the Eilenberger equations, $\check{g}^2, \check{g}^3, \ldots$ are solutions as well [176], which is why an additional requirement on the quasiclassical Green's functions next to the Eilenberger equations has to be imposed [203] in order to obtain a unique solution. The above requirement $\check{g}^2 = c\check{\tau}_0$ cuts off this hierarchy of solutions and is consistent with the Eilenberger equations for spatially constant c, as shown above. Note that this argument does not apply to the Usadel equations (9.19). However, they are consistent with the normalization condition, which can be seen as follows: Again, multiplying the Usadel equations with $\check{G}$ once from left, once from right and adding both obtained equations yields

$$\check{G}\nabla\left(\check{G}\nabla\check{G}\right) + \left(\nabla\left(\check{G}\nabla\check{G}\right)\right)\check{G} = 0.$$

Just as in the case of the Eilenberger equations, the RHS vanished due to the normalization condition. Further, after performing the derivatives on the LHS, the property $\check{G}\nabla\check{G} = -\left(\nabla\check{G}\right)\check{G}$, which follows from the normalization, can be used to arrive at

$$\nabla^2\check{G} + 2\left(\nabla\check{G}\right)^2\check{G} + \check{G}\left(\nabla^2\check{G}\right)\check{G} = 0.$$

The LHS of this equations equals $\left(\nabla^2\check{G}^2\right)\check{G}$, which vanishes due to the normalization. Hence, all together a true statement is obtained, which shows that the Usadel equations are indeed consistent with the normalization condition.

10.1 Spectral Usadel equations

The retarded component of the Usadel equations (9.20) reads

$$\nabla\left(\hat{R}\nabla\hat{R}\right) = \left[-i\epsilon\hat{\tau}_3 + \hat{\Delta}, \hat{R}\right] \tag{10.6}$$

[21] Note that the system itself might be spatially inhomogeneous.

and gives an equation for the retarded Green's function $\hat{R}$. Multiplying both sides with τ_3 and taking the trace[22] yields with the trigonometric parameterization Eq. (10.2a)

$$\nabla \cdot \left(-i \sin^2(\theta) \nabla \chi\right) = \sin(\theta) \left(\Delta e^{-i\chi} - \Delta^* e^{i\chi}\right), \tag{10.7a}$$

Note that this equation also follows from the (1, 1)-component of the Eq. (10.6). Here, the identities

$$\begin{gathered} \mathrm{Tr}\left\{\left[\hat{\tau}_3, \hat{M}\right] \hat{\tau}_3\right\} = 0 \\ \mathrm{Tr}\left\{\left[\hat{\Delta}, \hat{R}\right] \hat{\tau}_3\right\} = 2\,\mathrm{Tr}\left\{\hat{\tau}_3 \hat{\Delta} \hat{R}\right\} = 2 \sin(\theta) \left(\Delta e^{-i\chi} - \Delta^* e^{i\chi}\right), \end{gathered}$$

valid for an arbitrary matrix $\hat{M}$, were used. A second equation can be obtained from the (1, 2)-component, which reads

$$\frac{1}{2}\nabla^2\theta + \left(i\epsilon - \frac{1}{2}\cos(\theta)(\nabla\chi)^2\right)\sin(\theta) + \frac{1}{2}\cos(\theta)\left(\Delta e^{-i\chi} + \Delta^* e^{i\chi}\right) = 0. \tag{10.7b}$$

In order to derive this equation a term $\nabla^2\chi$ was replaced using the first equation (10.7a). The two quantities θ and χ are determined by these two equations. The two other equations stemming from the components (2, 1) and (2, 2) are the same as those above.[23]

The spectral Usadel equations (9.19)-(9.20) determine energy-dependent quantities, such as the local density of states (LDOS), which is given by

$$N_S(\mathbf{r}, E) = \frac{N_0}{4}\mathrm{Tr}\left\{\hat{\tau}_3 \left(\hat{R}(\mathbf{r}, E) - \hat{A}(\mathbf{r}, E)\right)\right\} = N_0 \mathrm{Re}\left\{\cos\left(\theta(\mathbf{r}, E)\right)\right\} \tag{10.8}$$

with the normal-state DOS at the Fermi energy N_0.

The spectral Usadel equations (10.6) possess a symmetry, which will determine the structure of non-equilibrium quantities such as the current densities (see Sec. 10.2) and relates the solutions to energies ϵ and $-\epsilon$. Let $\hat{R}$ be the solution to the spectral Usadel equations (10.6) to energy ϵ, i.e.

$$\nabla\left(\hat{R}\nabla\hat{R}\right) = \left[-i\epsilon\hat{\tau}_3 + \hat{\Delta}, \hat{R}\right].$$

Taking the Hermitian conjugate on both sides of this equations yields

$$\nabla\left(\hat{R}^\dagger\nabla\hat{R}^\dagger\right) = \left[+i\epsilon\hat{\tau}_3 + \hat{\Delta}, \hat{R}^\dagger\right],$$

showing that $\hat{R}^\dagger$ is a solution to the spectral Usadel equations to energy $-\epsilon$. Here, on the LHS

$$\nabla\left(\hat{R}^\dagger\right)\hat{R}^\dagger = -\hat{R}^\dagger\nabla\hat{R}^\dagger,$$

following from the normalization condition $\left(\hat{R}^\dagger\right)^2 = \hat{\tau}_0$, and on the RHS

$$\left[\hat{M}, \hat{N}\right]^\dagger = -\left[\hat{M}^\dagger, \hat{N}^\dagger\right]$$

[22] Taking the trace of Eq. (10.6) directly yields an empty statement: On the one hand the trace of a commutator of two arbitrary matrices vanishes, $\mathrm{Tr}\{[A, B]\} = 0$, and on the other hand the normalization $\hat{R}^2 = \hat{\tau}_0$ implies that $\mathrm{Tr}\left\{\hat{R}\nabla\hat{R}\right\} = 0$. This also shows (at least to some extent) that the Usadel equations are consistent with the normalization requirement.

[23] From the definition of the retarded Green's functions Eq. (9.10a) it follows that the components of $\hat{R}$ are not independent, as can also be seen from the parameterization following from the normalization.

for any matrices $\hat{M}, \hat{N}$ were used. This symmetry can be expressed as

$$\hat{R}(\mathbf{r}, -\epsilon) = \hat{R}^{\dagger}(\mathbf{r}, \epsilon). \tag{10.9a}$$

In the trigonometric parameterization Eq. (10.2a) this symmetry is transferred to the angle and phase,

$$\theta(\mathbf{r}, -\epsilon) = \theta^{*}(\mathbf{r}, \epsilon) \tag{10.9b}$$

$$\chi(\mathbf{r}, -\epsilon) = \chi^{*}(\mathbf{r}, \epsilon). \tag{10.9c}$$

10.1.1 Bulk solutions

Superconductor

For a homogeneous superconducting bulk at thermal equilibrium obeying BCS theory, the spectral quantities and the order parameter are spatially homogeneous as well, the supercurrent vanishes, $\partial_x \chi = 0$, and the order parameter can always be assumed real-valued. Hence, the spectral Usadel equation (10.7a) requires $\chi \equiv 0$, and with this the remaining one simplifies to

$$i\epsilon \sin(\theta) + \cos(\theta) = 0,$$

yielding

$$\tan\left(\theta_{\mathrm{BCS}}\right) = \frac{i}{\epsilon}. \tag{10.10}$$

This equation is solved by

$$\theta_{\mathrm{BCS}} = \begin{cases} \frac{\pi}{2} + \frac{i}{2}\ln\left(\frac{1+\epsilon}{1-\epsilon}\right) & , |\epsilon| < 1 \\ \frac{i}{2}\ln\left(\frac{\epsilon+1}{\epsilon-1}\right) & , |\epsilon| > 1 \end{cases}. \tag{10.11}$$

Plugging this expression into the parameterization for the retarded Green's function Eq. (10.2a) gives

$$\hat{R} = \frac{1}{\sqrt{\epsilon^2 - 1}} \begin{pmatrix} |\epsilon| & i\,\mathrm{sgn}(\epsilon) \\ i\,\mathrm{sgn}(\epsilon) & -|\epsilon| \end{pmatrix}. \tag{10.12}$$

This expression obviously solves the retarded component of the Eilenberger equation (9.18), which is to be expected, since the superconductor is assumed to be homogeneous in real and k-space[24] and hence in the expansion of the quasiclassical Green's function in spherical harmonics, only the s-wave component $\check{g}_s = \check{G}$ appears.

The density of states can then be obtained via Eq. (10.8) and is given by its known BCS expression

$$N_S(\epsilon) = N_0 \Theta(|\epsilon| - 1) \frac{|\epsilon|}{\sqrt{\epsilon^2 - 1}}.$$

[24] Here, the assumption of thermal equilibrium goes is.

Normal metal

Similarly, for a spatially homogeneous normal metal with $\Delta \equiv 0$ the only non-trivial spectral Usadel equation (10.7b) has the solution $\theta_N \equiv 0$, which gives for the retarded Green's function $\hat{R} = \hat{\tau}_3$. The calculation of the density of states can be used as consistency check, which yields the expected result N_0.

10.2 Kinetic Usadel equations

The Keldysh component of the Usadel equations (9.20) reads

$$\hat{R}\nabla\hat{K} + \hat{K}\nabla\hat{A} = \left[-i\epsilon\hat{\tau}_3 + \hat{\Delta}, \hat{K}\right]. \tag{10.13}$$

With the parameterization Eq. (10.2b) and the expression for the distribution matrix Eq. (10.2c) the LHS of the above equation can be written as

$$\begin{aligned}\hat{R}\nabla\hat{K} + \hat{K}\nabla\hat{A} = &\left(\hat{\tau}_0 - \hat{R}\hat{A}\right)\nabla f_L + \left(\hat{\tau}_3 - \hat{R}\hat{\tau}_3\hat{A}\right)\nabla f_T + \\ &\left(\hat{R}\nabla\hat{R} - \hat{A}\nabla\hat{A}\right) f_L + \left(\hat{R}\nabla\hat{R}\hat{\tau}_3 - \hat{\tau}_3\hat{A}\nabla\hat{A}\right) f_T\end{aligned}$$

With the identities

$$\begin{gathered}\mathrm{Tr}\left\{\left[\hat{M}, \hat{N}\right]\right\} = 0 \\ \mathrm{Tr}\left\{\hat{R}\nabla\hat{R}\right\} = \mathrm{Tr}\left\{\hat{A}\nabla\hat{A}\right\} = 0 \\ \mathrm{Tr}\left\{\hat{\tau}_3\left[\hat{\tau}_3, \hat{M}\right]\right\} = 0 \\ \nabla\left(\mathrm{Tr}\left\{\hat{R}\nabla\hat{R}\hat{\tau}_3 - \hat{\tau}_3\hat{A}\nabla\hat{A}\right\}\right) = \mathrm{Tr}\left\{\hat{\tau}_3\left[\hat{\Delta}, \hat{R} - \hat{A}\right]\right\} = 2\,\mathrm{Tr}\left\{\hat{\tau}_3\hat{\Delta}\left(\hat{R} - \hat{A}\right)\right\} \\ \mathrm{Tr}\left\{\hat{\Delta}\hat{\tau}_3\hat{M}\hat{\tau}_3\right\} = -\mathrm{Tr}\left\{\hat{\Delta}\hat{M}\right\} \\ \mathrm{Tr}\left\{\hat{R}\hat{A}\hat{\tau}_3\right\} = -\mathrm{Tr}\left\{\hat{R}\hat{\tau}_3\hat{A}\right\}\end{gathered}$$

for arbitrary matrices $\hat{M}, \hat{N}$, which partially follow from the normalization of the Green's functions $\hat{R}, \hat{A}$ or the spectral Usadel equations (10.7a)-(10.7b) and can be proved by straight forward but quite unspectacular direct calculation, one can conveniently derive equations for the distribution functions by taking the trace on both sides of Eq. (10.13) directly and after multiplication of both sides with $\hat{\tau}_3$. This approach yields the kinetic equations[25]

$$\nabla\cdot\left(\mathcal{D}_L\nabla f_L - \mathcal{T}\nabla f_T + \Pi_E f_T\right) = 0 \tag{10.14a}$$

$$\nabla\cdot\left(\mathcal{D}_T\nabla f_T + \mathcal{T}\nabla f_L + \Pi_E f_L\right) = j_{\mathrm{leak}} \tag{10.14b}$$

with the leakage current

$$j_{\mathrm{leak}} = \mathcal{R} f_T - \mathcal{L} f_L. \tag{10.15}$$

The kinetic equations represent diffusion equations for the spectral energy and charge current densities

$$\mathbf{j}_E = \mathcal{D}_L\nabla f_L - \mathcal{T}\nabla f_T + \Pi_E f_T \tag{10.16a}$$

$$\mathbf{j}_C = \mathcal{D}_T\nabla f_T + \mathcal{T}\nabla f_L + \Pi_E f_L \tag{10.16b}$$

[25] Note that the kinetic equations are written in units of Δ_{BCS} and ξ_0. In SI units an additional factor of $\hbar D$ in front of the divergences has to be included.

with the spectral coefficients

$$\mathcal{D}_L = \frac{1}{4}\mathrm{Tr}\left\{\hat{\tau}_0 - \hat{R}\hat{A}\right\} = \frac{1}{2}\left[1 + |\cos(\theta)|^2 - |\sin(\theta)|^2 \cosh(2\,\mathrm{Im}\{\chi\})\right] \tag{10.17a}$$

$$\mathcal{D}_T = \frac{1}{4}\mathrm{Tr}\left\{\hat{\tau}_0 - \hat{R}\hat{\tau}_3\hat{A}\hat{\tau}_3\right\} = \frac{1}{2}\left[1 + |\cos(\theta)|^2 + |\sin(\theta)|^2 \cosh(2\,\mathrm{Im}\{\chi\})\right] \tag{10.17b}$$

$$\Pi_E = \frac{1}{4}\mathrm{Tr}\left\{\hat{\tau}_3\left(\hat{R}\nabla\hat{R} - \hat{A}\nabla\hat{A}\right)\right\} = \mathrm{Im}\left\{\sin^2(\theta)\ \nabla\chi\right\} \tag{10.17c}$$

$$\mathcal{T} = \frac{1}{4}\mathrm{Tr}\left\{\hat{\tau}_3\hat{A}\hat{R}\right\} = \frac{1}{2}|\sin(\theta)|^2 \sinh(2\,\mathrm{Im}\{\chi\}) \tag{10.17d}$$

$$\mathcal{L} = \frac{1}{2}\mathrm{Tr}\left\{\hat{\tau}_3\hat{\Delta}\left(\hat{A} - \hat{R}\right)\right\} = -\mathrm{Re}\left\{\sin(\theta)\left(\Delta e^{-i\chi} - \Delta^* e^{i\chi}\right)\right\} \tag{10.17e}$$

$$\mathcal{R} = \frac{1}{2}\mathrm{Tr}\left\{\hat{\Delta}\left(\hat{R} + \hat{A}\right)\right\} = \mathrm{Re}\left\{\sin(\theta)\left(\Delta e^{-i\chi} + \Delta^* e^{i\chi}\right)\right\}. \tag{10.17f}$$

Here, $\mathcal{D}_L$ and $\mathcal{D}_T$ play the role of normalized energy dependent spectral diffusion coefficients for the energy (j_E) and charge (j_C) current densities, respectively. Π_E gives the density of supercurrent carrying states and $\mathcal{T}$ is a cross diffusion term. The coefficients $\mathcal{R}$ and $\mathcal{L}$ are connected to the leakage current, whereas $\mathcal{R}$ in particular is related to Andreev reflection.

The observable physical energy and charge current densities can be obtained from

$$\mathbf{J}_E = -\frac{\sigma_N}{2e^2}\int_{-\hbar\omega_D}^{\hbar\omega_D} E\mathbf{j}_E \mathrm{d}E = -\frac{\sigma_N\Delta_{\mathrm{BCS}}^2}{2e^2\xi_0}\int_{-\frac{\hbar\omega_D}{\Delta_{\mathrm{BCS}}}}^{\frac{\hbar\omega_D}{\Delta_{\mathrm{BCS}}}} \epsilon\left[\mathcal{D}_L\nabla f_L - \mathcal{T}\nabla f_T + \Pi_E f_T\right]\mathrm{d}\epsilon \tag{10.18a}$$

$$\mathbf{J}_C = \frac{\sigma_N}{2e}\int_{-\hbar\omega_D}^{\hbar\omega_D} \mathbf{j}_C \mathrm{d}E = \frac{\sigma_N\Delta_{\mathrm{BCS}}}{2e\xi_0}\int_{\frac{\hbar\omega_D}{\Delta_{\mathrm{BCS}}}}^{\frac{\hbar\omega_D}{\Delta_{\mathrm{BCS}}}} \left[\mathcal{D}_T\nabla f_T + \mathcal{T}\nabla f_L + \Pi_E f_L\right]\mathrm{d}\epsilon. \tag{10.18b}$$

Both consist of a dissipative part containing spatial derivatives of the distribution functions, and a supercurrent part.

The conservation of the physical energy current follows immediately from the conservation of the spectral one, which is ensured by Eq. (10.16a). However, according to Eq. (10.16b) the spectral charge current is not conserved, but instead the leakage current Eq. (10.15) gives rise to a source/sink term. The conservation of the physical charge current is not so obvious:[26] With the explicit definitions of $\mathcal{L}$ and $\mathcal{R}$ Eqs. (10.17e) and (10.17f) and the order parameter

[26] Even in presence of inelastic electron-phonon interaction, which can be incorporated in form of collision integrals appearing as inhomogeneities on the right hand side of the kinetic equations (10.16a)-(10.16b),the physical charge current density is conserved [204].

Eq. (10.5), the energy integral of the RHS of Eq. (10.16b) can be rewritten as

$$\int_{-\frac{\hbar\omega_D}{\Delta_{\mathrm{BCS}}}}^{\frac{\hbar\omega_D}{\Delta_{\mathrm{BCS}}}} (\mathcal{R} f_T - \mathcal{L} f_L)\mathrm{d}\epsilon = \int_{-\frac{\hbar\omega_D}{\Delta_{\mathrm{BCS}}}}^{\frac{\hbar\omega_D}{\Delta_{\mathrm{BCS}}}} \mathrm{Re}\left\{\Delta \sin(\theta)\, \mathrm{e}^{i\chi}(f_L + f_T) - \Delta^* \sin(\theta)\, \mathrm{e}^{i\chi^*}(f_L - f_T)\right\} \mathrm{d}\epsilon$$

$$= 2\,\mathrm{Re}\left\{-i\frac{|\Delta|^2}{\lambda} + i \int_0^{\frac{\hbar\omega_D}{\Delta_{\mathrm{BCS}}}} \mathrm{Im}\left\{\Delta \sin(\theta)\, \mathrm{e}^{-i\chi}\right\} (f_L + f_T)\mathrm{d}\epsilon\right\} = 0.$$

Hence, the physical charge current is indeed conserved,

$$\partial_x J_C \propto \int \partial_x j_C \mathrm{d}\epsilon = \int j_{\mathrm{leak}} \mathrm{d}\epsilon = 0,$$

and the leakage current j_{leak} leads to spectral redistribution of the spectral charge current in compliance with charge current conservation.

As already mentioned, the symmetry property Eqs. (10.9) of the spectral Usadel equations has influence on the structure of the current densities Eqs. (10.18). It follows that among the spectral coefficients Eqs. (10.17) $\mathcal{D}_L, \mathcal{D}_T$ and $\mathcal{R}$ are even functions of the energy, whereas the others are odd. Consequently, when neglecting the cross-diffusion term $\mathcal{T}$, the dissipative charge and energy currents are determined by the even (f_T) and odd (f_L) part of the distribution function, respectively, since the other part would vanish due to the energy integral. This is not unexpected, though: For a purely odd distribution function, i.e. $f_T \equiv 0$, the number of electron-like excitations with $\epsilon > 0$ equals the number of hole-like excitations with $\epsilon < 0$,[27] which results in a vanishing net current density due to the exact cancellation of both current contributions. As expected [205], the density of supercurrent carrying states, Π_E, is an odd function of energy. Furthermore, only unoccupied quasiparticle states can contribute to the supercurrent, so that one expects the charge supercurrent to be proportional to $\int \Pi_E(1-f)\mathrm{d}\epsilon$. This coincides with Eq. (10.18b) (up to a constant).

[27] The occupation of states is of course not only determined by the distribution function, but also by the DOS. The quasiclassical formulation assumes a particle-hole symmetry with an even DOS around the Fermi energy $\epsilon = 0$.

11 Mesoscopic proximity systems

When considering mesoscopic hybrid structures composed of different metals, the interplay between the compounds needs to be taken into account. Especially the mutual influence between a superconducting and a non-superconducting metal, known as superconducting proximity effect, is of importance. In addition, the Usadel equations, introduced in Sec. 9.4, which are to be applied to each compound separately, are supplemented with boundary (or rather matching) conditions for the Green's functions at the interface of the different metals.

Furthermore, the preparation of systems with dimensions small compared to the superconducting coherence length is almost no challenge anymore for modern sophisticated and elaborated manufacturing techniques. These structures allow for further simplification by deriving effective models with lower dimensions approximating the actual physical systems. This will be done for a particular experimental set-up in mind at a later point (see Sec. 12.1).

11.1 Superconducting proximity effect and Andreev reflection

The pair amplitude $F(\mathbf{r}) = \left\langle \psi_\uparrow(\mathbf{r},t)\psi_\downarrow(\mathbf{r},t)\right\rangle$[28] is the order parameter distinguishing the superconducting state with $F \neq 0$ due to the presence of Cooper pairs from the non-superconducting state $F = 0$. As other order parameters as well, it is a smooth and continuous function of space. Consequently, when bringing a superconducting metal in good metallic contact with a normal, non-superconducting one, the pair amplitude spreads into the normal metal and, in turn, is diminished in the superconductor, taking place over an energy-dependent length scale around the normal-metal–superconductor interface. This superconducting proximity effect changes the properties of the involved metals in many regards: The local density of states is altered significantly [160, 175, 206, 207], the conductance of the SN bilayer shows the reentrance effect [164, 168][29], the transition temperature is decreased [199, 209, 210], a normal metal sandwiched by two superconductors may allow a supercurrent to flow from one superconductor to the other [211], and the magnetic response changes [212, 213]. The Andreev reflection [214] is the microscopic process responsible for the superconducting proximity effect [215, 216]. It describes the charge transfer between the normal metal and superconductor and is depicted in Fig. 11.1.

An electron in the normal metal with energy E above the Fermi energy incident on the interface between the normal metal and the superconductor can enter the superconductor as Bogoliubov quasiparticle [180] only if its energy exceeds the spectral energy gap, i.e. quasiparticle states with that energy are available in the superconductor to be occupied. For smaller energies, it can only enter the superconductor together with a second electron from the normal metal having opposite momentum and spin, to form a Cooper pair and join the superconducting condensate, leaving a hole in the normal metal. Energy conservation requires that the hole excitation has the same energy as the incident electron, which means that the second electron has an energy E below the Fermi energy. Since the states $|\mathbf{k},\uparrow\rangle$ and $|-\mathbf{k},\downarrow\rangle$ are degenerated, i.e. have the same energy, the hole cannot have the same momentum as the incident electron. As a result of this non-vanishing momentum mismatch, the electron-hole pair will loose phase coherence on a length scale of $\xi_E = \sqrt{\hbar D/E}$.[30]

[28] The time-dependence entering the field operators vanishes in equilibrium and non-equilibrium steady states.

[29] See also [208] as creative approach to this topic.

[30] The phase coherence length ξ_E is limited by phase breaking processes, such as inelastic electron-electron or electron-phonon scattering and hence remains finite at the Fermi energy.

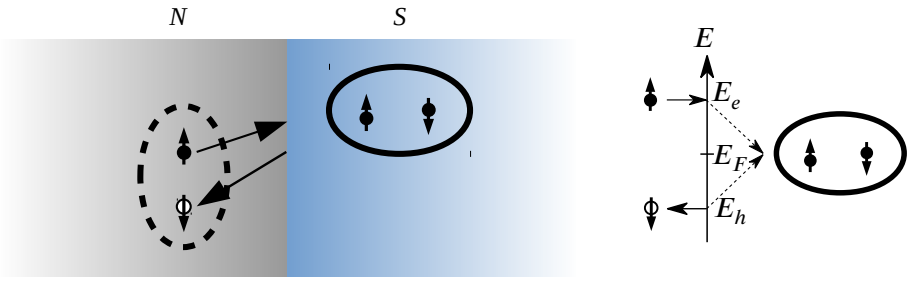

FIGURE 11.1: Depicted is the Andreev reflection of an electron in the normal metal incident on the normal-metal–superconductor interface as a hole and the formation of a Cooper pair on the superconducting side. The time-reversed process is also possible. The phase of the retro-reflected particle carries information about the phase of the incident particle and the superconducting state. Hence, Andreev reflection leads to particle-particle correlations in the normal metal.

Moreover, the superconducting proximity effect in other hybrid proximity systems is the base for various technical applications, such as superconducting spintronics using superconductors with ferromagnets [217, 218, 219], or qubits based on superconductor-semiconductor structures [220], to mention a few.

11.2 Boundary conditions

The quasiclassical approximation is valid for problems with a characteristic length much longer than the Fermi wavelength. However, in hybrid structures one must take care of the interface in order to properly take into account spatial changes in the conductance on microscopic length scales. Effective boundary conditions valid for arbitrary transmission of the interface have been derived by Zaitsev [221]. For this work the two regimes of very low transmission, occurring in tunnel junctions, and very high transmission with a clean and good metallic contact are of particular interest and will thus get special attention separately. The boundary conditions will look rather innocent, but in fact require quite some numerical effort in general, which results from the non-linearity of the Usadel equations and will be discussed in Sec. 14.

Tunnel barrier

Kuprianov and Lukichev [222] gave the Zaitsev boundary conditions in the dirty limit and for low transparency, which were further extended in Ref. [223]. Expressed in terms of Green's functions the Kuprianov-Lukichev boundary conditions read

$$\sigma_1 \check{G}_1 \frac{\partial \check{G}_1}{\partial n} = \sigma_2 \check{G}_2 \frac{\partial \check{G}_2}{\partial n} \tag{11.1a}$$

$$\sigma_2 \check{G}_2 \frac{\partial \check{G}_2}{\partial n} = \frac{1}{2R_t A} \left[\check{G}_1, \check{G}_2\right], \tag{11.1b}$$

where $\partial_n = \hat{n} \cdot \nabla$ is the derivative in direction of the interface normal $\hat{n}$ pointing from metal 1 into metal 2, σ denotes the respective conductivity, A is the cross-sectional area and R_t is the

tunnel resistance, respectively. Eq. (11.1a) describes the local conservation of the generalized current density $\sigma\check{G}\partial_n\check{G}$, which is in general not conserved by the Usadel equations (9.19).

Good metallic contact

In the case of a good metallic contact with (almost) perfect transmission, the generalized current $\sigma A\check{G}\partial_n\check{G}$ with cross-sectional area A is also conserved at the interface. In addition, the second requirement is the continuity of the Green's function across the interface,

$$\check{G}_1 = \check{G}_2. \tag{11.2a}$$

With this and the normalization of the Green's functions, $\check{G}^2 = 1$, it follows from the local conservation of the generalized current that the normal derivative of the Green's functions is also continuous across the interface,

$$\sigma_1 A_1 \frac{\partial\check{G}_1}{\partial n} = \sigma_2 A_2 \frac{\partial\check{G}_2}{\partial n} \tag{11.2b}$$

For equal cross-sectional area A, normal-state DOS N_0 and diffusion constant D the conductivities, $\sigma = e^2 N_0 D$, are equal, and the only quantity left in the Usadel equations in which the two metals can differ is the superconducting order parameter Δ. In this case their fulfillment can be forced easily: The boundary conditions are then equivalent to require continuously differentiable Green's functions. This, in turn, can be guaranteed by neglecting the interface and treating the structure as one entity for which the Usadel equations are solved, but now with a spatially discontinuous order parameter

$$\check{\Delta}(\mathbf{r}) = \begin{cases} \check{\Delta}_1 & ,\mathbf{r} \in \text{ metal 1} \\ \check{\Delta}_2 & ,\mathbf{r} \in \text{ metal 2} \end{cases}.$$

Since the Usadel equations are 2nd order differential equations, their solutions are continuously differentiable on the interior and hence in particular at the interface now belonging to the interior of the entity, even if a spatially discontinuous parameter enters the equations. Thus, all boundary conditions are fulfilled, and the solution of the Usadel equations is already determined.

Mesoscopic wire connected to a reservoir

The reservoir is treated as a macroscopic system in a spatially homogeneous state which is not affected by the presence of the mesoscopic wire it is in contact with. Instead, its retarded Green's function is given by the bulk solution, i.e. $\hat{R}_N = \tau_3$ for a normal-metal reservoir and, according to the expression for θ_{BCS} Eq. (10.11)

$$\hat{R}_S = \begin{pmatrix} \cos\left(\theta_{\mathrm{BCS}}\right) & \sin\left(\theta_{\mathrm{BCS}}\right) \mathrm{e}^{i\chi} \\ \sin\left(\theta_{\mathrm{BCS}}\right) \mathrm{e}^{-i\chi} & -\cos\left(\theta_{\mathrm{BCS}}\right) \end{pmatrix} = \frac{1}{\sqrt{\epsilon^2 - 1}} \begin{pmatrix} |\epsilon| & i\,\mathrm{sgn}\,(\epsilon)\,\mathrm{e}^{i\chi} \\ i\,\mathrm{sgn}\,(\epsilon)\,\mathrm{e}^{-i\chi} & -|\epsilon| \end{pmatrix}$$

for a superconducting one. If the superconductor in the reservoir is the only superconducting metal in the system, its phase can be set to zero, $\chi = 0$, by applying a gauge transformation.

The distribution functions of the reservoir are given by

$$f_{L/T}^{(R)} = \frac{1}{2}\left[\tanh\left(\frac{E + eV}{2k_B T}\right) \pm \tanh\left(\frac{E - eV}{2k_B T}\right)\right], \tag{11.3a}$$

where eV gives the chemical potential of the reservoir measured from a reference value. If the structure contains only one superconductor, the chemical potential of the pair condensate serves as reference value.

In the trigonometric parameterization Eq. (10.2a) and units of Δ_{BCS} and ξ_0, the boundary conditions for the superconductor simplify to

$$r\frac{\partial\theta_S}{\partial n} = \sin\left(\theta_S\right) \tag{11.3b}$$

$$\frac{\partial\chi_S}{\partial n} = 0 \tag{11.3c}$$

for the spectral quantities and

$$rD_{L/T}\frac{\partial f_{L/T}}{\partial n} = N_S\left[f_{L/T} - f_{L/T}^{(R)}\right]. \tag{11.3d}$$

Here, $r = R_t/R_{\xi_0}$ measures the tunnel resistance in units of the resistance of a one coherence length long superconductor in the normal state, $R_{\xi_0} = \xi_0/(A\sigma_S)$.

The entire charge and energy current supplied by the normal-metal reservoir is purely dissipative, which is why the respective supercurrent densities vanish at the tunnel barrier, as is described by Eq. (11.3c).[31]

Hard wall

At its surfaces the structure is typically bordered by a macroscopic insulating medium, such as a semiconducting substrate, inhibiting any unwanted tunnel current. Hence, this situation corresponds to a tunnel junction in the limit of infinite tunnel resistance. The appropriate boundary conditions are given by Eq. (11.1b) in the limit $R_t \to \infty$, which further simplify using the normalization of the Green's functions, $\check{G}^2 = \check{\tau}_0$, to

$$\frac{\partial\check{G}}{\partial n} = 0.$$

In the parameterization Eqs. (10.1), these read

$$\frac{\partial\theta}{\partial n} = \frac{\partial\chi}{\partial n} = 0$$

for the spectral quantities and

$$\frac{\partial f_L}{\partial n} = \frac{\partial f_T}{\partial n} = 0$$

for the distribution functions. From the expressions for the current densities Eqs. (10.16) it follows that the boundary conditions require the supercurrents and dissipative currents to vanish separately.

[31] In general, the boundary conditions for the distribution functions stemming from the Keldysh component describe the continuity of the quantity $\varkappa = -i\sin^2(\theta)\,\partial_n\chi$, also known as spectral supercurrent density, across the interface, among other things. As described by the spectral Usadel equations (10.7a) $\varkappa$ is conserved in a normal-metal ($\Delta = 0$). In a normal-metal reservoir, $\varkappa$ is assumed to vanish in the bulk far away from the interface, and thus everywhere. Consequently, $\varkappa$ vanishes on the superconducting side connected to the normal-metal reservoir. This is consistent with the boundary condition Eq. (11.3c).

Electrical grounding

An electrical grounding imposes boundary conditions on the distribution functions f_L and f_T by resetting them locally at the position of the grounding to their respective thermal equilibrium values given by

$$f_{L/T} = \frac{1}{2}\left[\tanh\left(\frac{E+eV}{2k_BT}\right) \pm \tanh\left(\frac{E-eV}{2k_BT}\right)\right].$$

The spectral quantities are unaffected by the electrical grounding.

12 Role of the proximity effect for normal-metal quasiparticle traps

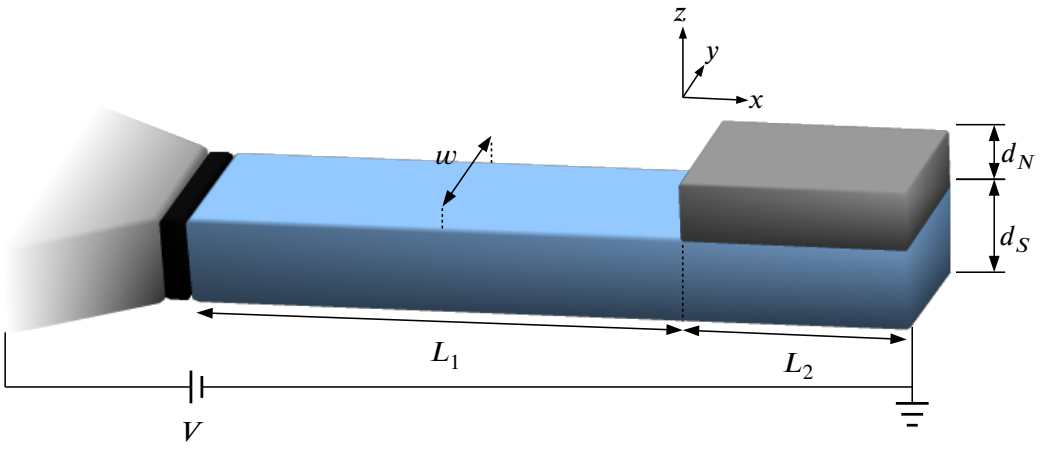

FIGURE 12.1: (Not to scale) Schematic of a QP injector with attached normal-metal trap. A mesoscopic superconducting wire (blue part) is connected to a big normal metal reservoir (partially shown by left gray part) via a thin tunnel barrier (black part). The reservoir is kept at temperature $T = 0$ K and potential eV measured from the superconductor's one. At its end the superconductor is covered in good metallic contact with another normal metal with length L_2, serving as QP trap, and is electrically grounded. In what follows, this set-up is referred to as setup 2. The trapping performance is investigated by comparing the non-equilibrium steady states of this set-up and another QP injector with the same dimensions and parameters but without attached trap. This reference set-up is called setup 1in the following. The origin $x = 0$ is located at the left edge of the QP trap. The dimensions w and d_i in the transverse directions y and z are assumed to be much smaller than the superconducting coherence length ξ_0, which allows for a one-dimensional model of the set-up.

As mentioned in Sec. 8, a QP injector composed of a normal-metal–insulator–superconductor junction which is equipped with a normal-metal trap in good metallic contact with the superconductor (see Fig. 12.1) is used to investigate on the trapping performance and the part played by the superconducting proximity effect therein. In order to determine the efficiency of the trap the non-equilibrium steady state of the S-island is compared with that of an NIS-junction with the same geometry and parameters but without a covering metal. In the following, this reference set-up will be called setup 1, whereas the set-up with normal-metal trap as is shown in Fig. 12.1 is referred to as setup 2. The Usadel equations reviewed in Sec. 10 are solved self-consistently for both set-ups and give access to the non-equilibrium steady states. At the injector, $x = -L_1$ (see Fig. 12.1 for the used coordinate system) the Kurprianov-Lukichev boundary conditions Eqs. (11.3) are applied, where the reservoir is assumed to be unaffected by the proximity effect from the mesoscopic superconductor due to the tunnel barrier, thus assuming its bulk solutions $\hat{R} = \hat{\tau}_3$. At $x = L_2$ the boundary conditions for a hard wall and electrical grounding are applied. The central quantities computed from the solutions are the superconducting order parameter, superconducting DOS, quasiparticle distribution and charge current density along the S-island. The difference among the set-ups for each quantity is put in relation to the proximity effect from the normal-metal trap in setup 2. It will be shown that the proximity effect leads to two competing characteristics affecting the trapping performance: the beneficial reduction of the DOS at an energy $|E| = \Delta_{\mathrm{BCS}}$ versus the contraction

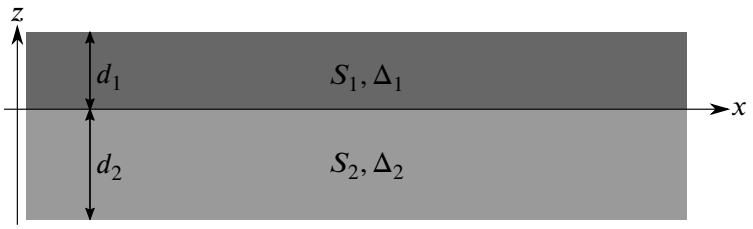

FIGURE 12.2: Overlap geometry composed of two superconducting metals $S_{1/2}$ with thickness $d_{1/2}$ and superconducting order parameter $\Delta_{1/2}$.

of the spectral energy gap causing QP poisoning. For both effects the trap position is decisive, which needs to be taken into account for optimizing the trapping performance. In addition, the conversion between dissipative normal and supercurrent inside the superconducting part with its impact on the QP density is studied.

12.1 One-dimensional model

Mesoscopic wires with transverse dimensions much smaller than the superconducting coherence length can be sufficiently treated as one-dimensional. In this section it is shown how the inhomogeneous overlap geometry shown in Fig. 12.1 due to the only partial covering by the normal-metal trap can be approximated by a one-dimensional set-up. This is done in two steps: First, a homogeneous overlap part extending in the interval $x \in [0, L_2]$ ignoring the rest is considered and one-dimensional Usadel equations for the Keldysh Green's function $\check{G}$ are derived. Essentially, they show that the overlap part behaves as a superconductor S' with an altered superconducting order parameter. In the last step, the appropriate matching conditions to apply at $x = 0$ between the uncovered S-part and the fictitious S'-part are reviewed, which are necessary due to the different transverse thicknesses.

First step: overlap geometry

Consider an infinite overlap geometry composed of two superconducting metals $S_{1/2}$ with thickness $d_{1/2}$ and superconducting order parameter $\Delta_{1/2}$, as shown in Fig. 12.2. The Green's functions $\check{G}_{1/2}$ of the two metals each obey Usadel equations with associated $\Delta_{1/2}$ and boundary conditions: At $z = \pm d_{1/2}$ the normal derivative of $\check{G}_{1/2}$ vanishes, $\partial_z \check{G}_{1/2}\big|_{z=\pm d_{1/2}} = 0$, and at $z = 0$ ones requires $\check{G}_1 = \check{G}_2$ and $\partial_z \check{G}_1 = \partial_z \check{G}_2$ [222], where ∂_z denotes the partial derivative with respect to z.
For thicknesses small compared to the superconducting coherence lengths, $d_1, d_2 \ll \xi_0 = \min\{\xi_1, \xi_2\}$ with $\xi_i = \sqrt{\hbar D/\Delta_i}$, the Green's functions can be expanded in a series in z/ξ_0. The boundary conditions are fulfilled by the expansion

$$\check{G}_{1/2}(x, z) \approx \check{G}_0(x) + \delta\check{G}(x)\left(\frac{z}{\xi_0} \pm \frac{z^2}{2d_{1/2}\xi_0}\right) \tag{12.1}$$

with two yet unknown Green's functions $\check{G}_0, \delta\check{G}$. Note that the only z-dependence of $\check{G}$ comes from the last term, i.e. $\check{G}_0$ and $\delta\check{G}$ only depend on x. The Usadel equations for the two metals can now be used to find $\check{G}$ and $\delta\check{G}$: Plugging the above series Eq. (12.1) for either $\check{G}_1$ or $\check{G}_2$ into the associated Usadel equations, neglecting all terms with a z-dependence and assuming

$\check{G}_0 - \left(d_{1(2)}/\xi_0\right)\delta\check{G} \approx \check{G}_0$ one finds for the correction

$$\hbar D\delta\check{G} = \xi_0 d_{1(2)}\check{G}_0\left\{\hbar D\frac{\partial}{\partial x}\left(\check{G}_0\frac{\partial\check{G}_0}{\partial x}\right) - \left[-iE\check{\tau}_3 + \check{\Delta}_{1(2)}, \check{G}_0\right]\right\},$$

and using this expression in the other Usadel equation one obtains 1D Usadel equations for $\check{G}_0$

$$\hbar D\frac{\partial}{\partial x}\left(\check{G}_0\frac{\partial\check{G}_0}{\partial x}\right) = \left[-iE\check{\tau}_3 + \overline{\check{\Delta}}, \check{G}_0\right] \tag{12.2}$$

with $\overline{\check{\Delta}} = \left(d_1\check{\Delta}_1 + d_2\check{\Delta}_2\right)/\left(d_1 + d_2\right)$, which is just the over the transverse direction averaged superconducting order parameter. The retarded component gives the spectral Usadel equations already obtained in Refs. [152, 158, 207].

In the case of a normal metal there is no universal length scale such as the coherence length. Instead, one can introduce the energy dependent length scale $\xi_E = \sqrt{\hbar D/|E|}$. The above derivation then requires $d_N \ll \xi_E$ for all relevant energies. This gives the energy constraint $|E| \ll \sqrt{\hbar D/d_N^2} \equiv E_{\mathrm{Th}}$ with the Thouless energy E_{Th} [224]. The relevant energies for the spectral properties and transport processes in NIS-junctions at $T = 0$ are Δ_{BCS} and $e|V|$, which are both small compared to $\hbar\omega_D$ for the present study. For $d_N \ll \xi_0$ the associated E_{Th} is comparable to $\hbar\omega_D$ and thus the above treatment of the overlap geometry is valid.

Second step: matching conditions

Now, we return to the finite overlap geometry (see Fig. 12.1) and present matching conditions at $x = 0$ for the Green's functions. How does the current density distribute transversely over the heterostructure? One might expect it to follow the path of least resistance by aggregating inside the superconductor. However, although a spatially non-continuous parameter (i.e. the superconducting order parameter) enters the exact two-dimensional Usadel equations, the distribution functions $f_{L/T}$ – and thus also the current densities – are, as solutions to a second-order differential equation, indeed continuous differentiable quantities. Consequently, in the small thickness limit, $d_1, d_2 \ll \xi_0$, with bordering hard walls, $\partial_z f = 0$, the distribution functions have nearly no transverse dependence, and thus the current densities distribute homogeneously over the transverse direction as well. As current is conserved by the exact two-dimensional kinetic Usadel equations, one has to require for the approximate one-dimensional Usadel equations

$$d_1\left.\frac{\partial f_l}{\partial x}\right|_{x=0} = \left(d_1 + d_2\right)\left.\frac{\partial f_r}{\partial x}\right|_{x=0}, \tag{12.3}$$

in addition to the usual continuity $f_l = f_r$ at $x = 0$. The subscripts l/r refer to "left" and "right" with respect to the contact at $x = 0$, where the two metals with different thickness meet.

There is no conserved quantity for the spectral Usadel equations in general. [32] In order to reduce the number of variables in a system, one usually averages the Green's functions $\check{G}(\mathbf{r})$ over the silent directions the Green's functions do not depend on. Consequently, at

[32] In a superconductor the spectral supercurrent density $j_E = \mathrm{Tr}\left\{\hat{\tau}_3\hat{R}\nabla\hat{R}\right\}$ (which is not be confused with the energy current density also denoted by j_E) is not conserved in general.

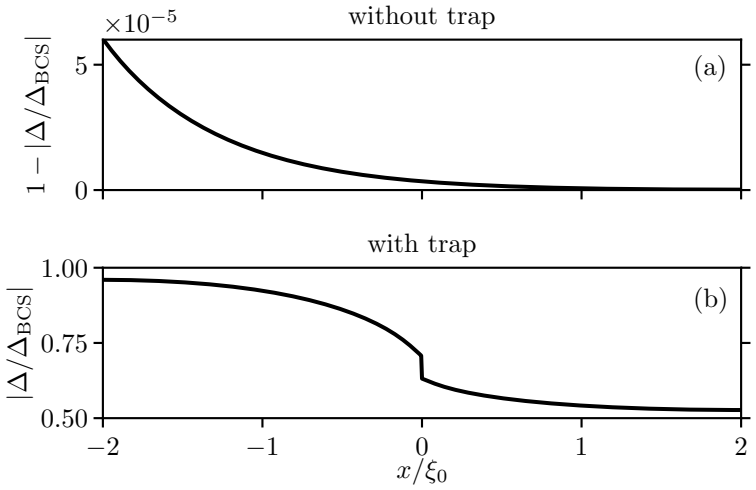

FIGURE 12.3: Spatial profile of the superconducting order parameter along the superconductor, computed for $eV = 0$. For setup 1 (top panel (a)) the inverse proximity effect of the normal-metal reservoir on the superconductor is almost negligible due to the tunnel barrier, hence the order parameter only slightly deviates from the bulk value. The good metallic contact of the normal metal in setup 2 (bottom panel (b)) leads to a halving of the order parameter (for $d_S = d_N$) of the underlying superconducting part, which also influences the rest of the superconductor. Note that at the injector with a distance of $L_1 = 2$ to the normal-metal trap, the superconducting order parameter recovers to over 95 % of its bulk value.

locations where metals with different cross-sectional area are in contact, the so defined new Green's functions are not continuous differentiable. To see that, consider e.g. the present set-up Fig. 12.1:

$$\left.\frac{\partial \check{G}_l}{\partial x}\right|_{x=0} = \frac{1}{d_1}\int_0^{d_1} \left.\frac{\partial \check{G}}{\partial x}\right|_{x=0} \mathrm{d}z \tag{12.4}$$

$$\left.\frac{\partial \check{G}_r}{\partial x}\right|_{x=0} = \frac{1}{d_1+d_2}\left[\int_0^{d_1} \left.\frac{\partial \check{G}}{\partial x}\right|_{x=0} \mathrm{d}z + \int_{d_1}^{d_2} \underbrace{\left.\frac{\partial \check{G}}{\partial x}\right|_{x=0}}_{=0} \mathrm{d}z\right] \tag{12.5}$$

$$\Rightarrow d_1 \left.\frac{\partial \check{G}_l}{\partial x}\right|_{x=0} = \left(d_1+d_2\right) \left.\frac{\partial \check{G}_r}{\partial x}\right|_{x=0}, \tag{12.6}$$

where the last integral in the second line vanishes due to the hard-wall boundary condition. Together with the usual continuity $\check{G}_l = \check{G}_r$ at $x = 0$ the matching conditions Eq. (12.6) describe the local conservation law of the spectral current $\check{G}\partial_x\check{G}$. They can be generalized taking into account arbitrary cross-sectional areas and conductivities for the two metals in contact [222]. Furthermore, the Keldysh components of Eq. (12.6) imply the matching conditions Eq. (12.3) for the distribution functions.

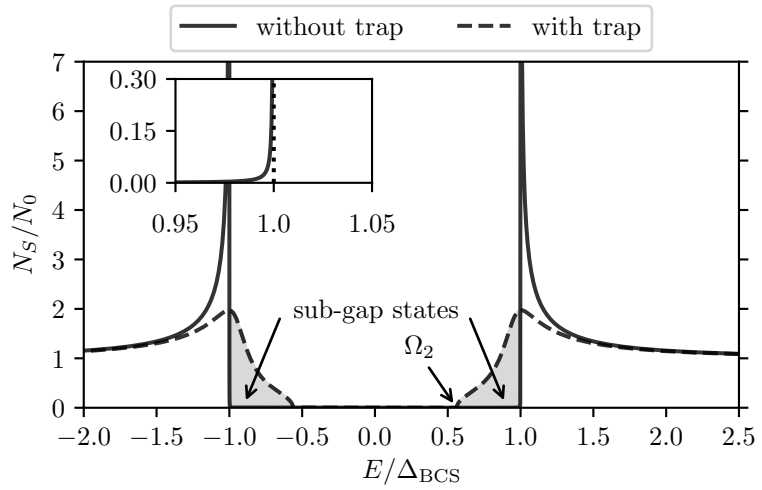

FIGURE 12.4: Comparison of the superconducting DOS at the QP injector ($x = -L_1$) for setup 2 (dashed line) and setup 1 (solid line), computed for $eV = 0$. The respective deviations from the BCS bulk DOS (dotted line, almost entirely covered by solid line) result from the proximity effect. There, the influence of the normal-metal reservoir is again almost negligible due to the tunnel barrier (see inset). For setup 2, the proximity effect from the normal-metal trap results in a significant reduction of the spectral energy gap to a value $\Omega_2 \approx 0.56\Delta_{\mathrm{BCS}}$, accompanied by a reduction of the BCS peak at an energy $|E| = \Delta_{\mathrm{BCS}}$, while the superconducting order parameter Δ almost recovers its BCS bulk value (see Fig. 12.3 (b)). The sub-gap states, depicted by the grey-shaded areas, with energies $|E| < \Delta_{\mathrm{BCS}}$, for which the bulk DOS vanishes, are additionally available for occupation.

12.2 Numerical results

If not mentioned otherwise the used parameters are $L_1 = L_2 = 2\xi_0$ for both set-ups, and $d_N = d_S \ll \xi_0$ for setup 2.

Order parameter

For setup 1, the inverse proximity effect from the normal-metal reservoir only leads to a slight spatial modification of the superconducting order parameter, as seen in Fig. 12.3 (a).

Fig. 12.3 (b) shows the great impact of the proximity effect of the normal-metal trap on the superconductor: It reduces the order parameter of the underlying superconductor to a bulk value of $d_S\Delta_{\mathrm{BCS}}/(d_S + d_N)$, which, in turn, leads to a reduction of the order parameter of the uncovered superconducting part. Their mutual adjustment leads to a stronger bending on the uncovered site, since the SN bilayer has a greater thickness of $d_S + d_N$. Moreover, the discontinuity at $x = 0$ in the superconducting order parameter and the electron pairing interaction strength λ is such that the pairing amplitude $F = \lambda\Delta$ is continuous.

Furthermore, for both set-ups a dependence on the applied voltage, due to QP injection or formation of a supercurrent, is hardly discernible, which is in accordance with numerical results showing that $n_{\mathrm{qp}}/(N_0\Delta_{\mathrm{BCS}}) \ll 1$ and $J_S/J_{\mathrm{crit}} \ll 1$ with the critical supercurrent density $J_{\mathrm{crit}} \approx \frac{3}{4}\Delta_{\mathrm{BCS}}\sigma_N/(e\xi_0)$ [161] (see Fig. 12.7 and Fig. 12.9 below).

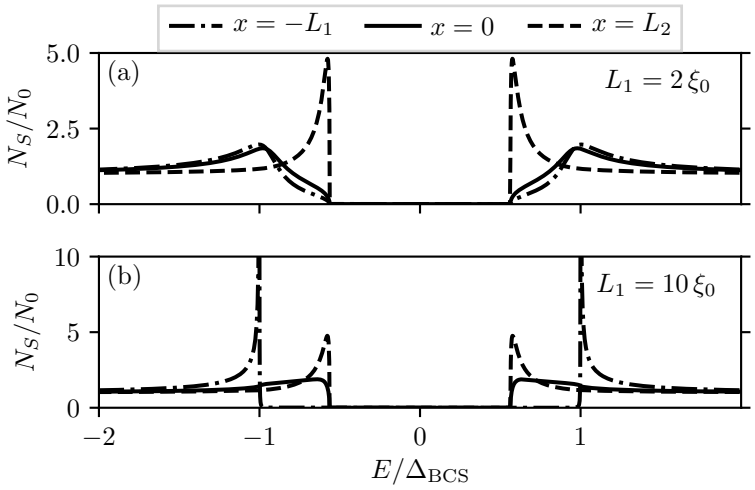

FIGURE 12.5: Superconducting DOS at the QP injector (dashdotted line), side of the trap facing the injector (solid) and electrical grounding (dashed line) for a distance of $L_1 = 2\xi_0$ (top panel (a)) and $L_1 = 10\xi_0$ (bottom panel (b)) between the QP injector and the normal-metal trap (see Fig. 12.1 for set-up details), computed for $eV = 0$. The DOS approaches the BCS bulk behavior with increasing distance from the trap, hence losing the striking features of setup 2 with $L_1 = 2\xi_0$ (see Fig. 12.4), which are thus caused by the proximity effect from the normal-metal trap.

Density of states

Within the Usadel formalism, the QP DOS can be computed from the retarded Green's function via

$$N_S(x, E) = \frac{N_0}{2}\mathrm{Re}\left\{\mathrm{Tr}\left\{\hat{R}(x, E)\hat{\tau}_3\right\}\right\} = N_0\mathrm{Re}\left\{\cos\left(\theta(x, E)\right)\right\}.$$

Fig. 12.4 shows the superconducting DOS for both set-ups at the QP injector. For setup 1 (dashed line) the DOS almost coincides with that of a BCS bulk superconductor (dotted line). The inverse proximity effect from the normal-metal reservoir on the superconductor is strongly suppressed due to the tunnel barrier and only leads to a slight broadening of the BCS energy gap with a small but non-vanishing DOS for energies $|E| \leq \Delta_{\mathrm{BCS}}$, revealing the existence of sub-gap states, i.e. states with energy $|E| < \Delta_{\mathrm{BCS}}$ for which the BCS DOS vanishes (see inset of Fig. 12.4).

For setup 2 the pronounced reduction of the spectral energy gap Ω_2 in the DOS with a significant increase in the number of sub-gap states and the reduction of the peak at $|E| = \Delta_{\mathrm{BCS}}$ are most salient. As Fig. 12.5 illustrates, this is traced back to the close proximity of the normal-metal trap ($L_1 = 2\xi_0$ for top panel (a)) with a distance of $L_1 = 2\xi_0$, as these features almost recover their BCS bulk behavior for $L_1 = 10\xi_0$ (see bottom panel (b)). Note that this in contrast to the superconducting order parameter, which almost recovers its BCS bulk value at the injector for $L_1 = 2\xi_0$ (see Fig. 12.3). Such discrepancy between the spectral energy gap Ω in the DOS and the absolute value of the order parameter $|\Delta|$ are known from gapless superconductivity, which can occur in both equilibrium and non-equilibrium situations[33] and

[33] See, for example [179, 180, 225] and references therein.

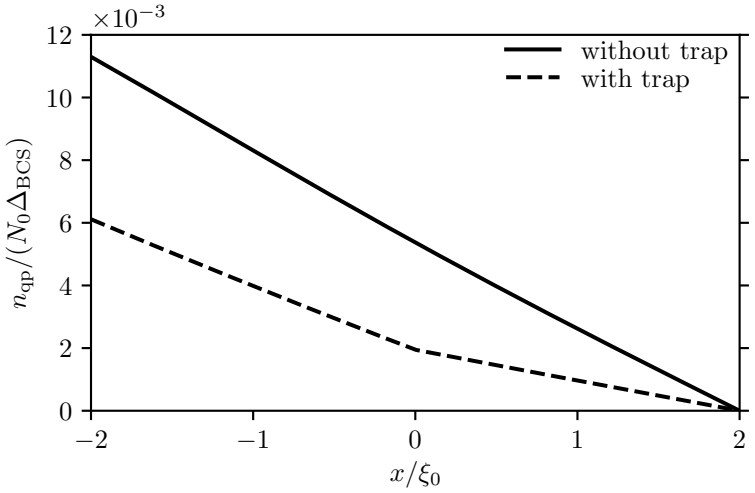

FIGURE 12.6: Comparison of the QP density along the superconductor with (solid line) and without (dashed line) trap for a voltage $e|V| = 10\Delta_{\mathrm{BCS}}$. With attached trap the QP density is reduced throughout the superconductor. For setup 1, the superconductor is almost homogeneous due to the negligible proximity effect, and therefore the diffusion of the QPs through the superconductor result in a linear curve, in accordance with the approximate solutions given in Sec. 14.3. The kink in the dashed line for setup 2 results from the changing thicknesses at $x = 0$ (see Fig. 12.1), entering via the effective matching conditions Eq. (12.6).

in hybrid structures in thermal equilibrium with striking agreement between experiment and theory based on the Usadel formalism [226].

See Fig. 12.5 (a) for the DOS at different positions within the superconductor.

Quasiparticle injection

The density of populated QP states $n_{\mathrm{qp}} = n_h + n_e$ has contributions

$$n_h(x) = \int_{-\hbar\omega_D}^{0} N_S(x,E) f_h(x,E) \mathrm{d}E$$

from hole-like excitations with $E < 0$ and

$$n_e(x) = \int_{0}^{\hbar\omega_D} N_S(x,E) f_e(x,E) \mathrm{d}E$$

from electron-like excitations with $E > 0$. Using the particle-hole symmetry $N_S(-E) = N_S(E)$ and $f_h(-E) = f_e(E)$, the total density of QPs can be written as

$$n_{\mathrm{qp}}(x) = \int_{0}^{\hbar\omega_D} N_S(x,E) \left[1 - f_L(x,E) - f_T(x,E)\right] \mathrm{d}E. \tag{12.7}$$

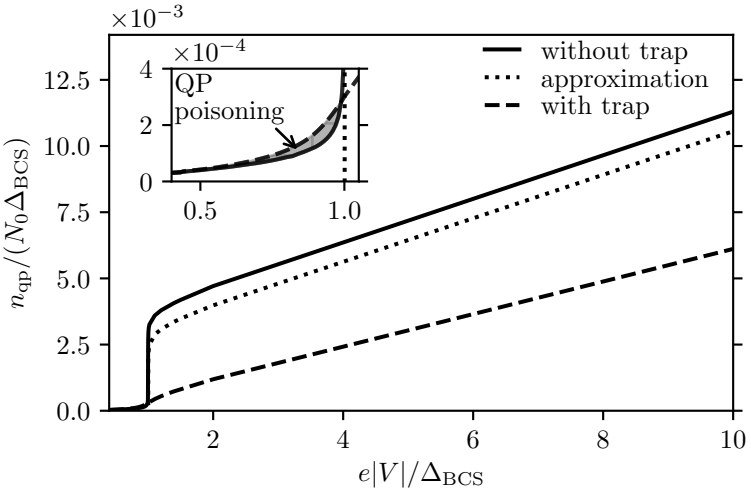

FIGURE 12.7: QP density at the injector as function of applied voltage with (dashed line) and without (solid line) trap. The two striking features of the DOS for setup 2 (see Fig. 12.4), caused by the proximity effect, influence the efficiency of the trap competitively: While the reduction of the DOS at an energy $|E| = \Delta_{\mathrm{BCS}}$ leads to the strongly reduced QP density at an injection voltage $e|V| = \Delta_{\mathrm{BCS}}$, the new available sub-gap states lead to QP poisoning, i.e. their occupation at lower voltages. The off-set between the parallel linear curves at higher voltages is explained below by the conversion between dissipative normal and supercurrent.

At the grounding, the distribution functions recover their zero-temperature equilibrium values, $f_L(E) = \mathrm{sgn}(E)$, $f_T(E) = 0$, so that the QPs are forced to vanish there, $n_{\mathrm{qp}}(x = L_2) = 0$. Fig. 12.6 shows the spatial profile of the QP density $n_{\mathrm{qp}}(x)$ along the superconductor for an applied voltage of $e|V| = 10\Delta_{\mathrm{BCS}}$. The trap leads to a reduction of the QP density throughout the superconductor. For setup 1 the proximity effect is strongly suppressed. Consequently, the superconductor is almost homogeneous, the spectral coefficients that enter the kinetic Usadel equations (10.16a)-(10.16b) are spatially independent, and the diffusion of the QPs through the superconductor leads to a linear change in the QP density. The approximate solutions, which assume a homogeneous superconductor and are given in the appendix, are in good agreement with the numerical results.

The presence of the sub-gap states in the DOS Fig. 12.4 makes a QP injection possible for voltages $e|V| < \Delta_{\mathrm{BCS}}$ (see Fig. 12.7).

Trapping performance

The trapping performance can be demonstrated and quantified by a direct comparison of the density of injected QPs for both set-ups, see Fig. 12.7: At a voltage $e|V|$ slightly above Δ_{BCS}, the QP density for setup 1 is bigger than that for setup 2 by a factor of approximately 7.6. This is due to the inverse proximity effect, which leads to a significant reduction in the DOS at $|E| = \Delta_{\mathrm{BCS}}$[34] (see Fig. 12.4). However, since the total number of available states is not

[34]The QP density is not only controlled by the DOS, but also by the QP distribution function. The distribution function shows a step-like behaviour, where the width of the middle-step coincides with the according gap in the DOS, so that the departure from the equilibrium distribution does not manifest itself. The agreement of the numerical results for the the QP and current density with that given in [180], which assume an equilibrium distribution, support this finding.

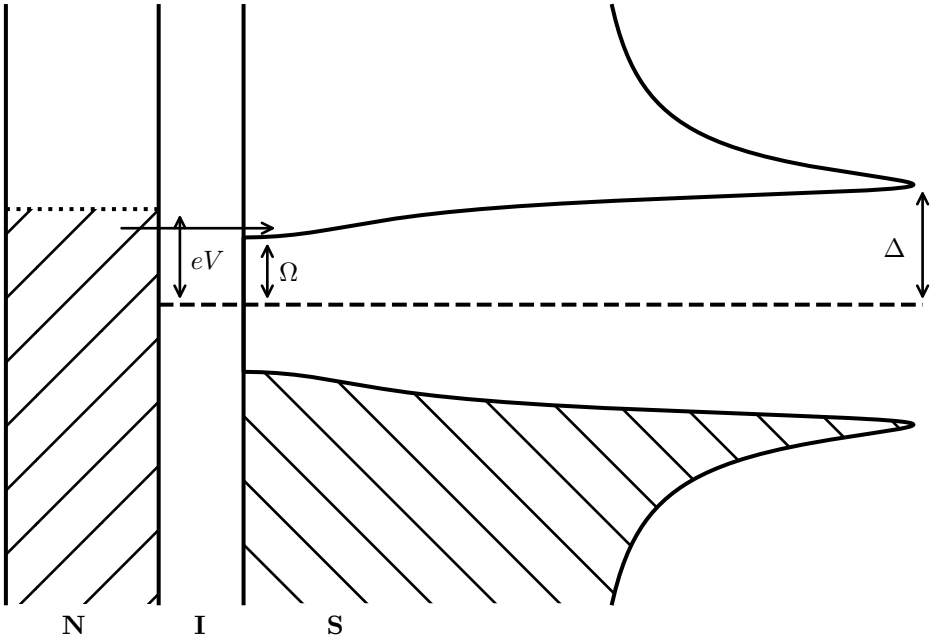

FIGURE 12.8: In the semiconductor model [180] the superconductor is represented as a semiconductor with a band gap of $2\,\Omega$ and its chemical potential right between the valence and conduction band. As usual, at $T = 0$ K all states up to the respective chemical potentials of the superconductor and normal metal are occupied, depicted by the hatched area, respectively. The difference between the chemical potentials gives rise to a voltage V between the two metals. Electrons in the normal metal with energy $\Omega < E < eV$ can tunnel through the tunnel barrier and enter the superconductor, hence contributing to quasiparticle and current injection.

altered by the (inverse) proximity effect,

$$\int_{-\hbar\omega_D}^{\hbar\omega_D} \left(N_S - N_0\right) \mathrm{d}E = 0,$$

the reduction of the $|E| = \Delta_{\mathrm{BCS}}$ peak is accompanied by a softening of the spectral energy gap down to $\Omega \approx 0.56\Delta_{\mathrm{BCS}}$ with the existence of the sub-gap states. This feature is pronounced much more significantly for setup 2, which leads to QP poisoning for voltages $e|V| < \Delta_{\mathrm{BCS}}$, i.e. higher QP densities. Note, however, that the ratio of QP densities for setup 2 and setup 1 is not higher than approximately 1.4, even though the DOS differ significantly from each other for energies $|E| < \Delta_{\mathrm{BCS}}$. The location of the trap plays a decisive role in the trapping performance as the superconducting DOS recovers its bulk-form with increasing distance to the trap. Consequently, in the limit $L_1 \gg \xi_0$ the trap does not have an impact on the injection and density of the QPs. The opposite limit $L_1 = 0$ is equivalent to setup 1 but with the superconductor S replaced by S' with half the initial spectral energy gap. The resulting injection curve $n_{\mathrm{qp}}(V)$ at the injector is obtained from the solid line in Fig. 12.7 horizontally shifted by 0.5 units, indicating a QP poisoning for all voltages. These two limits clearly show the existence of a trap position with optimal trapping performance.

The integrand in Eq. (12.7) is almost independent of the applied voltage (apart from the fact

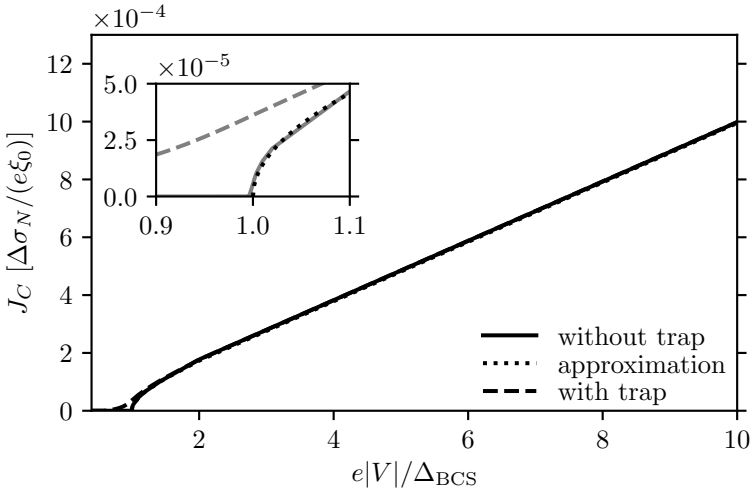

FIGURE 12.9: Current-voltage characteristics for the set-up with (dashed line) and without (solid line) normal-metal trap. The dotted line in the inset shows the theoretically predicted $I - V$ curve in the diffusive limit with neglected proximity effect. The deviations from this curve for the present set-ups are due to the sub-gap states, which are occupied and contribute to the charge current for voltages $e|V| < \Delta_{\mathrm{BCS}}$.

that $f(|E| > e|V|) = 0$), and almost equal for both set-ups at high energies $|E| \gg \Delta_{\mathrm{BCS}}$. This, together with the finding that the integrand is strongly peaked at $|E| = \Delta_{\mathrm{BCS}}$ due to the DOS for setup 1, explains why both curves are almost parallel with an offset of approximately $5.2 \times 10^{-3} N_0 \Delta_{\mathrm{BCS}}$ for voltages $e|V| \gtrsim 2\Delta_{\mathrm{BCS}}$. This offset depends on the set-up geometries and tends to zero in the limit $L_1 \gg \xi_0$. Below, we will qualitatively explain the appearance of this offset via the conversion between normal and supercurrent.

Current conversion

The Usadel formalism allows for a spectral resolution of the physical charge and energy current densities, J, in terms of their respective spectral ones, $\mathbf{j}$:

$$J_C = \frac{\sigma_N}{e} \int_0^{\hbar\omega_D} j_C \mathrm{d}E \tag{12.8}$$

$$J_E = -\frac{\sigma_N}{e^2} \int_0^{\hbar\omega_D} E j_E \mathrm{d}E \tag{12.9}$$

with the normal-state conductivity $\sigma_N = e^2 N_0 D$ of the metal and the current densities given in Eq. (10.16a)-(10.16b). The dissipative part is proportional to the gradient of the distribution functions, whereas the last term accounts for the supercurrent, respectively.

The current-voltage characteristics of both set-ups are shown in Fig. 12.9.

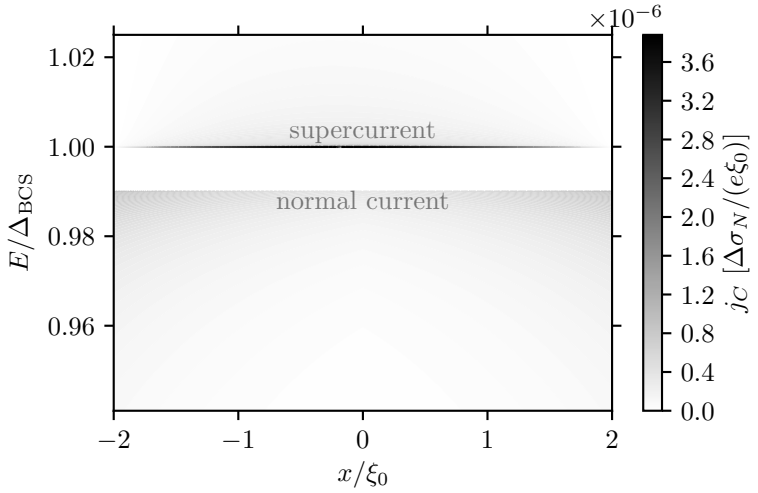

FIGURE 12.10: Spectrally resolved charge current with contributions to the dissipative normal current and supercurrent as a function of position (horizontal axis) and energy (vertical axis) at a voltage $e|V| = 0.99\Delta_{\mathrm{BCS}}$ just below the spectral energy gap for setup 1.

Fig. 12.10 shows a contour plot of the spectral charge current j_C along the superconductor without normal-metal trap in the relevant energy interval for an applied voltage of $e|V| = 0.99\Delta_{\mathrm{BCS}}$. The sub-gap states present in the DOS Fig. 12.4 make a QP injection and a current flow possible for voltages $e|V| < \Delta_{\mathrm{BCS}}$. The energies of QPs entering the superconductor and thus the spectral contributions to the normal current are bounded by $e|V|$, whereas the states with energies $|E| \gtrsim \Delta_{\mathrm{BCS}}$ contribute to the supercurrent, most significantly at the peak of the DOS (see Fig. 12.4) and regardless of the applied voltage. Note that these two contributions overlap for voltages $e|V| \gtrsim \Delta_{\mathrm{BCS}}$.

From Eq. (10.16b) it is evident, that the spectral charge current is not conserved in a superconductor. Instead, the leakage current leads to its spectral redistribution. This process is visualized in Fig. 12.11: According to Fig. 12.10, the charge current entering the superconductor at the injector is entirely made out of dissipative normal current. While passing through the superconductor, the spectral charge current gets shared among states with energies $|E| \leq e|V|$ and $|E| \approx \Delta_{\mathrm{BCS}}$ indicated by the blue ($j_{\mathrm{leak}} < 0$) and red ($j_{\mathrm{leak}} > 0$) areas. This manifests itself in an increase of the supercurrent and a decrease of the normal current (see also Fig. 12.10), respectively, indicated by the varying transparency of the associated arrows. This conversion happens on a length scale of about $2\,\xi_0$, after which the whole process is almost reversed.[35] Note, however, that the current conversion takes place in a normal metal as well, which therefore cannot be determined solely by the leakage current, since it vanishes in a normal metal due to $\Delta = 0$.

The purely normal charge current entering the superconductor,

$$J_C = \frac{\sigma_N}{e} \int_0^{e|V|} \left(\mathcal{D}_T \frac{\partial f_T}{\partial x} + \mathcal{T} \frac{\partial f_L}{\partial x} \right) \Bigg|_{x=-L_1} \mathrm{d}E,$$

is carried by states with an energy up to $e|V|$. The lower boundary in the above integral must be effectively replaced by the spectral energy gap in the DOS, as (almost) no states are

[35] Note the lack of symmetry around $x = 0$, which is due to the unsymmetrical boundary conditions.

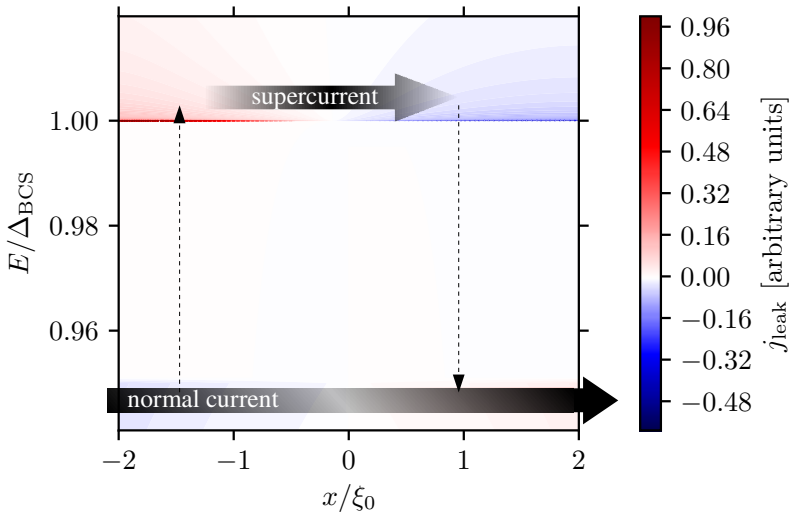

FIGURE 12.11: Contour plot of the leakage current without normal-metal trap at a voltage $e|V| = 0.95\Delta_{\mathrm{BCS}}$. Shown is the spectral redistribution of the charge current density (see Fig. 12.10) in the relevant energy interval and the partial conversion between normal and supercurrent along the superconductor. The transparency level of the arrows indicate the amount of the respective current to the total charge current (see Fig. 12.10).

available for occupation below it.

The conversion between normal and supercurrent is due to Andreev reflection [214] of states with energy $|E| < |\Delta|$ described by $\mathcal{R}$. Note that the spectral energy gap Ω in the DOS might differ from Δ, as it is the case for setup 2. For setup 1 with a negligible proximity effect, $\mathcal{R}$ almost attains its BCS bulk value and thus vanishes for energies $|E| \gtrsim \Delta_{\mathrm{BCS}}$. But even for setup 2 with a non-negligible impact of the proximity effect, the order parameter has a magnitude close to unity at the injector and decreases monotonically throughout the superconductor (see Fig. 12.3 (a)). The spectral energy gap Ω is significantly reduced and the DOS is clearly non-vanishing for states with energy $|E| > \Omega$ due to the proximity effect, so that these new states contribute to the charge current (see Fig. 12.8 for an illustration). Since $\mathcal{R}$ is non-vanishing for these energies, the associated states get Andreev reflected and thus contribute to the supercurrent. This explains why the conversion from normal to supercurrent is so pour for setup 1 compared to setup 2 for voltages $e|V| > \Delta_{\mathrm{BCS}}$ (see Fig. 12.12). For voltages $e|V| < \Delta_{\mathrm{BCS}}$ all occupied states get Andreev reflected and thus contribute to supercurrent, giving rise to the sudden jump at $e|V| = \Delta_{\mathrm{BCS}}$. This conversion process is not local, but instead takes place over a length of about $2\xi_0$. In addition, the grounding at $x = L_2$ forces an entire reconversion from super- to normal current, so that both set-ups with a total length $L_S = L_1 + L_2 = 4\xi_0$ of the superconductor each are too short for a pronounced conversion close to unity. This might also explain why the conversion for setup 1 is higher than for setup 2 for voltages $e|V| < \Delta_{\mathrm{BCS}}$. This could be resolved by increasing the length of the superconducting part, leading to a decline in conversion for voltages $e|V| > \Delta_{\mathrm{BCS}}$.

Andreev reflection and QP reduction

The mutual conversion between normal and supercurrent via Andreev reflection [227] affects the QP density: The dissipative normal current is due to a diffusive motion of the QPs and is thus almost proportional to the gradient of their density, $\boldsymbol{J}_N \propto \nabla n_{\mathrm{qp}}$. Consequently, the more normal current is converted into supercurrent along the superconductor, the more

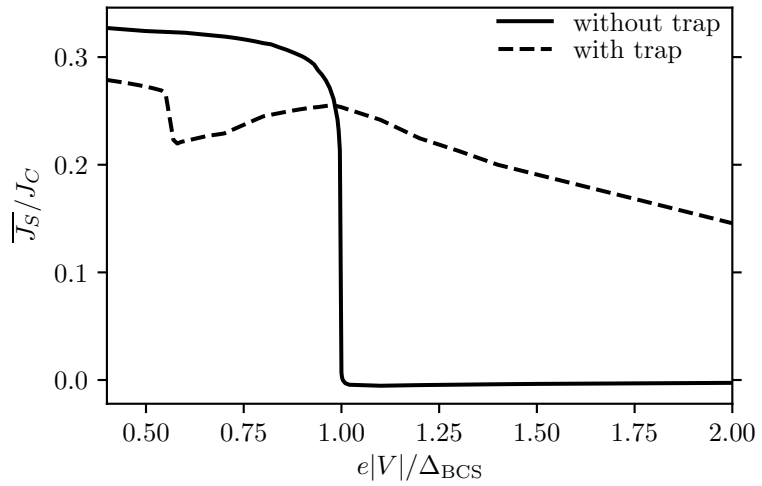

FIGURE 12.12: Supercurrent density averaged along the superconductor and normalized to the total charge current density as a function of applied voltage for setup 2 (dashed line) and setup 1 (solid line). The conversion between dissipative normal current and supercurrent is due to Andreev reflection of states with energy $|E| \leq |\Delta|$, which takes place over a length $\sim 2\xi_0$. This, and the amount of sub-gap states, i.e. the discrepancy of the spectral energy gap Ω in the DOS and $|\Delta|$, explain the different ratios of conversion into supercurrent.

the QP density gradient decreases. A pronounced conversion, combined with the electrical grounding draining the QPs $n_{\mathrm{qp}} = 0$, leads to a reduction of the QP density throughout the whole superconductor.

This rather qualitative view can be made more quantitative: Integrating $\partial_x n_{\mathrm{qp}} = \alpha J_N = \alpha(J_C - J_S)$ with a phenomenological proportionality factor α along the superconductor yields for the QP density at the injector $n_{\mathrm{qp}}(x = -L_1) = \alpha L \left(J_C - \overline{J_S}\right)$, where $\overline{J_S}$ denotes the supercurrent averaged along the superconductor and it was used that $n(x = L_2) = 0$ due to the electrical grounding. From the numerical solutions for high voltages $e|V| \gg \Delta_{\mathrm{BCS}}$ the factor α is found to be approximately $\alpha^{(1)} \approx 2.83$ for setup 1 and $\alpha^{(2)} \approx 2.21$ for setup 2. Neglecting the supercurrent for setup 1 and using $J_C^{(1)} = J_C^{(2)} \equiv J_C$, the difference in the QP density $\Delta n = \left(n_{\mathrm{qp}}^{(1)} - n_{\mathrm{qp}}^{(2)}\right)\Big|_{x=-L_1}$ at the injector is given by

$$\Delta n = \left(1 - \frac{\alpha^{(2)}}{\alpha^{(1)}}\right) n_{\mathrm{qp}}^{(1)}\Big|_{x=-L_1} + \alpha^{(2)} L_S \overline{J_S}^{(2)},$$

where the QP densities, length of the superconductor and supercurrent density are measured in units of $N_0\Delta_{\mathrm{BCS}}$, ξ_0 and $\Delta_{\mathrm{BCS}}\sigma_N/(e\xi_0)$, respectively. Plugging in all numerically determined values, Δn acquires a value of approximately 4.8×10^{-3} for high voltages. This is in good agreement with the offset of 5.2×10^{-3} in Fig. 12.7.

13 Conclusion

Normal-metal QP traps can improve the performance of superconducting devices. The superconducting proximity effect takes a central role in the evacuation process of non-equilibrium

QPs. When attaching such a QP trap in close proximity to an NIS-junction, the main effects of the inverse proximity effect are a significant reduction of both the spectral gap Ω in the DOS and the $|E| = \Delta_{\mathrm{BCS}}$ peak in the superconducting DOS. While the trapping performance arises from the latter effect, the former leads to QP poisoning due to the occupation of the new available states $\Omega < |E| < \Delta_{\mathrm{BCS}}$. Due to Andreev reflection, which still occurs up to energies $|\Delta|$, these states contribute to the conversion from normal to supercurrent along the superconductor, which qualitatively explains the numerically observed reduction of the QP density for high injection voltages in presence of a trap. These effects need to be taken into account for finding the optimal trap position and optimizing the trapping performance. This is subject to further investigation.

14 Numerical solution of the Usadel equations

14.1 Relaxation method and difficulties

In structures of finite size, the Usadel equations are supplemented by one boundary condition at each outer end, and further matching conditions between different compounds of the structure. Here, the arising boundary value problem (BVP) is solved numerically using Python. Existing libraries with included solvers for BVPs are available, such as scipy's bvp_solver for first order ordinary differential equations.[36] Typically, a non-linear ordinary differential equation (ODE) is solved using a relaxation method [228], which discretizes the ODE, thereby transforming it into a non-linear algebraic equation $F(u) = 0$ for the vector u storing the values of the wanted quantity on the mesh points. The algebraic equation, in turn, can be solved using a Newton iteration scheme: Starting with a given initial guess for the solution to the BVP on the mesh grid, u_0[37], the approximate solution is improved iteratively by introducing small deviations, $u_k = u_{k-1} + \delta u$, determined via

$$F(u_k) \approx F(u_{k-1}) + J(u_{k-1})\delta u \stackrel{!}{=} 0,$$

which is a linearized version for the deviation δu of the non-linear problem with the the Jacobian J of F with respect to u. This iteration is terminated if the deviations between two successive iterations $\delta u = u_k - u_{k-1}$ and $F(u_k)$ are both smaller than pre-specified tolerances.

However, as already mentioned, the matching conditions between two compounds of the structure complicate the numerical solution. As example, consider a one-dimensional SN structure with mesoscopic superconducting and normal metal part both of finite length, which are in good metallic contact and with hard-wall boundary conditions on the outer ends. The appropriate matching conditions require $\check{G}$ and $\sigma A \partial_x \check{G}$ to be continuous across the interface, which shall be located at $x = 0$. This problem can be solved by choosing (or guessing) a value for $\check{G}(x = 0)$, and solving the Usadel equations using the relaxation method described above on the S-part and N-part separately with the chosen $\check{G}(x = 0)$ as boundary condition on each part. The first matching condition, $\check{G}_S(x = 0) = \check{G}_N(x = 0)$, is thus fulfilled by construction. However, since $\check{G}_S$ and $\check{G}_N$ depend on $\check{G}(x = 0)$, the second matching condition will in general not be fulfilled right away, and furthermore, since the Usadel equations are non-linear, it is not possible to construct a solution fulfilling both matching conditions from a linear combination of two solutions $\check{G}^{(1)}_{S/N}, \check{G}^{(2)}_{S/N}$ to different values of $\check{G}^{(1)}(x = 0), \check{G}^{(2)}(x = 0)$.[38] Therefore, a Newton iteration-like approach is necessary to fulfill both matching conditions simultaneously. Given that not only the numerical solution of the Usadel equations is based on an iteration, but the solution of the self-consistency equation as well, the total run time is impractical and unacceptable in many cases. This is the main reason why to implement an own numerical solver, which is described in some detail below.[39]

[36] As is discussed in Sec. 12.1 two dimensions of the set-ups present in this work can be neglected, degrading the Usadel equations from partial to ordinary differential equations. The derivation of equivalent first order differential equations is achieved in the usual manner: The second order differential equation is promoted to a system of two coupled first order differential equations.

[37] An analytic approximate solution for the Usadel equations can be computed rather conveniently, as will be seen in Sec. 14.3.

[38] This only works for the kinetic Usadel equations (10.14) since they are linear in the distribution functions.

[39] Note, however, that there was no attempt done to improve the initial guess for the matching condition, which probably would have reduced the run time. Frankly speaking, the decision towards an own solver was not insignificantly driven by curiosity as well.

14.2 Details about used solver

The solver written for this work is partially based on the relaxation method mentioned above. The structure is spatially divided into a mesh with equidistant grid points with spacing $h = 0.01$. The differential operators[40] appearing in the spectral and kinetic Usadel equations (10.7) and (10.14), respectively, and applied boundary and matching conditions are written as finite differences with an accuracy up to second order $\mathcal{O}(h^2)$. In doing so and linearizing the spectral Usadel equations around the small deviations, the BVP is transformed into a linear system of equations for the deviations with a sparse coefficient matrix, which is solved using the spsolve routine contained in the scipy.sparse.linalg package. Note that any matching condition is, as part of the linear system, represented as linear equation as well and hence does not need any iterative approach to be solved. The error and convergence tolerance for the spectral Usadel equation is set to $\varepsilon_{\mathrm{err}} = 10^{-9}$ and $\varepsilon_{\mathrm{con}} = 10^{-11}$, respectively. The number of iterations needed to get below these thresholds,

$$||F(u_k)|| < \varepsilon_{\mathrm{err}} \quad \wedge \quad ||\delta u|| < \varepsilon_{\mathrm{con}},$$

where $||\bullet|| = \max_{x_i} \left|\bullet(x_i)\right|$, is typically between 2 and 10 depending on the energy. The obtained numerical solutions can be used as initial guess when solving the spectral Usadel equations for the next energy value. In this way, only two sets of solutions to the spectral Usadel equations need to be stored at a time.

Note that the kinetic Usadel equations are linear in the distribution functions. Hence, it is sufficient to transform the BVP into a system of linear equations by just replacing the differential operators as finite differences as well. The system of linear equations for the distribution function with the sparse coefficient matrix is solved again using the spsolve routine. As linear equations the kinetic Usadel equations do not require any error or convergence tolerance and are solved after one call of the routine. It is good habit, though, to calculate the error by inserting the numerical solution into the kinetic Usadel equations and check whether it is smaller than a pre-specified tolerance, set here to 10^{-9} as well.

Most of the physical quantities are obtained from the Green's functions via an integration over the energy interval $[0, \hbar\omega_D]$.[41] This is accomplished by dividing this interval into a mesh which is denser near the spectral energy gap with a spacing down to $h = 10^{-6}$ and more sparse far away[42], leading to $\mathcal{O}\left(10^4\right)$ mesh points. The chosen energy mesh can be and was approved by plotting the integrands of the physical quantities and checking for a smooth behavior. The integrals are approximated using the Simpson's rule[43] successively applied to two neighboring mesh intervals $[\epsilon_{k-1}, \epsilon_k]$ and $[\epsilon_k, \epsilon_{k+1}]$ with the same spacing, starting from the high energy end: For each of the three energy values the Usadel equations need to be solved, where the solutions to the energy ϵ_{k-1} are already known from the preceding pair of neighboring mesh intervals, and the obtained numerical solutions are used as initial guess for the next energy value. After each energy value is processed, the integrands of all physical quantities at hand are calculated and stored, and after all three energy values are processed, the integral over the interval $[\epsilon_{k-1}, \epsilon_{k+1}]$ is approximated according to Simpson's rule using the stored value for the integrands. The so obtained value is added to a variable I set to zero before the first pair of intervals was processed. When going to the next pair of neighboring intervals the old values for the integrands can be overwritten by the new ones. After the last pair of

[40] Note that the Usadel equations are not transformed into a system of coupled 1st order ODEs.

[41] Actually, for $T = 0$, the only physical quantities which need integration up to the Debye energy are the charge and energy supercurrent. All other quantities have the energy $k_B T$ as upper integration limit.

[42] For energies $|\epsilon| > 10$ a spacing of $h = 10^{-1}$ is used.

[43] See, for example, [229].

neighboring mesh intervals is processed in this way, the variable I stores the approximation of the energy integral over the whole interval and thus approximates the physical quantity. In doing so, the amount of occupied storage is minimized – only two numerical solutions of the spectral and one of the kinetic Usadel equations, and for each physical quantity three values of the integrands and the one for I need to be stored while calculating the whole integral – while not affecting the processing speed, and all physical quantities are calculated simultaneously with a single loop over the energy interval.

Since the spectral Usadel equations depend on the kinetic ones only implicitly via the self-consistency equation, but the spectral coefficients Eqs. (10.17) enter the kinetic equations, one first solves the spectral Usadel equations using the relaxation method with a guess for the order parameter and then the kinetic Usadel equations. Finally, the order parameter is updated.

Obviously, the physical quantities can only be obtained once the order parameter is calculated self-consistently. This is done using a loop with a successive calculation of the order parameter, which is given by an energy integral and is calculated in the way mentioned above. After each loop run the old and new value of the order parameter are updated. The loop is terminated if

$$||1 - \Delta_{\mathrm{new}}/\Delta_{\mathrm{old}}|| < \varepsilon_{\mathrm{sc}},$$

and the order parameter is exported and stored in a file for future use.[44] With a tolerance $\varepsilon_{\mathrm{sc}} = 10^{-6}$, the number of iterations ranges from $\mathcal{O}\left(10^1\right)$ for voltages well below the energy gap to several $\mathcal{O}\left(10^2\right)$ for higher voltages.

14.3 Approximate solutions and initial guess

General assumptions for the initial guess

The relaxation method starts from an initial guess for the boundary value problem. In some cases, approximate solutions to the spectral Usadel equations (10.7) can be obtained quite effortlessly. This usually starts from a thermal equilibrium situation, in which no supercurrent is present and the order parameter is real-valued. Furthermore, the order parameter is set to its BCS bulk value, thereby neglecting any space dependence. This is of course a crude approximation, especially in hybrid systems containing superconducting and normal conducting metals in good metallic contact. But it is sufficiently good for the relaxation method to converge in most cases. In this work, a one-dimensional hybrid system composed of two superconducting wires with BCS bulk values Δ_1 and Δ_2, which are in good metallic contact, is of interest. Both metals are assumed to have the same normal-state conductivity, but different thickness d in one dimension, such that $d_1/d_2 = \Delta_2/\Delta_1$. For this structure, the approximate solutions to the spectral Usadel equations under the mentioned assumptions are derived, inspired by [166].

[44] While this termination condition would fail for the geometric series, the convergence of the order parameter can be checked easily: Take the order parameter Δ_{final} after the loop terminated, change it slightly by multiplying it with an appropriate factor $f \approx 1$ and start the whole self-consistency procedure again but with $f\Delta_{\mathrm{final}}$ as initial order parameter. For $f > (<)1$ the order parameter should decrease (increase) in each loop run, which then validates Δ_{final}.

Initial guess for an S_1S_2 proximity system

The set-up is as follows: Consider a mesoscopic S_1S_2 proximity system of two superconducting wires in thermal equilibrium. Both of them are half-infinitely long, so that their spectral Green's functions approach the respective bulk solutions Eq. (10.12). The origin of the coordinate system is located at the interface of the two superconductors. Both order parameters are real-valued and the supercurrent vanishes, thus $\chi \equiv 0$ following from the spectral Usadel equation (10.7a). Without loss of generality, it is assumed that $\Delta_1 > \Delta_2$, and the x-axis is chosen such that S_1 lies in the negative side. Further, energies are measured in units of Δ_1, so that the order parameter of S_1 is one, whereas the other one is $1 > \Delta_2/\Delta_1 \equiv \Delta = d_1/d_2$. Then, the remaining spectral Usadel equations (10.7a) for the two metals read

$$\frac{1}{2}\frac{\partial^2\theta_1}{\partial x^2} + i\epsilon \sin\left(\theta_1\right) + \cos\left(\theta_1\right) = 0$$
$$\frac{1}{2}\frac{\partial^2\theta_2}{\partial x^2} + i\epsilon \sin\left(\theta_2\right) + \Delta\cos\left(\theta_2\right) = 0.$$

The boundary conditions Eqs. (11.2) apply,

$$\theta_1\big|_{x=0} = \theta_2\big|_{x=0} \tag{14.1a}$$
$$\Delta \left.\frac{\partial\theta_1}{\partial x}\right|_{x=0} = \left.\frac{\partial\theta_2}{\partial x}\right|_{x=0}. \tag{14.1b}$$

Since both equations do not dependent explicitly on x, each of them gives rise to a conserved, i.e. space independent quantity, given by[45]

$$H_1 = \frac{1}{2}\left(\frac{\partial\theta_1}{\partial x}\right)^2 - 2i\,\epsilon\cos\left(\theta_1\right) + 2\sin\left(\theta_1\right) \tag{14.2a}$$
$$H_2 = \frac{1}{2}\left(\frac{\partial\theta_2}{\partial x}\right)^2 - 2i\,\epsilon\cos\left(\theta_2\right) + 2\Delta\sin\left(\theta_2\right). \tag{14.2b}$$

The two ODEs both got integrated once, now yielding 1st order ODEs, which can be solved (at least formally). The conserved quantities are determined from the behavior far away from the interface, where the angles approach their respective bulk solutions Eq. (10.11) and with vanishing spatial gradients, giving

$$H_1 = 2\sqrt{1-\epsilon^2}$$
$$H_2 = 2\sqrt{\Delta^2-\epsilon^2}.$$

Therewith, and after transforming to the deviations from the respective bulk solutions,

$$\theta_i = \theta_{\mathrm{BCS},i} + \delta\theta_i,$$

[45] Where do the conserved quantities come from? Facing a 2nd order ODE, one may try to look for an artificial Lagrangian with "time" x, generalized coordinate θ and "velocity" $\partial_x\theta$, for which the Euler-Lagrangian equation gives the 2nd ODE at hand. From classical mechanics it is known that the associated Hamiltonian is a "constant of motion", if it does not depend explicitly on x (see [230], for example). This is the case, since any spatial dependence of the order parameter is neglected. To some extent this example shares the same spirit as the first topic: Mathematics does not care about the physical context - same equations means same physics.

with $\tan\left(\theta_{\mathrm{BCS},2}\right) = i\epsilon/\Delta$, the 1st order ODEs (14.2) read

$$H_i = \frac{1}{2}\left(\frac{\partial\,\delta\theta_i}{\partial x}\right)^2 + H_i\cos\left(\delta\theta_i\right).$$

These Hamiltonians resemble those of mathematical pendulums with initial conditions such that they would stop in the top position with displacement angle π after an infinite amount of time. These special initial conditions allow for analytic solutions[46], which are given by

$$\tan\left(\frac{\theta_{1/2}-\theta_{\mathrm{BCS},1/2}}{4}\right) = \tan\left(\frac{\theta_{0,1/2}-\theta_{\mathrm{BCS},1/2}}{4}\right)\exp\left\{\mp\sqrt{2H_{1/2}}\,x\right\}, \tag{14.3}$$

where $\theta_{0,i} = \theta_i(x=0)$ denotes the value of the angle at the interface.

The matching condition Eq. (14.1a) requires $\theta_{0,1} = \theta_{0,2} \equiv \theta_0$. The second matching condition Eq. (14.1b) determines θ_0 to be

$$\sin\left(\theta_0\right) = \frac{F - \tilde{\epsilon}\sqrt{F^2 - 1 + \tilde{\epsilon}^2}}{1-\tilde{\epsilon}^2} \tag{14.4}$$

with

$$\tilde{\epsilon} = \epsilon\frac{1+\Delta}{\Delta}, \quad F = \frac{\sqrt{1-\left(\frac{\epsilon}{\Delta}\right)^2} - \Delta\sqrt{1-\epsilon^2}}{1-\Delta}.$$

This can be obtained by solving Eqs. (14.2) for $(\partial_x\theta_i)^2$, which is plugged into the matching condition Eq. (14.1b) squared, from which one can solve for $\sin\left(\theta_0\right)$. Note that for the numerical evaluation of the RHS of Eq. (14.4) it is important to give the energy ϵ a tiny positive imaginary part, as is usual when dealing with retarded Green's functions.

As consistency check, the limit $\Delta \to 1$, which corresponds to a single homogeneous superconductor, can be considered, for which

$$F = \sqrt{1-\epsilon^2} - \frac{\epsilon^2}{\sqrt{1-\epsilon^2}}$$

and thus $\sin\left(\theta_0\right) = \sin\left(\theta_{\mathrm{BCS}}\right)$.

Approximate solutions for a quasiparticle injector

Here, the spectral and kinetic Usadel equations are solved for a quasiparticle injector (setup 1, see Fig. (12.1)). This is done by discarding the self-consistency equation and instead using the BCS bulk value Δ_{BCS} for the order parameter. This approach neglects the supercurrent and inverse proximity effect as well as the degradation of the order parameter due to QPs and a current flow. This assumption is in agreement with numerical results.

[46] Note that there is no analytic solution to the mathematical pendulum for arbitrary initial conditions.

For the spectral quantities θ, χ, the proximity effect is neglected as well. Hence, they are given by their respective bulk solutions as well,

$$\theta = \theta_{\mathrm{BCS}} = \begin{cases} \frac{\pi}{2} + \frac{i}{2}\ln\left(\frac{1+\epsilon}{1-\epsilon}\right) & , |\epsilon| < 1 \\ \frac{i}{2}\ln\left(\frac{\epsilon+1}{\epsilon-1}\right) & , |\epsilon| > 1 \end{cases}$$
$$\chi \equiv 0.$$

Thereby, the spectral coefficients Eqs. (10.17) entering the kinetic equations (10.14) are given by

$$N_S = \Theta(|\epsilon| - 1)\frac{|\epsilon|}{\sqrt{\epsilon^2 - 1}}$$
$$D_L = \Theta(|\epsilon| - 1)$$
$$D_T = \begin{cases} \frac{1}{1-\epsilon^2} & , |\epsilon| < 1 \\ \frac{\epsilon^2}{\epsilon^2-1^2} & , |\epsilon| > 1 \end{cases}$$
$$\mathcal{R} = 2\,\Theta(1 - |\epsilon|)\frac{1}{\sqrt{1 - \epsilon^2}}$$
$$j_S = \mathcal{T} = \mathcal{L} = 0.$$

With N_S and D_L both vanishing for sub-gap energies $|\epsilon| < 1$, the Kuprianov-Lukichev boundary condition for f_L is an identity equation and thus must be replaced by another appropriate boundary condition in order to obtain a unique solution. This is given by the requirement of a vanishing energy current into the superconductor, $\partial_x f_L = 0$, at the tunnel barrier for energies below the gap, $|\epsilon| < 1$, which is due to the property of superconductors being poor heat conductors.

As the spectral coefficients do not possess a space-dependence, the kinetic equations can be solved very easily, giving

$$f_L(x, \epsilon) = \mathrm{sgn}(\epsilon)\left[\frac{N_S(\epsilon)}{r + L_S N_S(\epsilon)}(x - L_2) + 1\right]$$
$$f_T(x, \epsilon) = \frac{1}{L_S + r N_S(\epsilon)}(x - L_2)$$

for $1 < |\epsilon| < e|V|/\Delta_{\mathrm{BCS}}$, and $f_L = \mathrm{sgn}(\epsilon)$, $f_T = 0$ otherwise.

Note that the leakage current vanishes exactly and thus, the spectral charge current is conserved. This is not the case for the approximate solutions of the spectral Usadel equations given in Ref. [166], which shows that they are qualitatively valid only in equilibrium situations.

The charge current can be approximated by

$$\left(\frac{\Delta_{\mathrm{BCS}}\sigma_N}{e\xi_0}\right)^{-1} J_C = \frac{1}{r}\int_1^{\frac{e|V|}{\Delta_{\mathrm{BCS}}}} \frac{N_S^2}{L/r + N_S}\mathrm{d}\epsilon \tag{14.5}$$

$$\approx \frac{1}{r}\int_1^{\frac{e|V|}{\Delta_{\mathrm{BCS}}}} N_S \mathrm{d}\epsilon \tag{14.6}$$

$$= \frac{1}{r}\sqrt{\left(\frac{eV}{\Delta_{\mathrm{BCS}}}\right)^2 - 1} \tag{14.7}$$

for $e|V| \geq \Delta_{\mathrm{BCS}}$, where it was used that the resistance of the superconductor in the normal state is much smaller than the resistance of the tunnel junction, i.e. $L/r \ll 1 < N_S$ for energies $\epsilon > 1$. According to Fig. 12.9, this result matches the numerically found solution very well, where the supercurrent was included and the order parameter was solved self-consistently. Note also, that Eq. (14.7) coincides with the result given in [180].

Within this approximation, the QP density Eq. (12.7) is given by

$$\frac{n_{\mathrm{qp}}(x)}{N_0\Delta_{\mathrm{BCS}}} = \frac{L_2 - x}{r}\int_1^{\frac{e|V|}{\Delta_{\mathrm{BCS}}}} N_S\left[\left(\frac{L}{r} + \frac{1}{N_S}\right)^{-1} + \left(\frac{L}{r} + N_S\right)^{-1}\right]\mathrm{d}\epsilon.$$

Note that the integral is position independent as the spectral quantities are constant in space, so that the only position dependence stems from the prefactor linear in x which is due to the distribution functions. The QP density at the injector, $n_{\mathrm{qp}}(x = -L_1)$, is plotted in Fig. 12.9 as a function of the applied voltage.

As the supercurrent is neglected within this approximation, the total charge current is entirely carried by normal current Eq. (14.7), which is consequently constant along the superconductor. This is also evident from the position independent gradient of the QP density, as both are proportional to each other.

Conclusion

This thesis presents two applications of solid state physics in the microscopic and mesoscopic regime with very different contexts. Both rely on sophisticatedly exploiting the changeability of quasiparticles arising from a Bogoliubov transformation.

In Part I of this thesis a physical framework containing an experimental set-up is proposed which serves as analogue model for the interplay between quantum physics and general theory of relativity. The one-dimensional propagation of surface acoustic waves on a piezoelectric semiconducting substrate is described by the usual wave equation. This coincides with the Euler-Lagrange equation for a massless scalar field in a spacetime with a particular metric. A curvature is imposed if the speed of sound of the substrate is space dependent, $c = c(x)$. This is achieved via a voltage biased gate attached to the substrate. After a Galilean boost into the reference frame of an observer moving with appropriate speed v, the transformed effective metric has features in common with that of a black hole and an expanding universe. In particular, it possesses an acoustic horizon for surface acoustic waves at the crossover between sub- and supersonic motion, $c(x) = v$. Due to these similarities spontaneous particle creation in form of phonons is expected. Only the moving observer experiences the acoustic horizon and is exposed to the excess particles, which arise from the observer dependent notion of particles expressed via a Bogoliubov transformation. In a flat space-time particle creation does not occur for two inertial observers because of the Lorentz invariance. In analogue models, however, the existence of a preferred speed – i.e. speed of sound in the present set-up – breaks Lorentz invariance. The motion of the moving observer can be regarded as an accelerated motion while passing the region where the speed of sound changes locally. Electrons carried by dynamic quantum dots on a separate, adjacent substrate serve simultaneously as moving observer and detector for the created phonons. Their interaction is mediated by spin-orbit and usual electron-phonon coupling which can overcome the spatial separation of the two substrates due to the piezoelectric effect. A perturbative approach using the Bloch-Redfield equation predicts that the electrons equilibrate to a non-thermal steady state in their spin degree of freedom, which is ascribed to particle creation. The readout of the electron spin is accomplished by the use of a Stern-Gerlach gate, which acts as spin-to-charge current converter. The proposal combines tools and techniques which are well-known and experimentally established, hence ensuring a realistic feasibility. Further improvement on the experimental side are the use of different piezoelectric semiconducting substrates with higher piezoelectric coupling constants than GaAs, which reduces the equilibration time of the electron spin. Furthermore, a readout scheme for the multi-level orbital states of the electrons inside the dynamic quantum dot is a direct route to investigate the spectrum and nature of the radiation. On the theoretical side, the rigorous application of quantum field theory with the calculation of the Bogoliubov transformation mixing the positive and negative frequency modes of the two reference frames – the rest frame of the substrate and the detector, respectively – would give the ultimate justification for particle creation and would yield information on the spectrum of the radiation.

Part II investigates on the role of the superconducting proximity effect on the trapping performance of normal-metal quasiparticle traps in the mesoscopic regime. We consider the

injection of quasiparticles into a superconducting wire via a voltage biased tunnel junction formed with a normal-metal reservoir. At its opposite end, the superconductor is coated with another metal in good metallic contact, serving as quasiparticle trap. The non-equilibrium steady state is determined by the quasiclassical Green's functions as self-consistent solution to the Usadel equations. As the dimensions in the transverse directions are typically much smaller than the superconducting coherence length, the whole set-up can be treated approximately as one-dimensional. This is accomplished by an appropriate Taylor expansion taking into account all matching and boundary conditions. In this approximation, the overlap geometry formed by the superconducting wire and the normal-metal trap is treated as another superconductor with lowered superconducting order parameter. Matching conditions for the one-dimensional model result from the current conservation. For the two set-ups – one with attached trap and the other one without – the superconducting order parameter, local density of states, quasiparticle density and the current densities inside the superconducting wire are calculated. The influence of the superconducting proximity effect is studied by a direct comparison of the numerical results among the two set-ups. The reduction of the quasiparticle density stems from the inverse proximity effect which leads to a significant reduction of the superconducting density of states at the injector for energies $|E| = \Delta_{\mathrm{BCS}}$. However, as the total number of quasiparticle states is conserved, this reduction at energies around Δ_{BCS} is accompanied by a significant reduction of the spectral gap Ω which leads to quasiparticle poisoning, lowering the trapping performance. The manifestation of these two competing behaviors is determined by the location of the trap, which needs to be taken into account for optimizing the trapping performance. Furthermore, the conversion between dissipative normal and supercurrent is enhanced in presence of a trap since the discrepancy between Ω and Δ_{BCS} allows for occupation of states which undergo Andreev reflection. This leads to further reduction of the quasiparticle density at high injection voltages. The aptness of a one-dimensional model for different trap geometries including two-dimensional arrays depends on the exact trap sizes and positions and might require a two-dimensional model depending on the exact parameters. Furthermore, there is experimental evidence that pair-breaking phonons take an important role in the distribution of quasiparticles across the superconductor hence going beyond the mesoscopic regime. A suitable theoretical model must include the phonon Green's functions.

Bibliography

[1] H. Heine, *Oh... diese Philosophen* (C. Bertelsmann Verlag, 2015).

[2] S. W. Hawking, Communications in mathematical physics **43**, 199 (1975).

[3] T. Jacobson, Physical Review D **44**, 1731 (1991).

[4] S. D. Mathur, Classical and Quantum Gravity **26**, 224001 (2009).

[5] S. Giddings, The Future of Theoretical Physics and Cosmology , 278 (2003).

[6] S. Hossenfelder, arXiv preprint hep-ph/0412265 (2004).

[7] P. Kanti, International journal of modern physics A **19**, 4899 (2004).

[8] A. F. Ali, M. Faizal, and M. M. Khalil, Physics Letters B **743**, 295 (2015).

[9] W. G. Unruh, Physical Review Letters **46**, 1351 (1981).

[10] W. Unruh, Philosophical Transactions of the Royal Society A: Mathematical, Physical and Engineering Sciences **366**, 2905 (2008).

[11] C. Barceló, S. Liberati, and M. Visser, Living Rev. Rel **8**, 214 (2005).

[12] P. Painleve, L'Astronomie **36**, 6 (1922).

[13] T. Jacobson and G. Volovik, Physical Review D **58**, 064021 (1998).

[14] P. Nation, M. Blencowe, A. Rimberg, and E. Buks, Physical Review Letters **103**, 087004 (2009).

[15] R. Schützhold and W. G. Unruh, Physical Review Letters **95**, 031301 (2005).

[16] G. Rousseaux, C. Mathis, P. Maïssa, T. G. Philbin, and U. Leonhardt, New Journal of Physics **10**, 053015 (2008).

[17] S. Weinfurtner, E. W. Tedford, M. C. Penrice, W. G. Unruh, and G. A. Lawrence, Physical review letters **106**, 021302 (2011).

[18] L.-P. Euvé, F. Michel, R. Parentani, T. G. Philbin, and G. Rousseaux, Physical review letters **117**, 121301 (2016).

[19] H. S. Nguyen, D. Gerace, I. Carusotto, D. Sanvitto, E. Galopin, A. Lemaître, I. Sagnes, J. Bloch, and A. Amo, Physical review letters **114**, 036402 (2015).

[20] M. Elazar, V. Fleurov, and S. Bar-Ad, Physical Review A **86**, 063821 (2012).

[21] T. G. Philbin, C. Kuklewicz, S. Robertson, S. Hill, F. König, and U. Leonhardt, Science **319**, 1367 (2008).

[22] F. Marino, Physical Review A **78**, 063804 (2008).

[23] F. Belgiorno, S. L. Cacciatori, M. Clerici, V. Gorini, G. Ortenzi, L. Rizzi, E. Rubino, V. G. Sala, and D. Faccio, Physical review letters **105**, 203901 (2010).

[24] J. Steinhauer, Nature Physics **12**, 959 (2016).

[25] B. Cropp, S. Liberati, and R. Turcati, Physical Review D **94**, 063003 (2016).

[26] J. Ramón Muñoz de Nova, K. Golubkov, V. I. Kolobov, and J. Steinhauer, arXiv preprint arXiv:1809.00913 (2018).

[27] I. Buluta and F. Nori, Science **326**, 108 (2009).

[28] W. Greiner and S. Schramm, American Journal of Physics **76**, 509 (2008).

[29] M. O. Scully and M. S. Zubairy, "Quantum optics," (1999).

[30] E. Yablonovitch, Physical Review Letters **62**, 1742 (1989).

[31] J. Schwinger, Proceedings of the National Academy of Sciences of the United States of America **89**, 4091 (1992).

[32] D. E. Bruschi, I. Fuentes, and J. Louko, Physical Review D **85**, 061701 (2012).

[33] L. Parker, Physical Review Letters **21**, 562 (1968).

[34] C. M. Wilson, G. Johansson, A. Pourkabirian, M. Simoen, J. R. Johansson, T. Duty, F. Nori, and P. Delsing, Nature **479**, 376 (2011).

[35] K. Lange, J. Peise, B. Lücke, T. Gruber, A. Sala, A. Polls, W. Ertmer, B. Juliá-Díaz, L. Santos, and C. Klempt, New Journal of Physics **20**, 103017 (2018).

[36] S. Vezzoli, A. Mussot, N. Westerberg, A. Kudlinski, H. D. Saleh, A. Prain, F. Biancalana, E. Lantz, and D. Faccio, Communications Physics **2**, 1 (2019).

[37] R. Schützhold, M. Uhlmann, L. Petersen, H. Schmitz, A. Friedenauer, and T. Schätz, Physical review letters **99**, 201301 (2007).

[38] C. Fey, T. Schaetz, and R. Schützhold, Physical Review A **98**, 033407 (2018).

[39] S. Eckel, A. Kumar, T. Jacobson, I. B. Spielman, and G. K. Campbell, Physical Review X **8**, 021021 (2018).

[40] P. O. Fedichev and U. R. Fischer, Physical review letters **91**, 240407 (2003).

[41] U. R. Fischer and R. Schützhold, Physical Review A **70**, 063615 (2004).

[42] M. Wittemer, F. Hakelberg, P. Kiefer, J.-P. Schröder, C. Fey, R. Schützhold, U. Warring, and T. Schaetz, arXiv preprint arXiv:1903.05523 (2019).

[43] S. H. Simon, Physical Review B **54**, 13878 (1996).

[44] K. Ingebrigtsen, Journal of Applied Physics **41**, 454 (1970).

[45] G. Gumbs, G. Aĭzin, and M. Pepper, Physical Review B **57**, 1654 (1998).

[46] P. Bierbaum, Applied Physics Letters **21**, 595 (1972).

[47] A. Hutson and D. L. White, Journal of Applied Physics **33**, 40 (1962).

[48] A. Wixforth, J. Scriba, M. Wassermeier, J. P. Kotthaus, G. Weimann, and W. Schlapp, Physical Review B **40**, 7874 (1989).

[49] S. M. Sze, *Semiconductor devices: physics and technology* (John wiley & sons, 2008).

[50] S. Datta, *Surface acoustic wave devices* (Prentice Hall, 1986).

[51] W. Unruh and R. Schützhold, Physical Review D **68**, 024008 (2003).

[52] S. W. Hawking, Nature **248**, 30 (1974).

[53] G. W. Gibbons and S. W. Hawking, Physical Review D **15**, 2752 (1977).

[54] M. Visser, International Journal of Modern Physics D **12**, 649 (2003).

[55] M. Visser, Classical and Quantum Gravity **15**, 1767 (1998).

[56] D. Johannsmann, Soft and Biological Matter , 191 (2015).

[57] D. A. Neamen, *Semiconductor physics and devices: basic principles* (New York, NY: McGraw-Hill,, 2012).

[58] G. D. Mahan, *Many-particle physics* (Springer Science & Business Media, 2013).

[59] F. Stern, Physical Review B **9**, 4597 (1974).

[60] T. Bateman, H. McSkimin, and J. Whelan, Journal of Applied Physics **30**, 544 (1959).

[61] W. Sritrakool, V. Sa-Yakanit, and H. Glyde, Physical Review B **32**, 1090 (1985).

[62] S.-H. Lee, H.-H. Jeong, S.-B. Bae, H.-C. Choi, J.-H. Lee, and Y.-H. Lee, IEEE Transactions on Electron Devices **48**, 524 (2001).

[63] J. A. Stotz, R. Hey, P. V. Santos, and K. H. Ploog, Nature Materials **4**, 585 (2005).

[64] C. Rocke, S. Zimmermann, A. Wixforth, J. Kotthaus, G. Böhm, and G. Weimann, Physical Review Letters **78**, 4099 (1997).

[65] J. Shilton, V. Talyanskii, M. Pepper, D. Ritchie, J. Frost, C. Ford, C. Smith, and G. Jones, Journal of Physics: Condensed Matter **8**, L531 (1996).

[66] J. Wang, J. Du, and Q. Pan, Science in China Series G: Physics, Mechanics and Astronomy **50**, 631 (2007).

[67] C. Barnes, J. Shilton, and A. Robinson, Physical Review B **62**, 8410 (2000).

[68] S. Furuta, C. Barnes, and C. Doran, Physical Review B **70**, 205320 (2004).

[69] B. A. Auld, *Acoustic fields and waves in solids* (1973).

[70] M. J. Schütz, in *Quantum Dots for Quantum Information Processing: Controlling and Exploiting the Quantum Dot Environment* (Springer, 2017) pp. 143–196.

[71] G. Aizin, G. Gumbs, and M. Pepper, Physical Review B **58**, 10589 (1998).

[72] M. Roy, physica status solidi (a) **45**, 549 (1978).

[73] A. Robinson and C. Barnes, Physical Review B **63**, 165418 (2001).

[74] M. Buitelaar, P. Leek, V. Talyanskii, C. Smith, D. Anderson, G. Jones, J. Wei, and D. Cobden, Semiconductor Science and Technology **21**, S69 (2006).

[75] D. P. DiVincenzo, Fortschritte der Physik: Progress of Physics **48**, 771 (2000).

[76] K. E. Cahill and R. J. Glauber, Physical Review **177**, 1857 (1969).

[77] A. S. Mouritzen and K. Mølmer, Physical Review a **73**, 042105 (2006).

[78] G. Dresselhaus, Physical Review **100**, 580 (1955).

[79] J. Stotz, F. Alsina, R. Hey, and P. Santos, Physica E: Low-dimensional Systems and Nanostructures **26**, 67 (2005).

[80] A. V. Khaetskii and Y. V. Nazarov, Physical Review B **64**, 125316 (2001).

[81] H.-P. Breuer and F. Petruccione, *The theory of open quantum systems* (Oxford University Press on Demand, 2002).

[82] P. Boucher, S. Rauwerdink, A. Tahraoui, C. Wenger, Y. Yamamoto, and P. Santos, Applied Physics Letters **105**, 161904 (2014).

[83] L. Adkins and A. Hughes, Journal of Applied Physics **42**, 1819 (1971).

[84] X. Zhao, P. Huang, and X. Hu, Scientific reports **6**, 1 (2016).

[85] P. Huang and X. Hu, Physical Review B **88**, 075301 (2013).

[86] V. N. Golovach, A. Khaetskii, and D. Loss, Physical review letters **93**, 016601 (2004).

[87] M. Borhani, V. N. Golovach, and D. Loss, Physical Review B **73**, 155311 (2006).

[88] V. N. Golovach, M. Borhani, and D. Loss, Physical Review B **74**, 165319 (2006).

[89] P. Huang and X. Hu, Physical Review B **89**, 195302 (2014).

[90] P. Hänggi, P. Talkner, and M. Borkovec, Reviews of modern physics **62**, 251 (1990).

[91] T. Sogawa, H. Ando, and S. Ando, Physical Review B **61**, 5535 (2000).

[92] W. G. Unruh, Foundations of Physics **44**, 532 (2014).

[93] U. Weiss, *Quantum dissipative systems*, Vol. 13 (World scientific, 2012).

[94] F. Wilhelm, M. Storcz, U. Hartmann, and M. R. Geller, arXiv preprint cond-mat/0603637 (2006).

[95] C. P. Slichter, *Principles of magnetic resonance*, Vol. 1 (Springer Science & Business Media, 2013).

[96] R. R. Ernst, G. Bodenhausen, A. Wokaun, *et al.*, *Principles of nuclear magnetic resonance in one and two dimensions*, Vol. 14 (Clarendon press Oxford, 1987).

[97] Y.-R. Shen, New York, Wiley-Interscience, 1984, 575 p. (1984).

[98] R. Zwanzig, The Journal of Chemical Physics **33**, 1338 (1960).

[99] S. Nakajima, Progress of Theoretical Physics **20**, 948 (1958).

[100] K. Blum, *Density matrix theory and applications*, Vol. 64 (Springer Science & Business Media, 2012).

[101] K. E. Sapsford and L. C. Shriver-Lake, "Principles of bacterial detection: Biosensors, recognition receptors and microsystems," (Springer-Verlag New York, 2008) Chap. Bacterial Detection Using Evanescent Wave-Based Fluorescent Biosensors, pp. 83–108.

[102] M. Shaw, R. Lutchyn, P. Delsing, and P. Echternach, Physical Review B **78**, 024503 (2008).

[103] D. Ristè, C. Bultink, M. Tiggelman, R. Schouten, K. Lehnert, and L. DiCarlo, Nature communications **4**, 1 (2013).

[104] M. Stern, G. Catelani, Y. Kubo, C. Grezes, A. Bienfait, D. Vion, D. Esteve, and P. Bertet, Physical review letters **113**, 123601 (2014).

[105] P. De Visser, J. Baselmans, P. Diener, S. Yates, A. Endo, and T. Klapwijk, Physical review letters **106**, 167004 (2011).

[106] H. Paik, D. Schuster, L. S. Bishop, G. Kirchmair, G. Catelani, A. Sears, B. Johnson, M. Reagor, L. Frunzio, L. Glazman, *et al.*, Physical Review Letters **107**, 240501 (2011).

[107] C. Wang, Y. Y. Gao, I. M. Pop, U. Vool, C. Axline, T. Brecht, R. W. Heeres, L. Frunzio, M. H. Devoret, G. Catelani, *et al.*, Nature communications **5**, 1 (2014).

[108] G. Catelani, R. J. Schoelkopf, M. H. Devoret, and L. I. Glazman, Physical Review B **84**, 064517 (2011).

[109] G. Catelani, S. E. Nigg, S. Girvin, R. Schoelkopf, and L. Glazman, Physical Review B **86**, 184514 (2012).

[110] G. Catelani, Physical Review B **89**, 094522 (2014).

[111] R. Lutchyn, L. Glazman, and A. Larkin, Physical Review B **72**, 014517 (2005).

[112] R. Lutchyn, L. Glazman, and A. Larkin, Physical Review B **74**, 064515 (2006).

[113] J. Leppäkangas and M. Marthaler, Physical Review B **85**, 144503 (2012).

[114] J. M. Martinis, M. Ansmann, and J. Aumentado, Physical review letters **103**, 097002 (2009).

[115] J. Pekola, D. Anghel, T. Suppula, J. Suoknuuti, A. Manninen, and M. Manninen, Applied Physics Letters **76**, 2782 (2000).

[116] F. Giazotto, T. T. Heikkilä, A. Luukanen, A. M. Savin, and J. P. Pekola, Reviews of Modern Physics **78**, 217 (2006).

[117] S. Rajauria, P. S. Luo, T. Fournier, F. W. Hekking, H. Courtois, and B. Pannetier, Physical review letters **99**, 047004 (2007).

[118] J. T. Muhonen, M. Meschke, and J. P. Pekola, Reports on Progress in Physics **75**, 046501 (2012).

[119] P. Joyez, P. Lafarge, A. Filipe, D. Esteve, and M. Devoret, Physical review letters **72**, 2458 (1994).

[120] K. Lehnert, K. Bladh, L. Spietz, D. Gunnarsson, D. Schuster, P. Delsing, and R. Schoelkopf, Physical review letters **90**, 027002 (2003).

[121] J. Aumentado, M. W. Keller, J. M. Martinis, and M. H. Devoret, Physical review letters **92**, 066802 (2004).

[122] D. Gunnarsson, T. Duty, K. Bladh, and P. Delsing, Physical Review B **70**, 224523 (2004).

[123] S. Kaplan, C. Chi, D. Langenberg, J.-J. Chang, S. Jafarey, and D. Scalapino, Physical Review B **14**, 4854 (1976).

[124] J. L. Levine and S. Hsieh, Physical Review Letters **20**, 994 (1968).

[125] A. Rothwarf and B. Taylor, Physical Review Letters **19**, 27 (1967).

[126] U. Patel, I. V. Pechenezhskiy, B. Plourde, M. Vavilov, and R. McDermott, Physical Review B **96**, 220501 (2017).

[127] G. Catelani, L. Glazman, and K. Nagaev, Physical Review B **82**, 134502 (2010).

[128] C. Owen and D. Scalapino, Physical Review Letters **28**, 1559 (1972).

[129] R. McDermott and M. Vavilov, Physical Review Applied **2**, 014007 (2014).

[130] P. J. Liebermann and F. K. Wilhelm, Physical Review Applied **6**, 024022 (2016).

[131] E. Leonard Jr, M. A. Beck, J. Nelson, B. G. Christensen, T. Thorbeck, C. Howington, A. Opremcak, I. V. Pechenezhskiy, K. Dodge, N. P. Dupuis, *et al.*, Physical Review Applied **11**, 014009 (2019).

[132] B. Josephson, Phys. Lett. **1**, 251 (1962).

[133] M. Nahum, T. M. Eiles, and J. M. Martinis, Applied Physics Letters **65**, 3123 (1994).

[134] R. L. Kautz and J. M. Martinis, Physical Review B **42**, 9903 (1990).

[135] P. Joyez, *The single cooper pair transistor: a macroscopic quantum system*, Ph.D. thesis (1995).

[136] S. Friedrich, K. Segall, M. Gaidis, C. Wilson, D. Prober, A. Szymkowiak, and S. Moseley, Applied physics letters **71**, 3901 (1997).

[137] A. Ferguson, R. Lutchyn, R. Clark, *et al.*, Physical Review B **77**, 100501 (2008).

[138] J. Ullom, P. Fisher, and M. Nahum, Applied physics letters **73**, 2494 (1998).

[139] J. Peltonen, J. Muhonen, M. Meschke, N. Kopnin, and J. P. Pekola, Physical Review B **84**, 220502 (2011).

[140] I. Nsanzineza and B. Plourde, Physical review letters **113**, 117002 (2014).

[141] M. Taupin, I. Khaymovich, M. Meschke, A. Mel'nikov, and J. Pekola, Nature communications **7**, 1 (2016).

[142] D. Goldie, N. Booth, C. Patel, and G. Salmon, Physical review letters **64**, 954 (1990).

[143] J. Ullom, P. Fisher, and M. Nahum, Physical Review B **61**, 14839 (2000).

[144] S. Rajauria, L. Pascal, P. Gandit, F. W. Hekking, B. Pannetier, and H. Courtois, Physical Review B **85**, 020505 (2012).

[145] H. Knowles, V. Maisi, and J. P. Pekola, Applied Physics Letters **100**, 262601 (2012).

[146] H. Nguyen, T. Aref, V. Kauppila, M. Meschke, C. Winkelmann, H. Courtois, and J. P. Pekola, New Journal of Physics **15**, 085013 (2013).

[147] O.-P. Saira, A. Kemppinen, V. Maisi, and J. P. Pekola, Physical Review B **85**, 012504 (2012).

[148] L. Sun, L. DiCarlo, M. Reed, G. Catelani, L. S. Bishop, D. Schuster, B. Johnson, G. A. Yang, L. Frunzio, L. Glazman, *et al.*, Physical review letters **108**, 230509 (2012).

[149] H. Wang, M. Hofheinz, J. Wenner, M. Ansmann, R. Bialczak, M. Lenander, E. Lucero, M. Neeley, A. O'Connell, D. Sank, *et al.*, Applied Physics Letters **95**, 233508 (2009).

[150] C. Song, T. W. Heitmann, M. P. DeFeo, K. Yu, R. McDermott, M. Neeley, J. M. Martinis, and B. L. Plourde, Physical Review B **79**, 174512 (2009).

[151] A. Hosseinkhani, R.-P. Riwar, R. Schoelkopf, L. Glazman, and G. Catelani, Physical Review Applied **8**, 064028 (2017).

[152] A. Hosseinkhani and G. Catelani, Physical Review B **97**, 054513 (2018).

[153] J.-J. Chang and D. Scalapino, Physical Review B **15**, 2651 (1977).

[154] S. Rajauria, H. Courtois, and B. Pannetier, Physical Review B **80**, 214521 (2009).

[155] M. Lenander, H. Wang, R. C. Bialczak, E. Lucero, M. Mariantoni, M. Neeley, A. O'Connell, D. Sank, M. Weides, J. Wenner, *et al.*, Physical Review B **84**, 024501 (2011).

[156] R.-P. Riwar, A. Hosseinkhani, L. D. Burkhart, Y. Y. Gao, R. J. Schoelkopf, L. I. Glazman, and G. Catelani, Physical Review B **94**, 104516 (2016).

[157] K. D. Usadel, Physical Review Letters **25**, 507 (1970).

[158] W. Belzig, F. K. Wilhelm, C. Bruder, G. Schön, and A. D. Zaikin, Superlattices and microstructures **25**, 1251 (1999).

[159] A. Volkov and V. Pavlovskii, in *AIP Conference Proceedings*, Vol. 427 (American Institute of Physics, 1998) pp. 343–358.

[160] S. Guéron, H. Pothier, N. O. Birge, D. Esteve, and M. Devoret, Physical review letters **77**, 3025 (1996).

[161] A. Anthore, H. Pothier, and D. Esteve, Physical review letters **90**, 127001 (2003).

[162] A. Volkov, V. Pavlovskii, and R. Seviour, arXiv preprint cond-mat/9811151 (1998).

[163] R. Seviour, C. Lambert, and A. Volkov, Physical Review B **58**, 12338 (1998).

[164] P. Charlat, H. Courtois, P. Gandit, D. Mailly, A. Volkov, and B. Pannetier, Physical review letters **77**, 4950 (1996).

[165] P. Charlat, H. Courtois, P. Gandit, D. Mailly, A. Volkov, and B. Pannetier, Czechoslovak Journal of Physics **46**, 3107 (1996).

[166] W. Belzig, C. Bruder, and G. Schön, Physical Review B **54**, 9443 (1996).

[167] A. Zaikin, F. Wilhelm, and A. Golubov, arXiv preprint cond-mat/9604002 (1996).

[168] A. A. Golubov, F. Wilhelm, and A. Zaikin, Physical Review B **55**, 1123 (1997).

[169] P. Virtanen, T. T. Heikkilä, F. S. Bergeret, and J. C. Cuevas, Physical review letters **104**, 247003 (2010).

[170] J. Cuevas, J. Hammer, J. Kopu, J. Viljas, and M. Eschrig, Physical Review B **73**, 184505 (2006).

[171] P. Virtanen and T. T. Heikkilä, Applied Physics A **89**, 625 (2007).

[172] V. Kauppila, H. Nguyen, and T. Heikkilä, Physical Review B **88**, 075428 (2013).

[173] J. Voutilainen, T. T. Heikkilä, and N. B. Kopnin, Physical Review B **72**, 054505 (2005).

[174] J. Rammer and H. Smith, Reviews of modern physics **58**, 323 (1986).

[175] W. Belzig, F. K. Wilhelm, C. Bruder, G. Schön, and A. D. Zaikin, arXiv preprint cond-mat/9812297 (1998).

[176] J. Rammer, *Quantum field theory of non-equilibrium states*, Vol. 22 (Cambridge University Press Cambridge, 2007).

[177] N. Kopnin, *Theory of nonequilibrium superconductivity*, Vol. 110 (Oxford University Press, 2001).

[178] C. Timm, Institute of theoretical Physics Dresden (2012).

[179] P.-G. De Gennes, *Superconductivity of metals and alloys* (CRC Press, 2018).

[180] M. Tinkham, *Introduction to superconductivity* (Courier Corporation, 2004).

[181] R. Kubo, Journal of the Physical Society of Japan **12**, 570 (1957).

[182] G.-C. Wick, Physical review **80**, 268 (1950).

[183] G. Rickayzen, *Green's functions and condensed matter* (Courier Corporation, 2013).

[184] R. Kubo, M. Toda, and N. Hashitsume, *Statistical physics II: nonequilibrium statistical mechanics*, Vol. 31 (Springer Science & Business Media, 2012).

[185] L. N. Cooper, Physical Review **104**, 1189 (1956).

[186] J. Bardeen, L. N. Cooper, and J. R. Schrieffer, Physical Review **106**, 162 (1957).

[187] J. Bardeen, L. N. Cooper, and J. R. Schrieffer, Physical review **108**, 1175 (1957).

[188] A. Balatsky and J. Bonca, Physical Review B **48**, 7445 (1993).

[189] P. Coleman, E. Miranda, and A. Tsvelik, Physical review letters **70**, 2960 (1993).

[190] J. Linder and A. V. Balatsky, Reviews of Modern Physics **91**, 045005 (2019).

[191] T. Dubouchet, B. Sacépé, J. Seidemann, D. Shahar, M. Sanquer, and C. Chapelier, Nature Physics **15**, 233 (2019).

[192] V. Geshkenbein, L. Ioffe, and A. Larkin, Physical Review B **55**, 3173 (1997).

[193] Y. Nambu, Physical Review **117**, 648 (1960).

[194] A. A. Abrikosov, L. P. Gorkov, and I. E. Dzyaloshinski, *Methods of quantum field theory in statistical physics* (Courier Corporation, 2012).

[195] L. Gor'kov, in *Superconductivity* (Springer, 2008) pp. 201–224.

[196] G. Eilenberger, Zeitschrift für Physik A Hadrons and nuclei **214**, 195 (1968).

[197] A. Larkin and Y. Ovchinnikov, Sov. Phys. JETP **41**, 960 (1975).

[198] G. Schön, in *Nonequilibrium Superconductivity*, edited by D. Langenberg and A. Larkin (Elsevier, Amsterdam, 1984).

[199] V. Chandrasekhar, in *Superconductivity*, edited by K. Bennemann and J. Ketterson (Springer, Berlin, Heidelberg, 2008).

[200] J. W. Serene and D. Rainer, Physics Reports **101**, 221 (1983).

[201] A. Schmid and G. Schön, Journal of Low Temperature Physics **20**, 207 (1975).

[202] A. Larkin and Y. Ovchinnikov, Zh. Eksp. Teor. Fiz. **73**, 7 (1977).

[203] U. Eckern and A. Schmid, Journal of Low Temperature Physics **45**, 137 (1981).

[204] F. S. Bergeret, M. Silaev, P. Virtanen, and T. T. Heikkila, arXiv preprint arXiv:1706.08245 (2017).

[205] S.-K. Yip, Physical Review B **58**, 5803 (1998).

[206] W. McMillan, Physical Review **175**, 537 (1968).

[207] Y. V. Fominov and M. Feigel'man, Physical Review B **63**, 094518 (2001).

[208] C. Beenakker, in *Quantum mesoscopic phenomena and mesoscopic devices in microelectronics* (Springer, 2000) pp. 51–60.

[209] J. M. Martinis, G. C. Hilton, K. D. Irwin, and D. A. Wollman, Nuclear Instruments and Methods in Physics Research Section A: Accelerators, Spectrometers, Detectors and Associated Equipment **444**, 23 (2000).

[210] G. Brammertz, A. A. Golubov, P. Verhoeve, R. Den Hartog, A. Peacock, and H. Rogalla, Applied physics letters **80**, 2955 (2002).

[211] P. Dubos, H. Courtois, B. Pannetier, F. Wilhelm, A. Zaikin, and G. Schön, Physical Review B **63**, 064502 (2001).

[212] P. Visani, A. Mota, and A. Pollini, Physical review letters **65**, 1514 (1990).

[213] A. L. Fauchère, W. Belzig, and G. Blatter, Physical review letters **82**, 3336 (1999).

[214] A. Andreev, Sov. Phys. JETP **19**, 1228 (1964).

[215] B. Pannetier and H. Courtois, Journal of low temperature physics **118**, 599 (2000).

[216] T. Klapwijk, Journal of superconductivity **17**, 593 (2004).

[217] M. Eschrig, Reports on Progress in Physics **78**, 104501 (2015).

[218] J. Linder and J. W. Robinson, Nature Physics **11**, 307 (2015).

[219] F. Bergeret, A. Volkov, and K. Efetov, Physical review letters **86**, 4096 (2001).

[220] L. Casparis, M. R. Connolly, M. Kjaergaard, N. J. Pearson, A. Kringhøj, T. W. Larsen, F. Kuemmeth, T. Wang, C. Thomas, S. Gronin, *et al.*, Nature nanotechnology **13**, 915 (2018).

[221] A. Zaitsev, Zh. Eksp. Teor. Fiz **86**, 1742 (1984).

[222] M. Y. Kuprianov and V. Lukichev, Zh. Eksp. Teor. Fiz **94**, 149 (1988).

[223] C. Lambert, R. Raimondi, V. Sweeney, and A. Volkov, Physical Review B **55**, 6015 (1997).

[224] D. Thouless, Physical Review Letters **39**, 1167 (1977).

[225] J. Phillips, Physical Review Letters **10**, 96 (1963).

[226] V. Cherkez, J. Cuevas, C. Brun, T. Cren, G. Ménard, F. Debontridder, V. Stolyarov, and D. Roditchev, Physical Review X **4**, 011033 (2014).

[227] A. Jacobs and R. Kümmel, Physical Review B **64**, 104515 (2001).

[228] W. H. Press, S. A. Teukolsky, W. T. Vetterling, and B. P. Flannery, "Numerical recipes in c," (1988).

[229] P. J. Davis and P. Rabinowitz, *Methods of numerical integration* (Courier Corporation, 2007).

[230] H. Goldstein, C. Poole, and J. Safko, "Classical mechanics," (2002).